STATISTICAL MECHANICS OF PRESSURIZED TWO-DIMENSIONAL POLYMER RINGS

By

Mithun Kumar Mitra

The Institute of Mathematical Sciences, Chennai.

A thesis submitted to the
Board of Studies in Physical Sciences

In partial fulfillment of the requirements

For the Degree of

DOCTOR OF PHILOSOPHY

of

HOMI BHABHA NATIONAL INSTITUTE

August 2009

Homi Bhabha National Institute

Recommendations of the Viva Voce Board

As members of the Viva Voce Board, we recommend that the dissertation prepared by **Mithun Kumar Mitra** entitled "Statistical Mechanics of Pressurized Two-dimensional polymer rings" may be accepted as fulfilling the dissertation requirement for the Degree of Doctor of Philosophy.

---------- **Date :**
Chairman : Chair of Committee

---------- **Date :**
Convener : Convenor of Committee

---------- **Date :**
Member : Member 1 of Committee

---------- **Date :**
Member : Member 2 of Committee

Final approval and acceptance of this dissertation is contingent upon the candidate's submission of the final copies of the dissertation to HBNI.

I hereby certify that I have read this dissertation prepared under my direction and recommend that it may be accepted as fulfilling the dissertation requirement.

---------- **Date :**
Guide : Gautam I. Menon

---------- **Date :**
Guide : Rajesh Ravindran

DECLARATION

I, hereby declare that the investigation presented in the thesis has been carried out by me. The work is original and the work has not been submitted earlier as a whole or in part for a degree/diploma at this or any other Institution or University.

Mithun Kumar Mitra

To

Ma and Baba

ACKNOWLEDGEMENTS

This thesis owes a debt of gratitude to many people. Firstly, I would like to thank my advisor, Dr. Gautam I. Menon, who was not only my PhD advisor but my Masters advisor as well. He has been the best mentor that I could have asked for, and provided constant guidance and encouragement for five long years. My regular discussions with him form the basis of much of my knowledge of statistical mechanics and condensed matter, and made my experience of graduate life such a rewarding one.

My co-advisor, Dr. Rajesh Ravindran, has had an invaluable effect on this thesis. Although he joined after I had been for three years in Matscience, this thesis would not have been possible in its present form without his help and guidance. It was a genuine pleasure discussing physics with him, and his approach to research and science has been truly educational.

I had many discussions over the years with several faculty and my fellow students in Matscience, especially those in the condensed matter group, both regarding my own projects as well as physics in general. I am grateful to them for the many vibrant discussions they provided. In particular, I would like to thank Dr. Sitabhra Sinha and Dr. Purusattam Ray for many discussions regarding my thesis project. In addition I also benefitted at various times from discussions with Naveen, Sumithra, Vinu, Saptarshi, Raj, Kamil and Amit. I am also grateful to the many wonderful teachers in the institute, from whom it was my pleasure to learn. I would also like to thank all the staff members of IMSc for their sincere help in all matters.

The six years I spent in Matscience would not have been anywhere as enjoyable had it not been for the wonderful friendships I formed. Our batch was a notorious one, and we spent many wonderful evenings in gossip and games, and equally many nights awake catching up on our work. For five years out of the six I spent in Matscience, office 115 had been my refuge, and for four of those five years, I had the company of my officemates, Raj Kumar Pan and Bireswar Das to thank for all of the memories. The three of us spent countless hours together, discussing any and all matters academic and (mostly) non-academic that arose. My explorations of the Chennai food landscape were carried out mostly with Kinjal Banerjee, and together

we left almost no restaurant unexplored. The football games in the evenings were a bright spot of any day. The Matscience football club was the source of a few broken bones, much joy and even more friends. The nightly tea circle was another fixture of Matscience life. No topic was taboo and the discussions often carried on late into the night and sometimes even into the morning. To these and all other friends, a big thank you for making life in Matscience the great experience it was.

Finally, none of this would have been possible without the constant support and encouragement of my family. My parents have been there throughout to support unconditionally whatever decision I have made, and been a real pillar of support. Even in the middle of difficult times, when I could not be with them, they have ungrudgingly braved adversity. To them I owe a debt that can never be repaid. My sister has been my greatest friend, co-conspirator and guide. Our regular conversations were a source of constant joy. Despite her occasional efforts to act as the big sister, she has been the best friend I could ask for. For the last two years of my time in Matscience, I had a new person to look forward to meeting whenever I came home. My niece brightened my visits immeasurably, and towards the last few months when she started talking I probably spent more time talking to her on the phone than I did with my sister. Without their ever-present love and support, this thesis would not have seen the light of day.

Synopsis

This thesis studies the statistical mechanics of pressurized ring polymers. These can be thought of as simple low-dimensional models for the understanding of vesicle shapes and phase transitions, a classic problem first studied several decades ago in the context of the shapes of red blood cells. The problem of vesicle shapes was originally studied by Helfrich and Canham and others, who described such shapes in terms of the energy minimising configurations of a curvature Hamiltonian, under the constraints of fixed enclosed volume and surface area. Shape changes arise when solutions of the Euler-Lagrange equations representing distinct shapes exchange stability. However, the non-linearity of these equations, if no special symmetries are assumed, necessitates purely numerical approaches. Further, while the curvature modulus in bilayer lipid membrane systems is often large, so that thermal fluctuations about the minimum free energy structure may be ignored, the more general problem of understanding the thermodynamics of such shape transitions is a formidable one.

In view of the complexity of the full three dimensional problem, it is instructive to analyse the equivalent problem in two dimensions. Such an approach yields useful understanding about the full problem in three dimensions, besides being interesting in its own right. The two-dimensional variant of the vesicle problem was first studied by Leibler, Singh and Fisher, who modeled vesicles as polymer rings of fixed contour length, whose enclosed area is constrained through a coupling to a pressure difference term. In addition, the bending rigidity of the polymer ring plays a crucial role in determining the shape of the ring. The problem is characterised by the existence of a continuous phase transition at zero pressure that separates a branched polymer phase from an inflated phase, with the ring being described by a self-avoiding walk at the transition point.

Another interesting version of the two-dimensional vesicle problem is obtained by studying the behaviour of lattice polygons. The polygon models the vesicle perimeter and is situated on an underlying lattice with the excluded volume parameter set by the lattice spacing. The analogy with the vesicle case is obtained by studying the variation of area with pressure for a polygon with a fixed perimeter.

In chapter I of this thesis, the Introduction, we provide a brief review of the literature regarding fluid vesicles. We also summarise known results for different classes of models for two-dimensional vesicles, including the self-avoiding and self-intersecting cases, and lattice polygon models. The chapter-wise summary of the results obtained in this thesis is presented below.

Pressurised Semiflexible Self-Intersecting Polymer Rings

The model for the two-dimensional vesicle as described above presents many difficulties for analytic studies, arising principally from the self-avoidance constraint. In Chapter 2 of this thesis, we study a related class of models in which the polymer ring is allowed to intersect itself, and the pressure term is conjugate to an algebraic or signed area. While the flexible chain problem was studied earlier, we investigate the effects of semiflexibility in this inextensible self- intersecting ring problem.

The flexible chain problem is characterised by a continuous phase transition at a critical value of an appropriately scaled pressure, separating collapsed and inflated regimes of the ring. We show that this transition survives for non-zero values of the bending rigidity and obtain an analytic form for the phase boundary separating the collapsed and inflated phases in the scaled pressure – bending rigidity plane.

We propose simple Flory theories to obtain exponents in different regimes for this model. The predictions of simple Flory approaches appear to be exact in this case, and demonstrate the power of such simple scaling arguments. We reproduce exact results for the flexible chain by using an analogy with the quantum mechanical problem of an electron moving in a magnetic field applied transverse to the plane of motion. We then incorporate semiflexibility in both the continuum and lattice models through scaling arguments, obtaining very good agreement with numerics. The numerical data was obtained through Monte Carlo simulations of both the continuum and lattice models. In addition, for the lattice polygons, exact numerical data is also obtained through the exact enumeration method, which explicitly counts the total number of allowed polygons, and hence the partition function.

We also perform several mean-field approaches to this model. We discuss how different mean-field approximations, motivated by physical arguments, model the behaviour of the system in different regimes of parameter space. A mean-field

approach where the inextensibility constraint is satisfied exactly but the closure condition is satisfied only on average yields better results in the large pressure regime whereas one in which the closure condition is satisfied exactly but the inextensibility constraint is satisfied in a mean-field sense is better suited for the low-pressure regime.

The usefulness of these results for more realistic systems lies in the fact that self-intersections are irrelevant in the large pressure limit. The results obtained at large pressures should therefore apply both qualitatively and quantitatively to the more realistic case of a pressurised self-avoiding polymer.

Asymptotic Behaviour of Lattice Polygons

In Chapter 3, we study the related problem of the asymptotic behaviour of the area of lattice polygons in the inflated phase. Although motivated by the fluid vesicle problem, the result presented in this work has a much wider applicability. The study of lattice polygons weighted by area and perimeter is a central problem in lattice statistics and combinatorics. Lattice polygons have been used to model vesicles, cell membranes, emulsions, polymers and percolation clusters.

In our work we considered inflated polygons of fixed perimeter. We calculate the area analytically for two special cases of lattice polygons - convex and column-convex lattice polygons using the Wulff construction, a variational approach using simple combinatorial arguments and the Euler-Lagrange equation. The asymptotic behaviour was observed to coincide for both classes of polygons. We therefore conjecture that overhangs are not important in the inflated regime, and hence that self avoiding polygons should have the same asymptotic behaviour. We obtain, in the inflated limit, $\tilde{p} = pN \gg 1$, the asymptotic behaviour of the area to be,

$$\langle A \rangle = \frac{N^2}{16}\left[1 - \frac{32\pi^2}{3\tilde{p}^2} + \frac{64}{\tilde{p}^2}\mathrm{Li}_2\left(1-\alpha\right)\right], \tag{1}$$

where Li_2 is the dilogarithm function

$$\mathrm{Li}_2(x) = \sum_{m=1}^{\infty} \frac{x^m}{m^2}, \tag{2}$$

and, $\alpha = e^{-2J}$ characterizes the bending rigidity of the polygon. This was verified

numerically using exact enumeration and lattice Monte Carlo methods. The data matches the predicted form to a high degree of accuracy. We also show numerically that self intersections were irrelevant in the inflated regime. These results continue to remain valid in the presence of a non-zero bending rigidity.

Finite Pressure Phase Transition in Self-Avoiding Rings

In Chapter 4, we revisit the classic problem of self-avoiding two-dimensional polymer rings originally studied by Leibler, Singh and Fisher. In their original work they described a scaling regime around zero pressure, with a phase transition separating branched polymer behaviour from the expanded phase. However, as Maggs et. al. subsequently showed, the right extrapolation predicts that area grows as the cube of the system size for large pressures. The expanded regime is thus simply inaccessible in scaling arguments based on the fixed point at zero pressure, the validity of the scaling assumptions of LSF being confined to the small pressure regimes.

Since at sufficiently large pressure values, a pressurised polymer must have an area which grows as the square of the number of monomers, the LSF approach must be suitably modified to allow for the existence of a swollen phase. We show that indeed, a large pressure inflated regime can be described, not in terms of the scaling variable used by LSF, but in terms of a scaled pressure variable, in the limit that pressure goes to zero and system size goes to infinity keeping the product finite.

In this scaling regime, we observe a new phase transition at a finite non-zero value of the scaled pressure, distinct from the zero pressure continuous phase transition. The order of the phase transition depends on the exact model used to represent the two-dimensional ring. When the beads are connected by harmonic springs with a hard cut-off at the maximum value of the bond length, we observe a first order transition separating the self-avoiding phase from the fully inflated phase. However, if the beads are connected by springs with a logarithmic potential such that the potential becomes infinite at the maximal bond length, the order of the phase transition changes, and there is now a continuous second order transition between the two phases.

The problem is studied through a careful scaling analysis and the scaling pre-

dictions are verified by extensive Monte Carlo simulations. Thus our work shows that there a new scaling regime in a scaled pressure variable, and that such a scaling regime describes a phase that is inaccessible to the LSF scaling function. Further, we prove the existence of a new finite pressure phase transition in this regime.

List of publications :

1. Mithun K. Mitra, Gautam I. Menon, R. Rajesh
"Thermodynamic Behaviour of Two-dimensional Self-avoiding Vesicles."
(Manuscript in preparation).

2. Mithun K. Mitra, Gautam I. Menon, R. Rajesh
"Asymptotic Behaviour of Inflated Lattice Polygons."
Journal of Statistical Physics, Vol. 131 (3), 393-404 (2008)
arXiv:0710.1509v1 [cond-mat.stat-mech]

3. Mithun K. Mitra, Gautam I. Menon, R. Rajesh
"Phase Transitions in Pressurised Semiflexible Polymer Rings."
Physical Review E, Vol. 77, 041802 (2008)
arXiv:0708.3318v1 [cond-mat.stat-mech]

Contents

List of Figures

1 Introduction

1.1 Amphiphilic membranes

Amphiphilic molecules are lipids that consist of two distinct parts, a hydrophilic head and a hydrophobic tail. Such molecules self-assemble into a remarkable variety of structures. A common structure formed by amphiphilic molecules is a bilayer, in which the hydrophobic tails of the two layers are in contact with each other, exposing the hydrophilic heads to the solution. In a solution, these bilayers typically close on themselves to form fluid vesicles. This further reduces the hydrophobic energy cost by not exposing any free hydrophobic edges to the solution. Although the bilayer itself is very thin, of the order of nanometers, the vesicles themselves can be huge, reaching dimensions of 100 micrometers. Such vesicles are soft, exhibiting a huge variety of shapes depending on external parameters such as temperature and osmotic pressure. Vesicles are ubiquitous in biological systems, playing a role in a wide range of functions such as trafficking in cells, and the segregation of different biochemical components. There has also been a huge interest in them from a condensed matter point of view because of their unique material properties and the enormous number of shapes and shape transitions that they exhibit. Fluid vesicles are toy models for actual biological vesicles. However, it should be remembered that real biological membranes are enormously complex structures that consist not only of these amphiphilic molecules but also of a variety of other molecules such as proteins and cytoskeltal filaments. Hence, the results obtained from a physical study of fluid vesicles should be applied judiciously to real biological systems.

1.2 Theory of vesicle shapes

The shapes of fluid vesicles are fundamentally different from ordinary interfaces since they are determined by the curvature free energy, and not by interfacial surface tension. This accounts for the great variety of shapes observed in vesicles, in contrast to the spherical shapes governed by isotropic surface tension. The theory of equilibrium shapes of fluid vesicles was worked out by Canham [8], Helfrich [23] and Evans [11] who realised that such shapes could be understood in terms of energy minimising configurations of a curvature hamiltonian, under the constraints of fixed enclosed volume and surface area.

The vesicle membrane is conventinally modeled as a two-dimensional sheet, that is, it is assumed that the membrane thickness is much smaller compared to the dimensions of the vesicle and also its fluctuations. The free energy of such a fluid membrane is determined by its shape alone. The shape is denoted as a geometrical surface. The curvature of the surface can then be described by two quantities, the mean curvature H and the gaussian curvature K. The free energy of the surface is then given by

$$\mathcal{H}_{el} = \int_S dA \left[\frac{\kappa}{2}(H - H_0)^2 + \bar{\kappa} K \right]. \tag{1.1}$$

Here dA is the area element and the coefficients κ and $\bar{\kappa}$ are known as the rigidity and the Gaussian rigidity respectively. The parameter H_0 represents the spontaneous curvature of the membrane.

The equilibrium shapes can then be calculated from a variational approach. If the vesicle is assumed to be incompressible and impermeable, the minimization problem to solve is

$$\delta \mathcal{H}_{el} = 0, \tag{1.2}$$

under the constraints, $A = const$ and $V = const$. The major success of such an approach was that it was able to reproduce the discocyte shapes that were observed in red blood cells (RBC). Also changing the physical parameters induced transitions among the various shapes.

Such a purely mechanical analysis is insufficient to understand the full behaviour of fluid vesicles if the rigidity parameter κ is of order $k_B T$. In this case

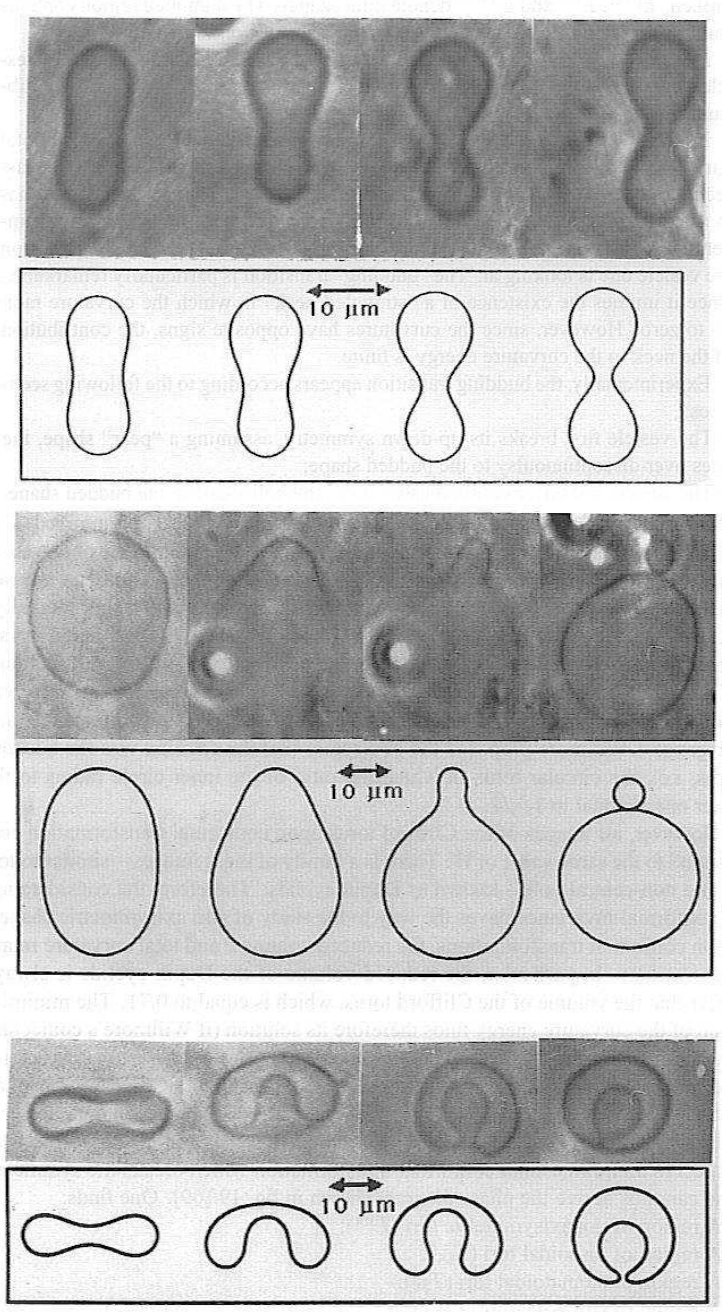

Figure 1.1: Demonstration (1) of a budding transition; (2) symmetric-asymmetric reentrant transition; (3) discocyte-stomatocyte transition. Vesicles of DMPC in water: the reconstructed trajectories in (v, m) space correspond to the dotted lines in the previous figure. From K. Berndl, J. Käs, R. Lipowsky, E. Sackmann, U. Seifert, in L. Peliti (ed.) *Biologically Inspired Physics* (New York: Plenum, 1991).

thermal fluctuations play an important role in the full description of the shape of vesicles. In order to understand the full thermodynamic behaviour such vesicles, we need to write down the partition function and then determine the relevant thermodynamic averages. The partition function in this case is given by,

$$\mathcal{Z} = \int D\vec{r} \exp[-\mathcal{H}_e l/k_B T]\delta(...), \tag{1.3}$$

where the integration is done over all possible configurations of random surfaces and the delta function enforces the necessary constraints, such as those of constant area and constant volume. This partition function is hard to evaluate, and thus the problem of shape transitions in fluid vesicles is a formidable one.

1.3 Two-dimensional vesicles

Given the complexity of understanding the full solution of the three-dimensional vesicle problem, one studies comparatively simpler systems that may nevertheless illuminate many features of the full system. One obvious simplification to make is to consider the statistical mechanics of two-dimensional vesicles, in which the vesicle is modeled as a polymer ring embedded in two-dimensions. The first studies of this type of model were carried out by Leibler, Singh and Fisher (LSF)[27].

LSF model the two-dimensional vesicle as a ring of N impenetrable circular beads of diameter a. The chain is self-avoiding, i.e. the beads cannot overlap each other. The centers of the beads are connected by tethers of length $l_0 > a$. The tethers also have an upper bound on their length, $l_0 < 2a$ to enforce the self-avoidance constraint. The two key features of the problem are the presence of a curvature term in the energy and a finite pressure difference Δp between the interior and the exterior of the ring due to the osmotic pressure. A net outward pressure which tries to inflate the ring corresponds to a positive Δp, while a net inward pressure which tries to collapse the ring corresponds to a negative Δp.The bending energy in the LSF model is given by

$$E_b = \frac{\kappa}{a} \sum_{i=1}^{N} (1 - \cos\theta_i), \tag{1.4}$$

where κ is the bending rigidity, and θ_i is the angle between the i^{th} and $(i+1)^{th}$ bonds. The pressure couples to the area of the ring, via

$$E_p = A\Delta p. \tag{1.5}$$

The system is characterised by a continuous phase transition at $\Delta p = 0$, which separates a branched polymer phase for negative pressures from an infalted phase for positive pressures. At the transition point the ring is described by a self-avoiding walk. LSF performed Monte Carlo simulations to study the variation of the size and enclosed areas for the different parameter regimes described by the pressure and the bending rigidity.

For the problem with zero bending rigidity, $\kappa = 0$, with a non-dimensionalised pressure defined by $p = \Delta p a^2/k_B T$, the radius of gyration R_G and the area A are described by the scaling relations,

$$R_G^2 \sim N^{2\nu} X(pN^{\phi\nu}), \quad A \sim N^{2\nu_A} Y(pN^{\phi\nu}), \tag{1.6}$$

and the various exponents were found through simulations to be, $2\nu = 0.755 \pm 0.018$, and $\nu/\nu_A = 1.007 \pm 0.013$, which suggests that $\nu = \nu_A$. Also, it was found that $\phi = 2.13 \pm 0.17$. This is close to the theoretically expected value of $\phi = 2$, which can be argued from the fact that the pressure couples to the area, and the area scales as $A \sim N^{2\nu}$. Thus the only combination in which the pressure enters the scaling function should be $x \sim pN^{2\nu}$.

Thus, at the crtical point $p = 0$, the polymer ring behaves like a self-avoiding walk. LSF determined the values of the scaling functions at this point to be $X(0)/a^2 = 0.116 \pm 0.008$ and $Y(0)/a^2 = 0.29 \pm 0.02$. They thus concluded that there was no area collapse at this point, for which $A/R_G^2 \to 0$ as $N \to \infty$. For negative values of the pressure, $p < 0$, there is a deflated regime and the ring collapses to form a branched polymer phase. The scaling functions in this regime were found to behave as $X(x) \approx X_-/x^\sigma$ and $Y(x) \approx Y_-/x^\tau$, where, $\sigma = 0.13 \pm 0.05$ and $\tau = 0.25 \pm 0.04$. These values are consistent with a branched polymer phase in the negative pressure regime.

For positive values of the pressure, $p > 0$, the chain assumes a stretched configuration. This inflated regime should also be characterised by definite scaling laws.

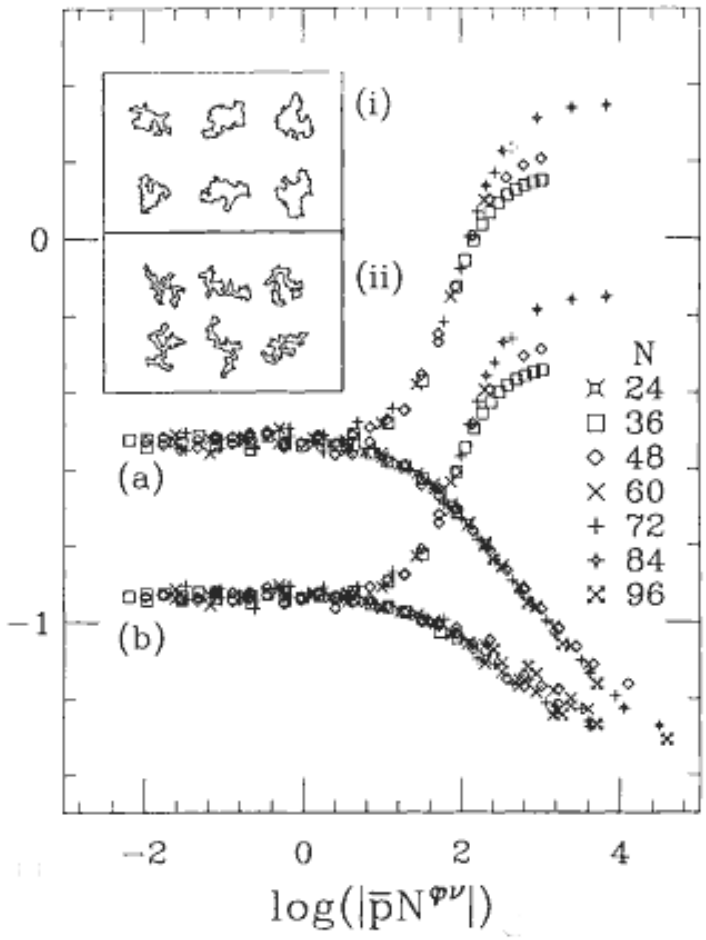

Figure 1.2: Scaling plots and vesicle configurations for rigidity $\kappa = 0$: (a) $\log_{10}(A/N^{2\nu})$ and (b) $\log_{10}(R_G^2/N^{2\nu})$ vs $\log_{10}|pN^{\phi\nu}|$ with $2\nu = 1.51$ and $\phi = 2.13$. Inset shows samples for $N = 60$ with (i) $p = 0$, (ii) $p = -1.25$. Reproduced from Leibler, Singh and Fisher [27].

For large values of Δp, the vesicles approach a circular shape, and thus one has $A \sim R_G^2$. This implies that

$$X(x) \approx X_+ x^{2\omega}, \quad Y(x) \approx Y_+ x^{2\omega}, \tag{1.7}$$

as $x \to \infty$. In addition, due to the circular nature of the vesicle at high pressure, the relation

$$\tilde{\pi} \equiv \frac{\langle A \rangle}{\langle R_G^2 \rangle} \to \frac{Y_+}{X_+} \approx \pi \tag{1.8}$$

should hold asymptotically as $x \to \infty$. Although LSF could not access this regime due to equilibration issues, they conjectured that the area should follow the scaling relation, $A \sim N^2 p^{(1/\nu)-1}$. This implies a value of $\omega = 1/6$. However, a later analysis due to Maggs et. al. [31] showed that this value was in fact erroneous and the stretched regime in this case should be described by $\omega = 1/2$.

We now reproduce the derivation of this $\omega = 1/2$ result as presented in Ref. [31]. We write down the relevant terms in the free energy function in the positive pressure region, where the chain is in an inflated state. One contribution to the free energy is from the pressure difference term,

$$F_p = -\Delta p A \approx -\pi \Delta p R^2, \tag{1.9}$$

where the assumption made is that the shape of the vesicle in the inflated regime can be approximated by a circle of radius R, and hence that the area can be expressed as $A \sim \pi R^2$. The term opposing this in the free energy represents the streching free energy of the polymer chain. In the inflated regime, the perimeter of the vesicle is highly streched and we can represent the perimeter by m linear and independant segments each consisting of $M = N/m$ beads. The length of each segment is given by $R_M = 2\pi R/m$. The probability distribution for a self-avoiding walk with an end-to-end vector $\vec{R}_M$ is given by [13]

$$\mathcal{P}(\vec{R}_M) \approx M^{-d\nu} P(R_M/\bar{a}M^{\nu}), \tag{1.10}$$

where P is an universal scaling function. For large values of the argument, the behaviour of the scaling function is given by [13]

$$P(y) \sim \exp(-c_d y^{\delta}), \quad \text{with} \quad \delta = \frac{1}{1-\nu}, \quad y \gg 1 \tag{1.11}$$

where c_d is some constant. The stretching free energy for any one segment is then given by,

$$F_M \approx c_d k_B T R_M^{\delta}/\bar{a}^{\delta} M^{\delta\nu}. \tag{1.12}$$

The full stretching free energy for the entire chain is then given by

$$F_N \approx m F_M \approx \bar{c}_d k_B T R^{\delta}/a^{\delta} N^{\delta\nu}, \tag{1.13}$$

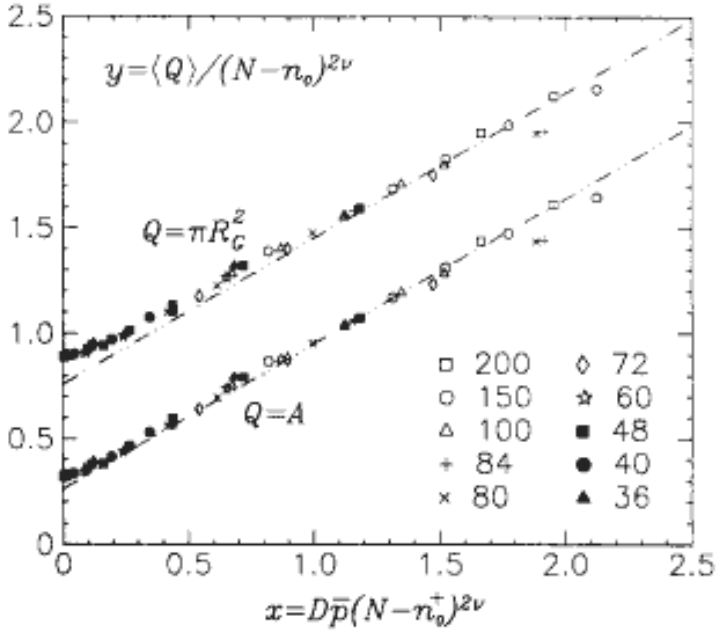

Figure 1.3: Scaling plot of data for the area and square radius if gyration of two-dimensional vesicles of N beads demonstrating the asymtotically linear behavior of the scaling functions $X(x)$ and $Y(y)$ for $\pi\langle R_G^2\rangle$ and $\langle A\rangle$ respectively. Units of a^2 have been used for R_G^2 and A. Note that the plot for $y = \langle \pi R_G^2\rangle/(N-n_0)^{2\nu}$ has been shifted upwards by $\Delta y = 1/2$ for clarity. The asymptotically negligible N shifts $n_0 \approx 0.5$ and $n_0^+ = 9$ have been incorporated to hasten convergence when $N \to \infty$ at fixed x. Reproduced from Maggs et. al. [31].

where, $\bar{c}_d \approx (2\pi a/\bar{a})^\delta c_d$, is independent of the number of segments m. The full free energy in the stretching limit is then given by

$$F = F_N + F_p \sim \frac{R^\delta}{N^{\delta\nu}} - pR^2. \tag{1.14}$$

The average value of the radius of the ring can now be found by minimizing the free energy as a function of R. This gives,

$$\langle R(N,p)\rangle \approx N^{\nu_+} p^\omega, \tag{1.15}$$

where,

$$\nu_+ = \frac{\nu}{2\nu-1}, \quad \omega = \frac{1-\nu}{2\nu-1}. \tag{1.16}$$

For two-dimensions, we have $\nu = 3/4$. This gives the values $\nu_+ = 3/2$ and $\omega = 1/2$. Thus, this implies that in the inflated regime, the area of the rings should scale as

$$\langle A \rangle \sim \langle R^2 \rangle \sim N^3 p. \tag{1.17}$$

Thus in the inflated regime of this scaling limit, the area of the ring grows as N^3 and not N^2 as suggested in Ref. [27]. Simulation data that confirm these exponents is shown in Fig. 1.3. These exponents, however, are valid only in the scaling regime about the $p = 0$ transition. When the ring inflates to its maximal size, $2\pi R \approx Na$, these relations will no longer be valid and the radius of the ring must necessarily scale with the number of monomers. Thus this analysis is valid only in the regime

$$N^{3/2} \ll p \ll N^{-1}. \tag{1.18}$$

Later in this thesis, we shall revisit the scaling hypothesis for the truly inflated regime and attempt to provide a coherent description of the ring in this region.

For non-zero values of the bending rigidity κ, the shape of a vesicle is determined by the interplay between two length scales, the rigidity length $l_\kappa = \kappa/k_B T$, and an expansile length $l_p^2 = k_B T/\Delta p$. For small positive values of κ and $\Delta p > 0$, the only effect is a rescaling of the effective bead size a, while with increasing κ, one enters a stiff regime. More marked effects are observed in the negative pressure regime $\Delta p < 0$. Here, with increasing values of κ, the many sharp bends which characterise the branched polymer phase become energetically unfavourable. When $\rho^* \equiv (l_\kappa l_p^2)^{1/3} \leq L$, one observes well-defined equilibrium shapes as found in red blood cells [27]. Moreover, LSF also observed a striking dynamic phenomena, in which at $\Delta p < 0$ and for some range of κ or T, the vesicle shape shape exhibited a nonlinear flickering phenomena which is also seen in RBCs. The vesicle oscillated between two or more characteristic cytotype shapes, spending large times in any one shape followed by a quick transition to another characteristic shape. The typical vesicle shapes and the nonlinear flickering phenomena as seen in the simulations are shown in Fig. 1.4.

In addition to scaling exponents, another important quantity that helps to quantify the shape of the vesicle is the anisotropy ratio. For a given shape of a vesicle, if the minimum and maximum eigenvalues of the radius of gyration tensor

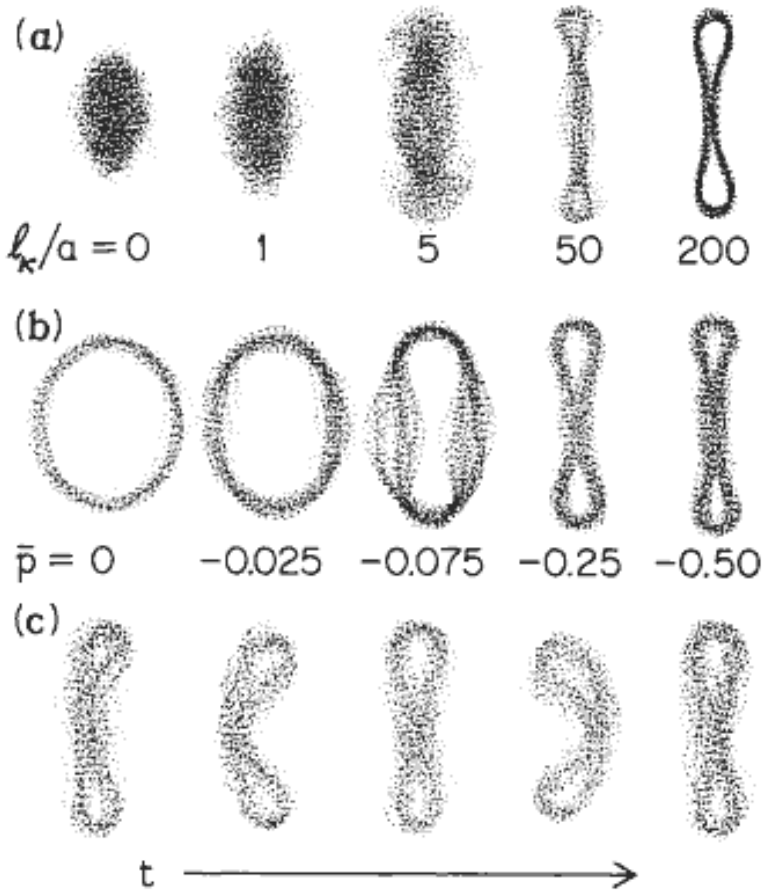

Figure 1.4: Vesicle cytotypes for (a) $p = -1.25$ as $l_\kappa/a \equiv \kappa/ak_BT$ increases; (b) $l_\kappa/a = 50$; and (c) as a function of time t, fpr $p = -0.075$ and $l_\kappa/a = 10$. Reproduced from Leibler, Singh and Fisher [27].

are denoted by $R_{G,min}$ and $R_{G,max}$ respectively, then the anisotropy can be defined as

$$\tilde{\Sigma} = \langle \frac{R^2_{G,min}}{R^2_{G,max}} \rangle. \tag{1.19}$$

Another definition alternatively used in the literature is to define

$$\Sigma = \frac{\langle R^2_{G,min} \rangle}{\langle R^2_{G,max} \rangle}. \tag{1.20}$$

For the LSF model, variation of the anisotropy Σ was measured as a function of the scaling variable $x \propto pN^{\phi\nu}$, with $\phi = 2$ and $\nu = 3/4$ [7]. In the limit $N \to \infty$,

the asymptotic values in the various regimes were found to be

$$\Sigma_0 = 0.393 \pm 15, \quad p = 0, \tag{1.21}$$

$$\Sigma^- = 0.230 \pm 10, \quad p = -\infty, \tag{1.22}$$

while in the inflated regime $\Sigma^+ = 1$ for $p = +\infty$ corresponding to circular vesicle shapes. They found that the anisotropy values changed continously from these asymptotic values as the scaling variable x was varied continuously.

In Chapter 4 of this thesis, we shall make a detailed study of the inflated phase of self-avoiding rings. We determine the relevant pressure variable that descibes the ring in the inflated phase and address the question of whether there is any interesting behaviour as a function of this suitably defined scaled pressure.

1.4 Lattice vesicles

One interesting version of the vesicle problem is to study the behaviour of lattice polygons. The polygon is assumed to lie on an underlying lattice and thus the excluded volume parameter is set by the lattice spacing. The lattice polygon is taken to model the perimeter of the vesicle and one can then ask similar questions as is posed for the continuum case, such as the variation of the area with the pressure. The polygon can be taken to be self-avoiding, which then defines the analog of the LSF model in the lattice case.

We shall briefly review here the basic known results for lattice polygons. Let $p_N(A)$ denote the number of polygons of perimeter N enclosing an area A. The basic quantity is then the perimeter and area generating function G(x,q), or the 'grand partition function', defined as

$$G(x,q) = \sum_{N,A} p_N(A) x^N q^A, \tag{1.23}$$

where, x and q are the fugacities associated with the perimeter and area respectively. Identification with the vesicle problem is achieved by recognising the area fugacity to be the exponential of the pressure, $q \equiv e^p$. The thermodynamical properties of polygons can thus be determined by studying the behaviour of this

generating function about its singular points.

We can also define the perimeter generating function and the area generating function as

$$P_N(q) = \sum_A p_N(A) q^A, \tag{1.24}$$

$$S_A(x) = \sum_N p_N(A) x^N. \tag{1.25}$$

The perimeter generating function $P_N(q)$ is the lattice equivalent of the partition function for the continuum version of the vesicle problem. For this generating function, it can be shown that one can define a free-energy like limit [15],

$$\tilde{\kappa}(q) \equiv \lim_{N\to\infty} \frac{P_N(q)}{N}. \tag{1.26}$$

More specifically, one can show [15] that $\tilde{\kappa}(y)$ exists and is finite for all values of $y \leq 1$. In this region, $\tilde{\kappa}(y)$ can be shown to be log-convex and continuous. For the region $y > 1$, this free-energy function $\tilde{\kappa}(y)$ is infinite. The average area as a function of the area fugacity (or equivalently, pressure) q, is defined as

$$\langle A \rangle_N(q) = \frac{\sum_N A p_N(A) q^A}{\sum_N p_N(A) q^A} \equiv \frac{\partial \log P_N(q)}{\partial \log q}. \tag{1.27}$$

The area function is then defined as $k_N(q) = \frac{\langle A \rangle_N(q)}{N^2}$. In the region $q > 1$, for asymptotically large polygons, we can show that the area function is finite and has the value 1/16, i.e.

$$\lim_{N\to\infty} \frac{\langle A \rangle_N(q)}{N^2} = \frac{1}{16}. \tag{1.28}$$

This value is independent of q and the qualitative change occurs for all $q > 1$. This implies that for any infinitesimal pressure $p > 0$ in the thermodynamic limit, the vesicle inflates to a square configuration.

The two-variable generating function can then be written in terms of the single variable generating functions as

$$G(x, q) = \sum_N P_N(q) x^N = \sum_A S_A(x) q^A. \tag{1.29}$$

The phase diagram for this model in the two-dimensional phase space defined by the two fugacities was first studied by Fisher, Guttmann and Whittington [15]. They showed that for all $q < 1$, $G(x, q)$ converges for $x < e^{-\tilde{\kappa}(q)}$ while for $q > 1$, $G(x, q)$ converges only if $x = 0$. For $q < 1$ and $x < e^{-\tilde{\kappa}(q)}$, the generating function is dominated by polygons of minimal area and one obtains branched polymers in this region. This phase is known as the compact phase. For $q > 1$ and $x > e^{-\tilde{\kappa}(q)}$, we have a single convoluted polygon that fills the entire lattice like a closed Hamiltonian walk. This phase is called the seaweed phase. At $q = 1$, one obtains standard self-avoiding polygons (SAP), while for positive q, $q > 1$, the polygons enter an inflated phase, where the shapes become approximately squares. The average area in this regime scales as the square of the perimeter, as discussed previously. This phase diagram of lattice polygons is shown in Fig. 1.5.

The phase boundary in the region $q < 1, x > x_c$ terminates at a bicritical point at $(x_c, 1)$. The phase boundary is characterised by a logarithmic singularity, when approached from below. Around this bicritical point, one expects a generic scaling form of the perimeter and area generating function to hold. Remarkably, this scaling function was computed exactly through q-algebraic techniques [39] and also verified through a field-theoretic approach [9] to be the logarithm of an Airy function, in what is one of the very few known examples of an exact scaling function for a nontrivial isotropic critical point.

In the vicinity of the bicritical point ($(x, q) \to (x_c^-, 1^-)$), the perimeter and area generating function is expected to display a scaling behaviour of the form [39, 40]

$$G(x, q) \sim G^{(reg)}(x, q) + (1 - q)^{\theta} F\left(\frac{x_c - x}{(1 - q)^{\phi}}\right), \tag{1.30}$$

where $G^{(reg)}$ is the regular part of the generating function at the bicritical point and $F(S)$ is the scaling function with critical exponents θ, ϕ. In analogy with the case of simpler polygon models, such as staircase polygons, the perimeter and area generating function for rooted self-avoiding polygons (SAPs that pass through a given point) is assumed to satisfy an q-algebraic functional equation of arbitrary degree N,

$$\sum_{n=1}^{N} \sum_{k_1,\ldots,k_n} (x, q) \prod_{i=1}^{n} G(q^{k_i} x, q) = b(x, q). \tag{1.31}$$

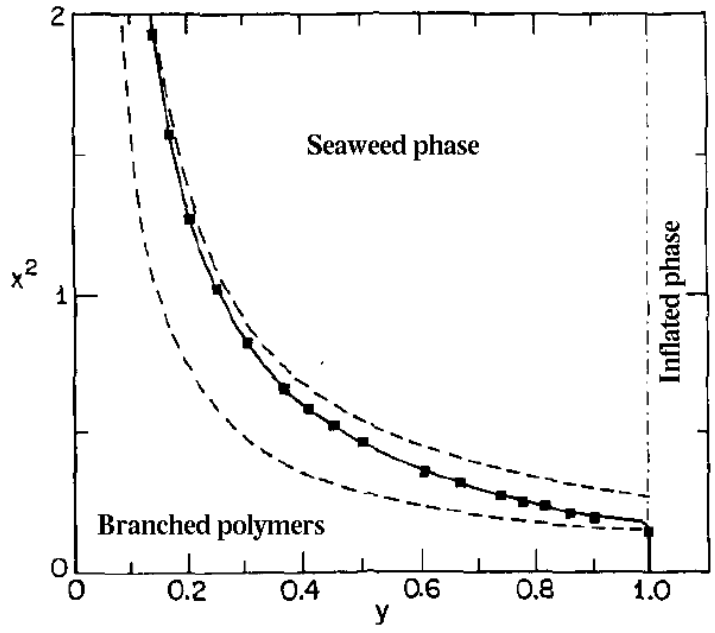

Figure 1.5: Plot of the phase boundary $q_c(x)$, or, equivalently, $x_c(q)$: solid squares; the curve is merely a guide to the eye. The series expansions for the generating function $G(x, q)$ converge on the origin side of the phase boundary and on the vertical piece at $q = 1$; this region defines the droplet or compact phase. For $q > 1$ the polygons are higly expanded; for $q < 1$ but above the phase boundarym a seaweed-like phase is anticipated. The broken curves denote upper and lower bounds for the phase boundary. Reproduced from Fisher, Guttmann and Whittington [15].

This assumption then implies that the scaling solution F(s) for rooted SAPs follows the Riccati differential equation with a solution

$$F^{(r)}(s) \propto \frac{d}{ds} \ln \mathrm{Ai}(s) \tag{1.32}$$

where $\mathrm{Ai}(s)$ is the Airy function, and also leads to values of the critical exponents as $\theta = 1/3, \phi = 2/3$. The scaling function of general (unrooted) self-avoiding polygons can then be determined from the rooted polygon answer through integration. The singular part of the generating function is given by [40]

$$G^{(sing)}(x, q) \sim (1 - q)F\left(\frac{x_c - x}{(1 - q)^{2/3}}\right) + C(q), \quad (x, q) \to (x_c, 1), \tag{1.33}$$

where $C(q)$ is a constant of integration given by

$$C(q) \sim (1-q)\ln(1-q), \tag{1.34}$$

and the scaling function is given by

$$F(s) \propto \ln \mathrm{Ai}(a). \tag{1.35}$$

Extensive numerical analysis was used to verify this form of the scaling function. It was subsequently pointed out [9], that the emergence of the Airy function can also be understood from a field-theoretic approach, in which the crossover from self-avoiding loops to branched polymers is analyzed from each end, using the methods of continuum field theory.

There has also been some work on the asymptotic behaviour of the scaling function in the inflated regime, $q > 1$. For the perimeter generating function $P_N(q)$, it was shown that for SAPs in two-dimensions [35]

$$P_N(q) = A(q)q^{N^2/4}(1+\mathcal{O}(\rho^N)), \quad \text{as } n \to \infty, \tag{1.36}$$

for some $0 < \rho < 1$. The leading asymptotic behaviour of $P_N(q)$ is given by

$$P_N(q) = \frac{(1+\mathcal{O}(\rho^N))}{(q^{-1};q^{-1})_\infty^4} \sum_{k=-\infty}^{\infty} q^{k(n-k)}. \tag{1.37}$$

Here,

$$(x;q)_m =^{def} \prod_{k=1}^{m}(1-xq^{k-1}) \tag{1.38}$$

is the standard q-product notation.

The polynomial $A(q)$ has different expressions $A_o(q)$ and $A_e(q)$ when N is restricted to subsequences with N being odd or even respectively. Explicit expressions for these coefficients can be calculated as

$$A_o(q) = \frac{\sum_{k=-\infty}^{\infty} q^{-(k+1/2)^2}}{(q^{-1};q^{-1})_\infty^4} \tag{1.39}$$

$$A_e(q) = \frac{\sum_{k=-\infty}^{\infty} q^{-k^2}}{(q^{-1};q^{-1})_\infty^4}. \tag{1.40}$$

There is an essential singularity in both the $A(q)$ functions as q approaches 1 from above. It was shown that [35]

$$A(q) \sim A_o(q) \sim A_e(q) \sim \frac{1}{4}(\frac{\epsilon}{\pi})^{3/2} e^{2\pi^2/3\epsilon} \quad \text{as } q \to 1^+, \tag{1.41}$$

where $\epsilon = \ln(q)$.

In Chapter 3 of this thesis, we shall provide an analytic calculation for the area of lattice polygons in the inflated regime. We derive the result exactly for convex and column-convex polygons, and it is found to hold true for self-avoiding polygons also, thus providing one of the few analytic results for self-avoiding polygons.

1.5 Self-intersecting rings

The two-dimensional self-avoiding model as introduced by Leibler, Singh and Fisher [27] although much simpler than the full three-dimensional problems, still admits no analytic approach, due to the self-avoiding nature of the beads. Rudnick and Gaspari [42] noted that relaxation of the self-avoiding constraint simplified the problem such that it became analytically tractable. Such a model, although physically unrealistic, yields useful insight into the self-avoiding problem. Further, in certain regimes, such as the inflated ring regime of the LSF problem, it is expected that the self-avoidance does not an important role and hence in such a scenario, the present model serves as a useful approximation to the true answer.

The Rudnick Gaspari (RG) model is pictured as a closed ring consisting of N linear links. The links are allowed to intersect each other. In the absence of a pressure differential, the length of the links or bonds follow simple gaussian statistics. If the mean length of a link is denoted by Δ^2, then the probability distribution governing the length of a link η is then given by

$$P(\eta) = \left(\frac{1}{\Delta^2 \pi}\right)^{1/2} \exp(-\eta^2/\Delta^2). \tag{1.42}$$

Note that in this model, the length of the links are not bounded and they can stretch to infinte length. We shall refer to this model as the Extensible Self-Intersecting (ESIR) model. The probability distribution of any shape specified by

a set of displacements η_α is then given by the product

$$\prod_{\alpha=1}^{N}\prod_{i=1}^{2} P(\eta_{\alpha i}), \tag{1.43}$$

where the sum over i is due to the fact that the bonds are in fact two-dimensional vectors. In the presence of a non-zero osmotic pressure difference Δp between the inside and the outside of the ring, there is an additional Boltzmann factor

$$\exp\left(\frac{\Delta p A}{k_B T}\right), \tag{1.44}$$

where A denotes the oriented or signed area enclosed by the ring. Thus in this case, the area of the ring can in fact be zero or negative. The replacement of the true area by the signed area is an important approximation of this model. However, this substitution is not expected to affect the results for large positive pressures, since intersections of the ring are not expected to persist in this regime. However, negative pressure are inaccessible in this model, since changing the sign of the pressure is equivalent to changing the sense of the area vector, without any real change in the shape of the ring. The fact that the ring is closed implies that the sum of the bond vectors should be zero, which leads to the two constraint equations

$$\sum_{\alpha=1}^{N} \eta_{\alpha i} = 0 \quad i = 1, 2. \tag{1.45}$$

The full probability distribution can then be written as

$$P(\eta_1, \eta_2, ...) = \frac{1}{Z}\exp\left(-\sum_{\alpha}(\eta_{\alpha x}^2 + \eta_{\alpha y}^2) + \frac{p}{2}\sum_{\alpha,\alpha'}\eta_{\alpha x}\eta_{\alpha y}\phi(\alpha - \alpha')\right), \tag{1.46}$$

where, p is defined as the dimensionless pressure $p \equiv \Delta^2(\Delta p/k_B T)$ and ϕ is the step function. The quantity Z is the partition function for the problem and normalizes the probability. The addition of the pressure differential leaves the gaussian form of the probability distribution unaltered and hence the partition function and other thermodynamic quantities can be calculated exactly. The normalization can be

calculated to be [18]

$$\begin{aligned} Z^{-1} &= \prod_k \left(1 - \frac{p^2}{4k^2}\right), \\ &= \frac{\sin \pi x}{x}, \end{aligned} \tag{1.47}$$

where, $x = pN/4\pi$. Thus the model predicts that the area of the vesicle blows up to infinity at a critical value of the pressure, $p_c = 4\pi/N$. The expectation value for the mean square radius of gyration R_G can be calculated to be

$$\langle R_G^2 \rangle = \frac{\Delta^2}{\pi p_c} \left(\frac{1}{x^2} - \frac{\pi}{x} \frac{1}{\tan \pi x} \right). \tag{1.48}$$

Thus if we define a scaled pressure as $\hat{p} = pN/4\pi$, then in this scaled pressure axis, there occurs a phase transition at a constant value $\hat{p} = 1$ independant of the system size at which the area of the ring blow up. Such a finite pressure transition is a new feature of this model, in variance with the results of the LSF model, where only a zero pressure transition was found. We shall revisit this result in the context of the LSF model and its variants in our thesis.

The ESIR model has the drawback that the inflated regime is inaccessible because the ring blows up to infinity at the critical point. This is an artefact of the infinite extensibilty of the constituent links of the model, which is clearly unphysical. A more physically realistic model would have to take into account the fact that the bonds should have a maximum bond length and thus should reach some maximum possible area in the inflated regime. To incorporate this fact, we define a modified version of the ESIR model, in which the polymer ring is modelled as a closed, freely-jointed chain of N monomers where the monomers are connected by rigid links of length l [21]. This is called the Inextensible Self-Intersecting Ring (ISIR) Model. The probability of a specific configuration η_j is then denoted by

$$P(\eta_j, p) \propto e^{pA[\eta_j]} \prod_{j=1}^{N} \delta(|\eta_j - \eta_{j-1}| - 1), \tag{1.49}$$

where, as in the ESIR model, the area A is the geometric or signed area of the ring, and $l \equiv 1$ is defined as the unit length. The model was analysed in the mean-

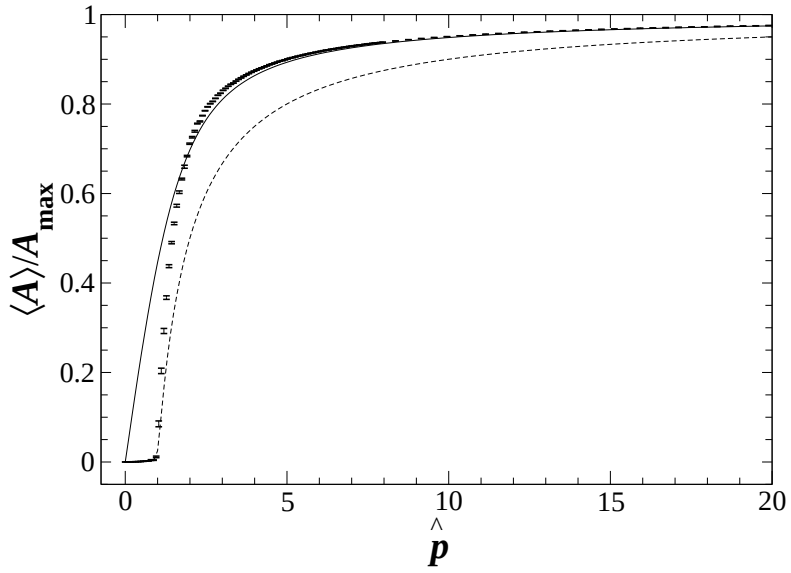

Figure 1.6: Mean area (scaled by $A_{\max}$) as a function of pressure (scaled by p_c), as obtained by the zeroth-order transfer-matrix calculation (solid curve), mean-field approximation (dashed curve), and MC simulations for $N = 1600$ (error bars). Reproduced from Haleva and Diamant [21].

field limit, where the rigid rods were replaced by harmonic springs, and the spring constant λ was determined self-consistently in the mean-field spirit by setting the average link length to 1. The partition function can be calculated using the same method as the ISIR model to be

$$Z(p, N, \lambda) = \frac{1}{\lambda^N} \frac{Np}{4\lambda \sin(Np/4\lambda)}. \tag{1.50}$$

The mean area is then determined by differentiating with respect to the pressure p,

$$\langle A(p, N, \lambda) \rangle = \frac{\partial \ln Z}{\partial p} = \frac{1}{p} - \frac{N \cot(Np/4\lambda)}{4\lambda}. \tag{1.51}$$

The spring constant is determined from the consistency equation

$$\langle (\eta_j - \eta_{j-1})^2 \rangle = -\frac{1}{N} \frac{\partial \ln Z}{\partial \lambda} = 1. \tag{1.52}$$

It can be shown that in the thermodynamic limit, $N \gg 1$, the spring constant λ

can be described by the continuous but non-analytic function [21]

$$\lambda(\hat{p}, N \to \infty) = \begin{cases} 1 & \hat{p} < 1 \ , \\ \hat{p} & \hat{p} > 1 \ . \end{cases} \tag{1.53}$$

Thus for this model also, there exists a phase transition about the critical pressure value $\hat{p} = pN/4\pi = 1$. In the thermodynamic limit, the behaviour of the area around the critical point can be obtained as

$$\langle A \rangle = \begin{cases} \frac{N}{4\pi}\frac{1}{\hat{p}(1-\hat{p})} \overset{\hat{p}\to 1^-}{\longrightarrow} \frac{N}{4\pi}\frac{1}{1-\hat{p}}, & 1-\hat{p} \gg N^{-1/2} \ , \\ \frac{N^{3/2}}{4\pi}, & |1-\hat{p}| \ll N^{-1/2} \ , \\ \frac{N^2}{4\pi}\frac{\hat{p}-1}{\hat{p}} \overset{\hat{p}\to 1^+}{\longrightarrow} \frac{N^2}{4\pi}(\hat{p}-1), & \hat{p}-1 \gg N^{-1/2}. \end{cases} \tag{1.54}$$

Thus there is a continuous phase transition with mean-field exponents across the critical point $\hat{p} = 1$ with the vesicle going from a crumpled phase below the transition to an inflated phase above the transition. This result was also verified using transfer matrix calculations and Monte Carlo simulations [21] as is shown in Fig. 1.6.

In addition to characterising the area transition across the critical point, it is also interesting to look at some quantitative measures of shape in the various regimes. Rudnick and Gaspari [17, 18] calculated two such measures, the radius of gyration R_G and the asphericity A_2 for the ISIR model. The basic quantity that contains information about the shape of the ring is the radius of gyration tensor, defined in a compact form as [16]

$$T_{ij} = \Delta^2 \sum_{\alpha\beta} a_{\alpha\beta}\eta_{\alpha i}\eta_{\beta j}, \tag{1.55}$$

with the elements of the symmetric matrix $a_{\alpha\beta}$ defined by

$$\begin{aligned} a_{\alpha\beta} &= \frac{1}{(N+1)^2}\alpha(N+1-\beta) \quad \alpha > \beta, \\ a_{\alpha\beta} &= \frac{1}{(N+1)^2}\beta(N+1-\alpha) \quad \beta > \alpha. \end{aligned} \tag{1.56}$$

For a two-dimensional system, the gyration tensor is a 2×2 matrix with two eigenvalues λ_1 and λ_2. A quantitative estimate of the mean size of the ring is then

provided by the radius of gyration defined as

$$R_G^2 = \lambda_1 + \lambda_2. \tag{1.57}$$

A measure of the deviation of the average shape from the circle is provided by the asphericity, defined as

$$A_2 = \frac{(\lambda_1 - \lambda_2)^2}{(\lambda_1 + \lambda_2)^2}. \tag{1.58}$$

For the ISIR model, expressions for these two shape measures can be calculated analytically [18]. While the expression for the radius of gyration was provided in Eq. 1.48, the asphericity can be calculated to be

$$A_2 = \frac{\frac{8}{p^4} - \frac{N^2}{6p^2} - \frac{2N}{p^3 \tan(Np/4)}}{-\frac{8}{p^4} - \frac{N^2}{6p^2} + \frac{N^2}{2p^2 \sin^2(Np/4)}}. \tag{1.59}$$

The asphericity has a value of $A_2 = 1/3$ for zero pressure and approaches zero as we approach the critical pressure p_c as the vesicle become more and more circular. Additional studies on asphericity measures have also been performed for polymer rings by incorporating semiflexibility effects [1, 28].

We study Self-intersecting rings in Chapter 2 of our thesis. While the phase transition at a finite value of the scaled pressure has been studied in this case, there have not been detailed studies on how semiflexibility affects the transition. We study the self-intersecting ring through both lattice and continuum models and characterise the phase boundary in the bending rigidity – pressure plane, through scaling analysis, mean field theories, Monte Carlo simulations and exact enumeration for the lattice model. We introduce a new approach to the mean field theory in this case, and this method reproduces the simulation results to high accuracy in the inflated phase.

2

Self-intersecting Polymer Rings

2.1 Introduction

In the Introduction (Sec. 1.5) we introduced the general model for self-intersecting rings. These systems present an analytically tractable model which helps us to understand the more complex problem of self-avoiding rings. In addition, as noted previously, in the regime where self-avoidance is not important, the results for self-intersecting rings present an useful approximation to the true answer.

Existing results by Rudnick and Gaspari [42, 18] and Haleva and Diamant [21] showed the presence of a continuous phase transition separating collapsed and inflated phases of the self-intersecting ring. However, these studies were done for flexible polymers, and since bending rigidity often plays an important role in the context of biological systems, it is important to study how the transition is affected or modified by the the presence of semiflexibility.

Furthermore, existing mean-field approaches to the self-intersecting ring problem [21] do not yield quantitatively correct answers for the area in the inflated phase. In this chapter, we present an alternative mean-field approach which gives the correct asymptotic behaviour for the area, even in the presence of nonzero bending rigidity.

We incorporate a bending rigidity cost into the ISIR model (Sec. 1.5) and ask whether the continuous phase transition seen for the flexible self-intersecting rings persists in this case. We show that there is indeed a phase transition in this case also, and characterise the nature of the phase boundary separating the collapsed and inflated phase as a function of the pressure and the bending rigidity.

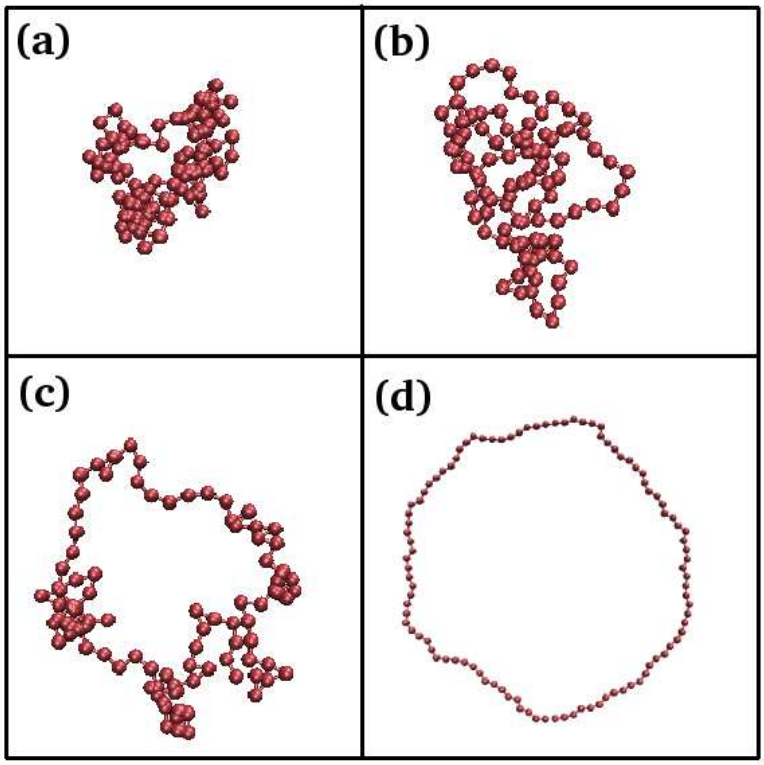

Figure 2.1: The collapsed to inflated phase transition as the pressure is increased. The different panels correspond to (a) $J = 0$, $p < p_c$; (b) $J = 2$, $p < p_c$; (c) $J = 0$, $p = p_c$; and (d) $J = 0$, $p > p_c$.

In the model proposed in this chapter, bending rigidity is incorporated into the ISIR model along standard lines for semiflexible polymers. We retain the coupling of the signed pressure to the algebraic area noting, as argued in [21], that this difference, while vastly increasing the tractability of the problem, makes little difference to computations within the inflated phase.

2.2 Definition of the model

The model is defined as follows. Consider a closed chain of N monomers in two dimensions. Let the positions of the j^{th} particle be denoted by the vector $\vec{r}_j$ and the corresponding tangent vectors by $\vec{t}_j = \vec{r}_{j+1} - \vec{r}_j,\ j = 1, 2, \ldots, N$. For a closed ring, $\vec{r}_{N+1} = \vec{r}_1$, or equivalently, $\sum_i \vec{t}_i = 0$. The algebraic or signed area A_s enclosed by

the ring is given by

$$A_s = \frac{1}{2}\sum_{i=1}^{N}(\vec{r}_i \times \vec{r}_{i+1}) \cdot \hat{z} = \sum_{j=1}^{N}\sum_{k=1}^{j-1}(\vec{t}_k \times \vec{t}_j) \cdot \hat{z}. \tag{2.1}$$

A_s can be either positive or negative.

Coupling this algebraic area to pressure, we obtain the energy term,

$$H_p = -pA_s. \tag{2.2}$$

Importantly, $p \to -p$ is a symmetry of the model, since the pressure term couples to the signed area. The bending energy cost can be written down following standard procedures as

$$H_b = -J\sum_{i=1}^{N}\hat{t}_i \cdot \hat{t}_{i+1}, \tag{2.3}$$

where J is the continuum bending rigidity and $\hat{t}$ is the unit vector in the direction of $\vec{t}$. The inextensibility condition is imposed through

$$|\vec{r}_i - \vec{r}_{i-1}| = |\vec{t}_i| = a = 1. \tag{2.4}$$

Since the tangent vectors have unit norm, we can represent them as $\vec{t}_i = (\cos\theta_i, \sin\theta_i)$, where $\theta \in [0, 2\pi)$. In terms of these variables, the partition function is

$$\mathcal{Z} = \int \prod_i d\theta_i \prod_{j=0}^{N-1}\left(\prod_{k=0}^{j-1} e^{\frac{p}{2}\sin(\theta_k - \theta_j)}\right) e^{J\cos(\theta_j - \theta_{j+1})}. \tag{2.5}$$

We shall refer to this model as the “continuum model".

We also study a lattice version of the same problem with the particles constrained to lie on the vertices of a two dimensional square lattice. The model remains essentially the same except for restrictions on the angles θ_i. Now θ_i is only allowed to take values $0, \pi/2, \pi$, and $3\pi/2$, such that all the particles are on the vertices of the square lattice. We will refer to this version as the “lattice model”. We discuss the differences and similarities between the two versions.

We use a combination of analytic and numerical methods to study these models: Flory type scaling theory for the scaling of the area as a function of pressure,

Monte Carlo simulations for different pressures and bending rigidities, mean field approaches and exact enumerations.

In Fig. 2.1 we show typical configurations obtained from Monte Carlo simulations of the continuum model in four limits. These are configuration snapshots across the collapsed to inflated phase transition, for different values of the bending rigidity J of the continuum model, as the pressure p is varied. Fig. 2.1(a) shows the collapsed phase for the case where the bending energy is zero, while Fig. 2.1(b) illustrates a typical ring configuration at an intermediate value of the bending rigidity, but still within the collapsed regime. In Fig. 2.1(c), we show a typical configuration close to the transition between collapsed and inflated phases. Last, Fig. 2.1(d) illustrates the fully inflated ring.

We summarise our main results below. We show that there is a continuous phase transition in the scaled pressure $\hat{p}$ $(= Np/4\pi)$ – bending rigidity (J) phase diagram, which separates a collapsed phase in which area $\propto N$, from an inflated phase in which area $\propto N^2$ (see Fig. 2.2). The $p \to -p$ symmetry implies the symmetry of the phase boundary upon reflection across the $p = 0$ axis, as shown in Fig. 2.2. The phase boundary for the continuum model is obtained as $\hat{p}_c = [I_0(J) - I_1(J)]/[I_0(J) + I_1(J)]$, where $I(J)$'s are the modified Bessel functions. For the lattice model, the phase boundary is obtained as $\hat{p}_c = e^{-J}$.

These results are obtained by incorporating the effects of a nonzero J into the known exact solution for the $J = 0$ case, through a scaling argument. For the collapsed phase, the free energy for nonzero J is calculated by the same method. In the inflated regime, we resort to mean field approximations. We employ two types of mean-field theories: In the first, the inextensibility constraint is satisfied exactly but the closure condition is satisfied only on average. In the second, we impose the closure condition exactly but satisfy the inextensibility constraint only on average. The dependence of the area on $\hat{p}$ for $\hat{p} \to \infty$ is calculated. The behaviour near the transition line is obtained through a Flory type scaling theory.

The rest of the chapter is organised as follows. Section 2.3 contains the details of the numerical methods used, including the Monte Carlo and exact enumeration algorithms. In Sec. 2.4, we discuss a Flory-type scaling theory valid for the semi-flexible case. Also, here we use the analogy between the extensible polymer and the quantum mechanical problem of the motion of an electron in a magnetic field to reproduce the solution of the problem for $J = 0$ and $\hat{p} < \hat{p}_c$. Section 2.5 describes

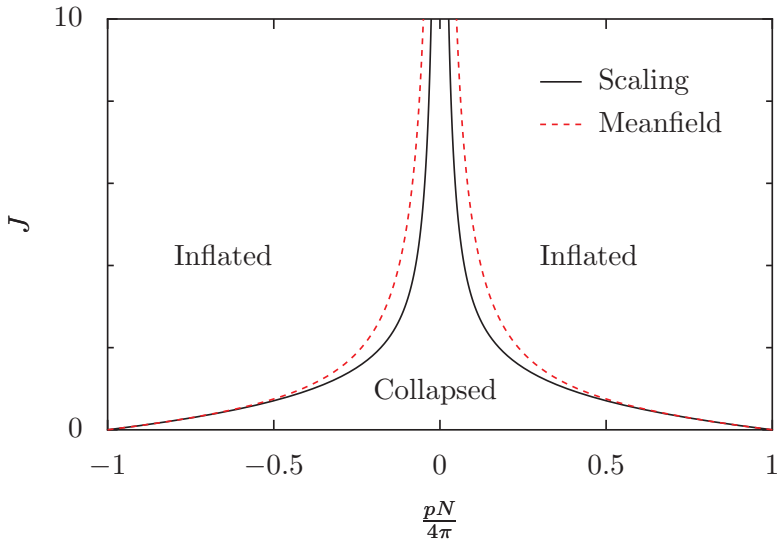

Figure 2.2: The phase boundary between collapsed and inflated phases for a semi-flexible polymer ring as obtained by two different methods, a scaling analysis based on Flory-type arguments and mean-field theory. Note that the $p \to -p$ symmetry of the model implies the symmetry of the phase boundary upon reflection across the $p = 0$ axis. Thus, negative and positive values of the scaled pressure are equivalent, since the pressure term couples to the *signed* area and not to the true area.

mean-field approaches to this problem: (a) a simple density-matrix based single-site mean-field approach which captures the properties of the inflated phase to very high accuracy but is inadequate for the collapsed phase, (b) a less accurate harmonic spring mean-field theory, which is capable of describing both collapsed and inflated phases, and finally, (c) other variational choices that we tried using different zeroth order hamiltonians. In Sec. 2.6, we discuss the behaviour around the critical point in greater detail. Sec. 2.7 contains results for the asymptotic behaviour of the area as well as a description of the appropriate scaling function for the area in the lattice case, as a function of N. Section 2.8 contains a summary and conclusions.

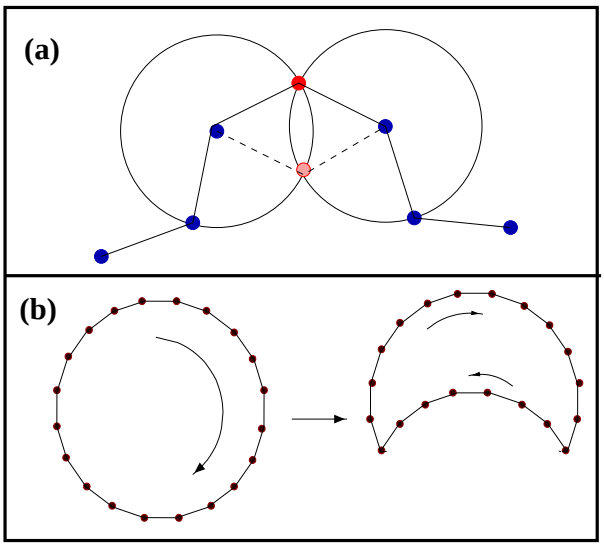

Figure 2.3: A schematic representation of the Monte Carlo moves: (a) single flip; and (b) global flip.

2.3 Numerical method

In this section, we describe the numerical methods used. For the continuum version of our model, we use Monte Carlo simulations (described in Sec. 2.3.1) while for the lattice problem, we use an exact enumeration scheme (described in Sec. 2.3.2). The analytic results we obtain for our model, described in later sections, provide useful benchmarks for the numerical work.

2.3.1 Monte Carlo Simulations

The algorithm for the Monte Carlo simulation of the continuum model consists of two basic moves[26, 46]: a single particle flip and a global flip. In the single particle flip, a particle is picked at random and reflected about the straight line joining its two neighbours (see Fig. 2.3(a)). The move is accepted using the standard Metropolis algorithm. Since the energy computation involves only nearby sites, the move is efficient and fast. In the global flip, two particles of the ring are chosen at random and the section of the ring between them is reflected about the line joining the two particles (see Fig. 2.3(b)). The energy calculation now involves

$O(N)$ particles and is thus computationally expensive. However, the global move is crucial to the study of the case where $J \neq 0$, since single particle moves alone are insufficient for equilibration in this case.

In the simulations, one Monte Carlo step is defined as one global move and N single particle moves made by selecting at random particles to be updated. This step is then repeated until the system equilibrates. This algorithm is ergodic within the initially chosen set of tangent vectors [26]. The initial configuration was chosen to be a regular N-sided polygon, but we verified that random configurations also gave the same results. Thermodynamic quantities are measured from averages taken over independent configurations in equilibrium.

We performed Monte Carlo simulations across a range of pressures for different values of J and system size. The system size varied from $N = 64$ to $N = 2000$. Typically each parameter value was run for 4×10^6 Monte Carlo steps. We waited typically for 10^6 steps for equilibration, averaging data over the remaining steps using independent configurations. We verified that changing the interval between two measurements did not change the results. In all the figures shown, the error bars on computed quantities are smaller than the sizes of the symbols used.

2.3.2 Exact enumeration

We first describe the algorithm for the case $J = 0$. Consider a random walk starting from the origin and taking steps in one of the four possible directions. For each step in the positive (negative) x-direction, we assign a weight e^{-Py} (e^{Py}), where y is the ordinate of the walker. Multiplying these weights, it is easy to check that the weight is e^{PA} for a closed walk enclosing an area A.

Let $T_N(x, y)$ be the weighted sum of all N-step walks from $(0, 0)$ to (x, y). It then obeys the recursion relation,

$$\begin{aligned} T_{N+1}(x,y) &= e^{-Py}T_N(x-1,y) + e^{Py}T_N(x+1,y) \\ &\quad + T_N(x,y-1) + T_N(x,y+1), \end{aligned} \tag{2.6}$$

with the initial condition

$$T_0(x, y) = \delta_{x,0}\delta_{y,0}. \tag{2.7}$$

Finally, $T_N(0, 0)$ gives the partition function of the ring polymer on a lattice.

For the semiflexible case, the recursion relation given above must be modified, since the ring is no longer a simple random walk but a walk with a one step memory. We convert it into a Markov process as follows. Let $T_N(x, y; x', y')$ be the sum of weights of all walks reaching (x, y) in N steps but having been at (x', y') at the previous step. These T_N's are now a Markov process and depend only on T_{N-1}'s. The recursion relations are then straightforward to write down. They are given by,

$$\begin{aligned}
T_{N+1}(x,y;x-1,y) &= e^{-Py}\big[T_N(x-1,y;x-2,y) + e^{2J}T_N(x-1,y;x,y) \\
&\quad + e^{J}T_N(x-1,y,x-1,y+1) + e^{J}T_N(x-1,y;x-1,y-1)\big], \\
T_{N+1}(x,y;x+1,y) &= e^{Py}\big[e^{2J}T_N(x+1,y;x,y) + T_N(x+1,y;x+2,y) \\
&\quad + e^{J}T_N(x+1,y;x+1,y+1) + e^{J}T_N(x+1,y;x+1,y-1)\big], \\
T_{N+1}(x,y;x,y-1) &= e^{J}T_N(x,y-1;x-1,y-1) + e^{J}T_N(x,y-1;x+1,y-1) \\
&\quad + e^{2J}T_N(x,y-1;x,y) + T_N(x,y-1;x,y-2), \\
T_{N+1}(x,y;x,y+1) &= e^{J}T_N(x,y+1;x-1,y+1) + e^{J}T_N(x,y+1;x+1,y+1) \\
&\quad + T_N(x,y+1;x,y+2) + e^{2J}T_N(x,y+1;x,y).
\end{aligned} \tag{2.8}$$

The partition function for the polymer problem can be expressed as a sum over areas and bends consistent with a given value of the area, i.e.,

$$\mathcal{Z}_N = T_N(0,0) = \sum_{A,B} C_N(A,B)e^{pA+JB}, \tag{2.9}$$

where $C_N(A, B)$ counts the number of closed paths of area A in a walk of length N which have B bends.

We count up to $N = 150$ for different values of J. The only limiting factor in going to larger N values is computer memory.

2.4 Flory-type Scaling Analysis

Flory type scaling theory provides a useful tool to capture the scaling behaviour of systems whose free energy reflects a competition between two or more terms. Such a scaling theory was proposed for the ISIR model in Ref. [21]. A transition from

a collapsed to an inflated state was predicted to occur at a critical value of the pressure, whose magnitude scaled with system size as N^{-1}. We show how these arguments may be extended to the semiflexible case, deriving expressions for the change in the critical point and scaling as a function of the bending rigidity.

The free energy consists of three terms describing (i) the entropy of the ring, (ii) the pressure differential and (iii) inextensibility of the bonds. When $J = 0$, these terms were argued to be R^2/N, $-PR^2$ and $R^4/(4N^3)$ for a ring of size R [21]. With semiflexibility, we show that a similar scaling form holds except for J dependent prefactors. Thus, the free energy takes the form

$$\begin{aligned} F &= F_{entropic} + F_{pressure} + F_{inextensibility}, \\ &\sim \frac{4\pi R^2}{N}\left[\alpha(J) - \hat{p}\right] + \frac{\beta(J)R^4}{N^3}. \end{aligned} \tag{2.10}$$

where we have defined $\hat{p} = Np/4\pi$, and α and β depend on J.

It is easily seen that a system described by such a Flory theory undergoes a continuous transition when the R^2/N term changes sign. This occurs at a critical scaled pressure $\hat{p}_c(J)$ which varies with J as

$$\frac{\hat{p}_c(J)}{\hat{p}_c(0)} = \frac{\alpha(J)}{\alpha(0)}. \tag{2.11}$$

When $\hat{p} < \hat{p}_c(J)$, then the area follows random walk statistics with $\langle A \rangle \sim N$. In this regime the R^4/N^3 term is not important. For non-zero values of J, there exists a persistence length l_p, and for length scales much larger than this length, the problem reduces to that of a freely jointed ring with an effective number of monomers given by N/l_p. Thus, we conclude that

$$\langle A(J, N, \hat{p}) \rangle = \frac{N}{\hat{p}_c(J)} f\left(\frac{\hat{p}}{\hat{p}_c(J)}\right), \quad \hat{p} < \hat{p}_c \tag{2.12}$$

where $f(x)$ is a scaling function. The scaling function $f(x)$ and $\hat{p}_c$ can be determined from the solution of the extensible chain with zero bending rigidity. This is discussed later in Sec. 2.4.3. This gives

$$\hat{p}_c = 4\pi\alpha(J), \tag{2.13}$$

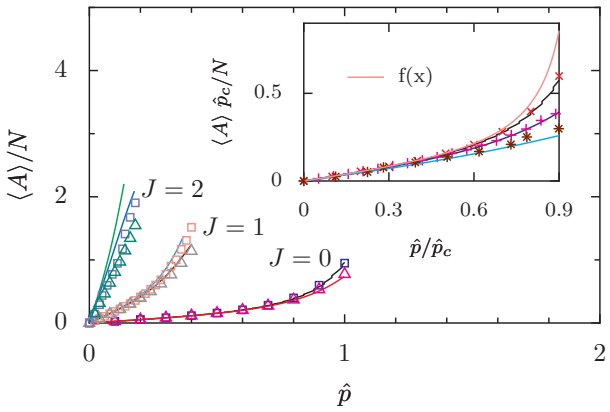

Figure 2.4: Area versus pressure curves for three J values for $\hat{p} < \hat{p}_c$. The points correspond to the continuum case while the solid curves correspond to the lattice case. The inset shows the collapse when the curves are scaled as in Eq. (2.12). The $f(x)$ curve in the inset represents the scaling function of Eq. (2.14). The main figure shows data for both $N = 60$ (triangles) and for $N = 100$ (squares), while the inset shows only the $N = 100$ data for clarity.

and

$$f(x) = \frac{1}{4\pi x} - \frac{\cot(\pi x)}{4}. \tag{2.14}$$

An equivalent approach to this transition is obtained by reinstating factors of the bond length a and $k_B T$ in the Flory estimate above. It is easy to see that the transition occurs when the "pressure length" $(\hat{p}a)^{-1}$, measuring the length scale at which the contribution of the pressure term in the free energy becomes significant, becomes of order the persistence length $l_p \sim Ja$.

Numerical confirmation of Eqs. (2.12) and (2.14) is provided in Fig. 2.4. The inset shows that the curves for different J collapse onto a single curve when scaled as in Eq. (2.12).

When $\hat{p} = \hat{p}_c$, the scaling is determined by the R^4/N^3 term. Thus, $\langle A \rangle \sim N^{3/2}/\sqrt{\beta(J)}$. Thus,

$$\frac{\langle A(J) \rangle}{\langle A(0) \rangle} = \sqrt{\frac{\beta(0)}{\beta(J)}}. \tag{2.15}$$

To test Eq. (2.15), we compare the Flory prediction with the enumeration results for the area in the lattice model. As can be seen from Fig. 2.5, there is good agreement for small values of J but the data starts to deviate away from the

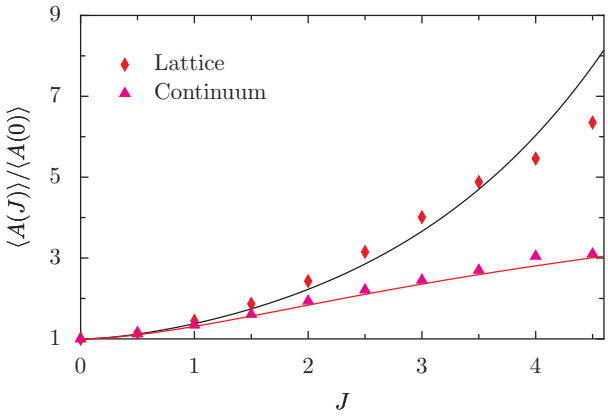

Figure 2.5: Comparison of the area ratio $\langle A(J)\rangle/\langle A(0)\rangle$ at the critical point with the scaling prediction (see Eqns. (2.15)) for the lattice (Eq. (2.32)) and continuum (Eq. (2.27)) models. The scaling prediction is satisfactory for small J but deviates as J increases. For the continuum simulation we used $N = 150$, while the points for the lattice calculation were obtained through a finite-size scaling of the values obtained from $N = 80, 90, ..., 150$.

predicted curve as J increases.

When $\hat{p} > \hat{p}_c(J)$, the ring is in an inflated state, with the area $\langle A\rangle \sim N^2$. To obtain an accurate description of this regime, we would need to keep higher order terms such as R^6/N^5 and so on. One thus expects that the lattice and the continuum problems should differ considerably in this regime.

We now derive expressions for $\alpha(J)$ and $\beta(J)$ in both the continuum and lattice cases. This is done by considering a semiflexible chain subjected to an external force. We obtain a perturbative solution for the partition function in the limit of small forces. From the partition function, we obtain the free energy of the ring. By comparing this with the form of Eq. (2.10), the values of $\alpha(J)$ and $\beta(J)$ can be obtained.

2.4.1 Continuum Case

Consider a semiflexible chain of N monomers. When the chain is pulled by a force $\vec{f}$, the partition function is given by

$$Z(J,\vec{f},N) = \int \prod_{j=1}^{N} d\hat{t}_j \; e^{J\hat{t}_j\cdot\hat{t}_{j+1}} \; e^{\vec{f}\cdot\hat{t}_j}. \tag{2.16}$$

We work in the limit of small forces, treating the J term exactly. We consider the f term as a perturbation on the zeroth order partition function [$f = 0$ in Eq. (2.16)], given by

$$Z_0(J,N) = [2\pi I_0(J)]^N, \tag{2.17}$$

where $I_0(J)$ is the modified Bessel function of the first kind of order 0.

Expanding the exponential in the force, we obtain,

$$\begin{aligned}
\exp\left(\sum_{j=1}^{N}\vec{f}.\hat{t}_j\right) &= \exp(\sum_{j=1}^{N} f\cos\theta_j) \\
&= 1 + f\sum_{j=1}^{N}\cos\theta_j + \frac{f^2}{2}\sum_{j,k=1}^{N}\cos\theta_j\cos\theta_k \\
&\quad + \frac{f^3}{6}\sum_{j,k,l=1}^{N}\cos\theta_j\cos\theta_k\cos\theta_l \\
&\quad + \frac{f^4}{24}\sum_{j,k,l,m=1}^{N}\cos\theta_j\cos\theta_k\cos\theta_l\cos\theta_m + \ldots
\end{aligned} \tag{2.18}$$

Now, the terms containing odd powers of $\cos\theta$ average to zero w.r.t. the zeroth order hamiltonian, and so we are left with

$$\begin{aligned}
\exp(\sum_{j=1}^{N}\vec{f}.\hat{u}_j) &\cong 1 + \frac{f^2}{2}\sum_{j,k=1}^{N}\cos\theta_j\cos\theta_k \\
&\quad + \frac{f^4}{24}\sum_{j,k,l,m=1}^{N}\cos\theta_j\cos\theta_k\cos\theta_l\cos\theta_m.
\end{aligned} \tag{2.19}$$

We now average each term with respect to the zeroth order Hamiltonian. On computing the averages, and expanding as a series for small values of f, the par-

tition function is obtained as

$$\ln Z(J,f,N) = \ln Z_0 + Nb_2 f^2 + Nb_4 f^4 + O(f^6), \tag{2.20}$$

where the coefficients b_2 and b_4 are given by

$$b_2 = \frac{I_0 + I_1}{4(I_0 - I_1)}, \tag{2.21}$$

$$b_4 = \frac{b_2^2}{4}\left[\frac{2I_2}{I_0 - I_2} - \frac{I_0 + 3I_1}{I_0 - I_1}\right]. \tag{2.22}$$

The I_n's are modified Bessel functions of the first kind. Their J dependence has been suppressed in the equation above.

The mean end-to-end distance in the limit of small force is obtained from $R \sim \partial \ln Z/\partial f$:

$$\frac{R}{N} = 2b_2 f + 4b_4 f^3 + O(f^5). \tag{2.23}$$

Solving for f from Eq. (2.23), we obtain

$$f = \frac{1}{2b_2}\frac{R}{N} - \frac{b_4}{4b_2^4}\left(\frac{R}{N}\right)^3 + O\left(\left(\frac{R}{N}\right)^5\right). \tag{2.24}$$

The Flory free energy $F(R) = -\ln Z + fR$, then reduces to

$$F(R) = -\ln Z_0 + \frac{1}{4b_2}\frac{R^2}{N} - \frac{b_4}{16b_2^4}\frac{R^4}{N^3} - pR^2. \tag{2.25}$$

Comparing with Eq. (2.10), the factors $\alpha(J)$ and $\beta(J)$ are obtained as

$$\alpha(J) = \frac{1}{4\pi}\frac{I_0 - I_1}{I_0 + I_1} \stackrel{J\to\infty}{\longrightarrow} \frac{1}{16\pi J}, \tag{2.26}$$

$$\beta(J) = 4\pi^2\alpha(J)^2\left[\frac{I_0 + 3I_1}{I_0 - I_1} - \frac{2I_2}{I_0 - I_2}\right] \stackrel{J\to\infty}{\longrightarrow} \frac{7}{64J}. \tag{2.27}$$

2.4.2 Lattice Case

For a lattice polygon, where each individual step can point only in four directions, we solve the problem of a semiflexible chain subject to an external force using the

exact 4×4 transfer matrix. The transfer matrix in this case is given by

$$T = \begin{pmatrix} e^{J+f} & e^{f/2} & e^{-J} & e^{f/2} \\ e^{f/2} & e^{J} & e^{-f/2} & e^{-J} \\ e^{-J} & e^{-f/2} & e^{J-f} & e^{-f/2} \\ e^{f/2} & e^{-J} & e^{-f/2} & e^{J} \end{pmatrix} \tag{2.28}$$

We determine the largest eigenvalue up to order f^4, and hence calculate the partition function:

$$\begin{aligned} \ln Z(J, f, N) &= N \left[\ln(2 + e^{-J} + e^{J}) + \frac{e^{J}}{4} f^2 \right. \\ &\quad \left. + \frac{1}{192}(e^{J} - 3e^{3J}) f^4 + O(f^6) \right]. \end{aligned} \tag{2.29}$$

We then follow the same procedure as for the continuum case, finding R/N in terms of f, inverting this equation to find f, and finally using this expression to compute the free energy. We thus obtain

$$F(R) = e^{-J} \frac{R^2}{N} + \left[\frac{1}{12} e^{-3J}(3e^{2J} - 1) \right] \frac{R^4}{N^3}. \tag{2.30}$$

The expressions for $\alpha(J)$ and $\beta(J)$ are then

$$\alpha(J) = \frac{1}{4\pi} e^{-J}, \tag{2.31}$$

$$\beta(J) = \frac{1}{12} e^{-3J}(3e^{2J} - 1). \tag{2.32}$$

2.4.3 Analytic answer for the collapsed phase

We shall now, for the sake of completeness, reproduce the exact result for the $J = 0$ case. It is known that the problem of self-intersecting polymers in two dimensions with no bending rigidity ($J = 0$) is analogous to the quantum mechanical problem of an electron moving in a magnetic field applied transverse to the plane of motion[12]. Using this analogy, analytic expressions for the partition function $\mathcal{Z}$ and $C_N(A)$, the number of closed walks of area A can be obtained.

First, recall that when an electron goes around a magnetic field, it picks up a

phase factor proportional to the flux enclosed by the path. This flux is proportional to the product of the strength of the magnetic field times the *algebraic area* enclosed by the loop. The propagator then is the sum over all such loops. This suggests that by a suitable mapping of the magnetic field to the pressure in the polymer problem, we can derive the partition function for the polymer from the quantum mechanical propagator for the electron problem.

Now, for an electron of charge e and mass m in a constant external magnetic field B, in the z direction, the kernel can be written as [12],

$$\begin{aligned} K(\vec{x},\vec{x'};t,0) &= \left(\frac{m}{2\pi i\hbar t}\right)\left(\frac{\omega t/2}{\sin\omega t/2}\right) \\ &\times \exp\left(\frac{im\omega}{2\hbar}\left\{\frac{\omega}{2}\cot\frac{\omega t}{2}[(x'-x)^2+(y'-y)^2]\ \omega(xy'-x'y)\right\}\right), \end{aligned} \tag{2.33}$$

where, $\omega = \frac{eB}{mc}$.
Since we are interested in the case when the electron returns to the origin, we have,

$$K(0,0;t,0) = \left(\frac{m}{2\pi i\hbar t}\right)\left(\frac{\omega t/2}{\sin\omega t/2}\right). \tag{2.34}$$

Now, in the quantum mechanical problem, when the particle goes around in a complete loop, it picks up a flux given by

$$\Phi = \frac{\imath eBA}{\hbar c}. \tag{2.35}$$

Thus to make the mapping to our problem, we need, $t \to -it$ to map the quantum mechanical Schrodinger equation to the classical diffusion equation, and

$$\frac{\imath eB}{\hbar c} = p \tag{2.36}$$

and

$$\omega = \frac{eB}{mc} = -\imath\frac{p\hbar}{m}. \tag{2.37}$$

Also, the time t in our case corresponds to the length of the polymer N.

The propagator is thus given by

$$K(0,0;-iN) = \frac{1}{4\pi}\frac{eB}{\hbar c}\frac{1}{\sinh \omega N/2}. \tag{2.38}$$

Substituting for ω, we obtain the partition function as

$$\mathcal{Z} = \frac{1}{4\pi}\frac{p}{\sin\frac{p\hbar N}{2m}}. \tag{2.39}$$

By comparing with the diffusion equation for a particle in two-dimensions, we see that $\frac{\hbar}{2m} = \frac{1}{4}$. Substituting this in the partition function and normalising appropriately, we finally obtain the partition function as

$$\mathcal{Z} = \frac{4^N}{4\pi}\frac{p}{\sin\frac{pN}{4}}. \tag{2.40}$$

To calculate the number of paths for a given area A, $C_N(A)$, we note that

$$\mathcal{Z} = \int_{-\infty}^{\infty} C_N(A)e^{pA} = \frac{1}{4\pi}\frac{p}{\sin\frac{p\hbar N}{2m}}. \tag{2.41}$$

Thus $C_N(A)$ is given by,

$$C_N(A) = \int_{-\infty}^{\infty}\frac{dk}{2\pi}\frac{4^{N-1}k}{\pi\sinh\left(\frac{kN}{4}\right)}e^{-\imath kA}. \tag{2.42}$$

On performing this integration we obtain,

$$C_N(A) = \frac{4^N}{N^2}\mathrm{sech}^2\frac{2\pi A}{N}. \tag{2.43}$$

On the lattice, since we actually measure $C_N(A)\Delta A$, we obtain,

$$C_N(A)\Delta A = \frac{4^{N+1}}{2N^2}\mathrm{sech}^2\frac{2\pi A}{N}. \tag{2.44}$$

This gives for the area

$$\langle A\rangle = \frac{1}{p} - \frac{N}{4}\cot(\frac{Np}{4}). \tag{2.45}$$

The free energy will have a singularity at $p = 4\pi/N$. Below this p, the ex-

pressions are valid for both the continuum case and the lattice. Exactly the same expression has been obtained by using the harmonic spring approximation [42]. The expression for area matches both the simulation and lattice data quite closely for low pressures, as can be seen from Fig. 2.4.

Moreover, if we recall the Flory prediction that by rescaling area and pressure by $\hat{p}_c(J)$, we can obtain the results for non-zero values of the bending rigidity from the answer of the problem with $J = 0$, we see that the above analysis also predicts the area expression for nonzero values of J.

2.5 Mean Field Theory

In this section we present mean-field theories to calculate the dependence of area on pressure and bending rigidity. In Sec. 2.5.1, we address the ISIR model ($J = 0$). The mean field theory presented in [21] performs poorly with respect to the Monte Carlo data when $\hat{p} > \hat{p}_c$. Here, we present an improved variational mean field which reproduces the behaviour of the area above the transition very accurately. It also yields the correct asymptotic behaviour for the area in the limit of high pressures. In this approach, the constraint of fixed link length in treated exactly while the closure constraint is satisfied in a mean field sense. However, such a mean-field theory fails to describe the collapsed phase, also yielding incorrect results for the case of nonzero J.

In Sec. 2.5.2, we generalise an earlier mean field theory for the freely jointed chain to include semi-flexibility, imposing the constraint of fixed bond length via a Lagrange multiplier [21]. The closure condition is imposed exactly. We thus derive expressions for the average area of the ring for all pressures and bending rigidity.

In Sec. 2.5.3, we present an alternate approach to variational mean field theories to that discussed in Sec. 2.5.1, obtained by computing averages with respect to a simple zeroth order hamiltonian. We also discuss different initial choices for the variational approach, and determine which of these match the simulation data best.

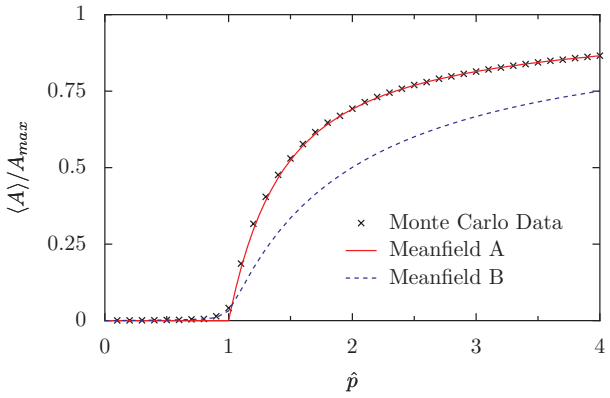

Figure 2.6: Comparison of Monte Carlo data with the two meanfield results for the flexible ($J = 0$) case, where meanfield A presents the results of the density-matrix approach and meanfield B that of the harmonic springs approach. The density matrix-based mean-field approach provides an accurate description of the area for $\hat{p} > \hat{p}_c$.

2.5.1 Density matrix mean-field for flexible polymers

In variational theory, a trial density matrix ρ is chosen to approximate the actual density matrix[10]. The variational parameters are determined by minimising the variational free energy F_ρ with respect to the parameters. The simplest mean-field theories assume a trial density matrix that is a product of independent single particle matrices, i.e,

$$\rho = \prod_j \rho_j, \tag{2.46}$$

where ρ_j is the single particle density matrix of particle j. The variational mean-field free energy is

$$F_\rho = \langle \mathcal{H} \rangle_\rho + T \sum_j Tr \rho_j \ln \rho_j. \tag{2.47}$$

The variational form for the density matrix should satisfy the constraint Tr $\rho_\mathrm{j} = 1$.

We choose the single particle density matrix based on the high pressure limit. In this limit, the ground state of our Hamiltonian is a regular N-gon, where the angle of the j^{th} tangent vector is $\theta_j = 2\pi j/N$. The single particle density matrix has a delta function peak at this value. At intermediate pressures, we therefore

take the form of the density matrix to be a gaussian of width σ (the variational parameter) centred about $2\pi j/N$:

$$\rho_j(\theta_j) = \frac{1}{\sqrt{2\pi}\sigma\,\mathrm{erf}[\pi/\sqrt{2}\sigma]} \exp\left[\frac{-(\theta_j - \frac{2\pi j}{N})^2}{2\sigma^2}\right], \tag{2.48}$$

where the normalisation ensures that Tr $\rho_{\mathrm{j}} = 1$ and $\mathrm{erf}(x)$ is the error function defined as

$$\mathrm{erf}(x) = \frac{2}{\sqrt{\pi}} \int_0^x e^{-t^2}\, dt. \tag{2.49}$$

Using this form of the density matrix, the averages are obtained as,

$$\begin{aligned}
\langle \cos\theta_j \rangle &= K(\sigma) \cos(\frac{2\pi j}{N}, \\
\langle \sin\theta_j \rangle &= K(\sigma) \sin(\frac{2\pi j}{N}, \\
\langle \rho_j \ln \rho_j \rangle &= -\frac{1}{2} + \frac{e^{\frac{\pi^2}{2\sigma^2}}\sqrt{\frac{\pi}{2}}}{\sigma\,\mathrm{erf}(\frac{\pi}{\sqrt{2}\sigma})} + \ln[\frac{1}{\sqrt{2\pi}\sigma\,\mathrm{erf}(\frac{\pi}{\sqrt{2}\sigma})}],
\end{aligned} \tag{2.50}$$

where

$$K(\sigma) = \frac{e^{-\sigma^2/2}\big[\,\mathrm{erf}[(\pi - \imath\sigma^2)/\sqrt{2}\sigma] + \mathrm{erf}[(\pi + \imath\sigma^2)/\sqrt{2}\sigma]\big]}{2\,\mathrm{erf}[\pi/\sqrt{2}\sigma]}. \tag{2.51}$$

The variational free energy is then given by,

$$\begin{aligned}
\frac{F_\rho}{N} = &-\frac{p}{4}\cot\left(\frac{\pi}{N}\right) K(\sigma)^2 + J\cos\left(\frac{2\pi}{N}\right) K(\sigma)^2 \\
&-\frac{1}{2} + \frac{\sqrt{\pi}\exp(\pi^2/(2\sigma^2))}{\sqrt{2}\sigma\,\mathrm{erf}[\pi/\sqrt{2}\sigma]} - \ln\left(\sqrt{2\pi}\sigma\,\mathrm{erf}[\frac{\pi}{\sqrt{2}\sigma}]\right),
\end{aligned} \tag{2.52}$$

where we have used the identity,

$$\sum_{j=0}^{N-1}\sum_{k=0}^{j-1} \sin\left[\frac{2\pi}{N}(j-k)\right] = \frac{N}{2}\cot(\frac{\pi}{N}). \tag{2.53}$$

When $N \gg 1$, the pressure and bending terms in Eq. (2.52) can be combined, and the problem is equivalent to one of a flexible polymer ($J = 0$) with an effective pressure $\hat{p}_{\mathrm{eff}} = \hat{p} + J$.

The variational parameter σ is chosen to be the σ^* that minimises F_ρ in

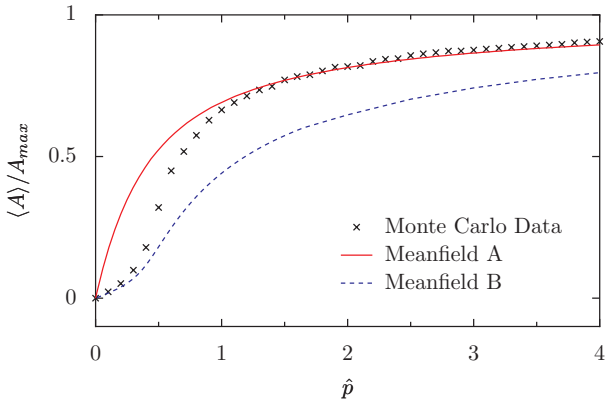

Figure 2.7: Comparison of Monte Carlo data with the two mean-field approaches for the case $J = 1$.

Eq. (2.52). This is done numerically. The average area, equal to $-\partial F_\rho / \partial p$, is then given by

$$\langle A \rangle = \frac{N}{4} \cot\left(\frac{\pi}{N}\right) K^2(\sigma^*) \overset{N\to\infty}{\longrightarrow} \frac{N^2}{4\pi} K^2(\sigma^*). \tag{2.54}$$

We now derive the asymptotic behaviour of area in the limit of high pressures. We work in the limit when N is large. For large pressures, we expect that σ^* tends to zero. In this limit

$$K(\sigma) \approx e^{-\sigma^2/2}, \quad \sigma \to 0. \tag{2.55}$$

and the variational free energy is then given by

$$F_\rho(\sigma) = N\left[-(\hat{p} + J)e^{-\sigma^2} - \ln(\sqrt{2\pi}\sigma) - \frac{1}{2}\right], \tag{2.56}$$

where $\hat{p} = Np/(4\pi)$. Solving $dF_\rho/d\sigma^* = 0$, it is straightforward to obtain

$$\sigma^* = \frac{1}{\sqrt{2\hat{p}}} + \frac{1 - 2J}{4\sqrt{2}\hat{p}^{3/2}}, \quad \hat{p} \to \infty. \tag{2.57}$$

The area then reduces to

$$\frac{\langle A \rangle}{N^2/4\pi} \to 1 - \frac{1}{2\hat{p}} + \frac{4J - 1}{8\hat{p}^2}, \quad \hat{p} \to \infty. \tag{2.58}$$

For flexible polymers ($J = 0$), this mean-field theory reproduces the $\hat{p} > \hat{p}_c$ behaviour very accurately. It also obtains the correct asymptotic behaviour. In Fig. 2.6, we compare the Monte Carlo data for $J = 0$ with the results of the above mean field theory and contrast it with the meanfield theory of Ref. [21].

The density matrix mean-field however, fails to correctly obtain the behaviour for non-zero values of the bending rigidity. It predicts a first order transition for $J \geq 1$, in disagreement with results from scaling theory. We compare the results of this mean field with the Monte Carlo data in Fig. 2.7 for a system with $J = 1$. This mean-field approach then predicts a transition at $\hat{p} = 0$. The discrepancy between the two curves increases for larger values of J.

We now describe an alternative mean-field approach to this problem which extends the harmonic spring-based mean field theory of Ref. [21] to non-zero values of J.

2.5.2 Harmonic spring mean-field for semiflexible polymers

We follow the approach of Ref. [18] wherein the rigid links between particles are replaced by extensible springs. The spring constant λ of the springs is identified with a Lagrange multiplier, chosen so that the mean length of a spring equals unity [21].

Consider a partition function for N particles given by,

$$\mathcal{Z} = \int d\vec{t}_j \exp\left[\frac{p}{2}\sum_{k<j}\vec{t}_k \times \vec{t}_j + J\sum_j \hat{t}_j \cdot \hat{t}_{j+1} - \lambda\sum_j \vec{t}_j^2\right]. \tag{2.59}$$

Note that while pressure couples to $\vec{t}$, the bending rigidity couples to the unit vectors $\hat{t}$. We make the approximation of replacing $\hat{t}$ by $\vec{t}$. This makes the problem analytically tractable.

Expanding the tangent vectors in Fourier space as,

$$\begin{aligned} \hat{t}_j^x &= \sqrt{\frac{2}{N}}\sum_k [A_k \cos(jk) + B_k \sin(jk)], \\ \hat{t}_j^y &= \sqrt{\frac{2}{N}}\sum_k [A_k' \cos(jk) + B_k' \sin(jk)], \end{aligned} \tag{2.60}$$

where $k = 2\pi l/N$, $l = 1, 2, \cdots, N$. The partition function then reduces to

$$\mathcal{Z} = \prod_k \int dA_k dA_k' dB_k dB_k' \; e^{-(\lambda - J\cos k)(A_k^2 + B_k^2 + A_k'^2 + B_k'^2)} e^{\frac{p}{k}(B_k A_k' - A_k B_k')}. \tag{2.61}$$

By completing the squares, this integral can be written as a gaussian integral and hence can be calculated exactly. This gives

$$\mathcal{Z} = \prod_k \frac{1}{\lambda - J\cos k} \times \left[1 - \frac{p^2}{4k^2(\lambda - J\cos k)^2}\right]^2. \tag{2.62}$$

The parameter λ^* is determined by equating the mean square link length to one, i.e

$$-\frac{1}{N}\frac{\partial \ln \mathcal{Z}}{\partial \lambda} = 1. \tag{2.63}$$

This gives

$$N = \sum_{l=1}^{N} \frac{1}{\lambda^* - J\cos(\frac{2\pi l}{N})} \left[1 + \frac{2\hat{p}^2}{l^2[\lambda^* - J\cos(\frac{2\pi l}{N})]^2 - \hat{p}^2}\right], \tag{2.64}$$

where $\hat{p} = pN/4\pi$.

When $J = 0$, the first factor in Eq. (2.64) becomes independent of l, and then the resultant expression can be evaluated exactly. Hence, an analytic expression for λ^* can be obtained in this case [21]. For $J \neq 0$, this is no longer possible, and for finite system sizes the resultant equation must be solved numerically. When $N \gg 1$, it is still possible to extract the behaviour of the system analytically.

We now determine the phase boundary from Eq. (2.64). We will consider the limit $N \gg 1$. First, note that $\lambda^* - J\cos(2\pi l/N) \neq 0$ for all l. For positive λ^*, this gives the condition that $\lambda^* > J$. Second, consider the term in the denominator for $l = 1$. It is $(\lambda^* - J)^2 - \hat{p}^2$. If we assume that λ^* is continuous in $\hat{p}$, we have the second constraint that $\lambda^* > J + \hat{p}$.

Setting $x = \frac{l}{N}$ and converting the first sum in Eq. (2.64) to an integral, the

equation for λ^* reduces to

$$1 = \frac{1}{\sqrt{\lambda^{*2} - J^2}} - \frac{1}{N(\lambda^* - J)} + \frac{2}{N(\lambda^* - J)} \sum_{k=1}^{\infty} \left(\frac{\hat{p}}{\lambda^* - J} \right)^{2k} \frac{1}{2k-1} + \mathcal{O}(\frac{1}{N^2}). \tag{2.65}$$

The sum in Eq. (2.65) is convergent if the ratio $\hat{p}/(\lambda^* - J) < 1$. In this case, we keep only the first term on the right hand side of Eq. (2.65). This gives,

$$\lambda^* = \sqrt{1 + J^2}, \quad \text{for } \hat{p} < \hat{p}_c. \tag{2.66}$$

The critical pressure is obtained when the ratio $\hat{p}/(\lambda^* - J)$ becomes equal to 1, i.e.

$$\hat{p}_c(J) = \lambda^* - J = \sqrt{1 + J^2} - J. \tag{2.67}$$

For large values of J, this goes as $\hat{p}_c(J) \sim 1/2J$, which differs by a factor of 2 from the answer obtained by scaling arguments [see Eq. (2.26)].

We shall now estimate λ^* in the different scaling regimes. We assume that λ^* is a non-decreasing function of $\hat{p}$ (as in $J = 0$). Then, since we have the constraint of $\lambda^* > \hat{p} + J$, the ratio $\hat{p}/(\lambda^* - J)$ must continue to remain at 1 for $\hat{p} > \hat{p}_c$. Thus, above the critical point, we obtain

$$\lambda^* = \hat{p} + J, \quad \text{for } \hat{p} > \hat{p}_c. \tag{2.68}$$

However, a simple substitution of Eq. (2.68) in Eq. (2.64) for $\hat{p} > \hat{p}_c$ does not satisfy Eq. (2.64). We therefore need to calculate the correction term arising from large but finite N. We start by considering Eq. (2.64). The first term can be summed exactly, giving

$$N \left(1 - \frac{1}{\sqrt{\lambda^2 - J^2}} \right) = \sum_{l=1}^{N} \frac{1}{\lambda - J\cos(\frac{2\pi l}{N})} \frac{2\hat{p}^2}{l^2(\lambda - J\cos(\frac{2\pi l}{N}))^2 - \hat{p}^2}. \tag{2.69}$$

We calculate the finite size corrections to λ^* as follows. Let

$$\lambda^*_{\hat{p}\geq\hat{p}_c} = \hat{p} + J - \delta. \tag{2.70}$$

When $\delta \to 0$, the main contribution to the left hand side of Eq. (2.69) comes from the $l = 1$ term. The contribution from other l is convergent as $\delta \to 0$. Expanding the right hand side as a series in δ, we obtain

$$-\frac{1}{\delta} = N\left[1 - \frac{1}{\sqrt{\hat{p}^2 + 2\hat{p}J}} - \frac{\delta(\hat{p}+J)}{(\hat{p}^2+2\hat{p}J)^{3/2}}\right]. \tag{2.71}$$

The δ independent term in the right hand side of Eq. (2.71) is nonzero for $\hat{p} > \hat{p}_c$ and is equal to zero for $\hat{p} = \hat{p}_c$. Thus, when $\hat{p} > \hat{p}_c$, we keep only the first term in the right side, while at $\hat{p} = \hat{p}_c$, we need to keep the second term too. Solving for δ, we obtain,

$$\delta = \begin{cases} \frac{1}{\sqrt{N}}\frac{1}{(1+J^2)^{1/4}}, & \hat{p} = \hat{p}_c, \\ \frac{1}{N}\frac{\sqrt{\hat{p}^2+2\hat{p}J}}{\sqrt{\hat{p}^2+2\hat{p}J}-1}, & \hat{p} > \hat{p}_c. \end{cases} \tag{2.72}$$

We are now in a position to calculate the mean area $\langle A\rangle$ from $\frac{\partial \ln \mathcal{Z}}{\partial p}$. This gives,

$$\langle A\rangle = \frac{N\hat{p}}{2\pi}\sum_{l=1}^{N}\frac{1}{l^2(\lambda^* - J\cos(\frac{2\pi l}{N}))^2 - \hat{p}^2}. \tag{2.73}$$

The numerical values obtained for λ are then substituted in this equation to get the corresponding value of the area. We can, however, analytically determine the scaling behaviour of the area in the limit of large system sizes from the values of λ calculated above.

For $\hat{p} < \hat{p}_c$, we have,

$$\langle A\rangle \simeq \frac{N\hat{p}}{2\pi}\sum_{l=1}^{N}\frac{1}{l^2(\sqrt{1+J^2} - J\cos(2\pi l/N))^2 - \hat{p}^2} \tag{2.74}$$

At the critical point, we obtain, from Eqns. (2.71) and (2.73),

$$\langle A\rangle = N^{3/2}\frac{(1+J^2)^{1/4}}{4\pi}, \quad \hat{p} = \hat{p}_c. \tag{2.75}$$

Similarly, for pressures greater than the critical pressure, we obtain, from Eqns. (2.68) and (2.73),

$$\frac{\langle A\rangle}{N^2/4\pi} = 1 - \frac{1}{\sqrt{\hat{p}^2 + 2\hat{p}J}} \stackrel{\hat{p}\to\infty}{\longrightarrow} 1 - \frac{1}{\hat{p}} + \frac{J}{2\hat{p}^2},\ \hat{p} > \hat{p}_c. \tag{2.76}$$

This mean field theory reproduces the qualitative behaviour of the simulation data correctly. It predicts a continuous transition for all J, unlike the density matrix field theory. However, there is a quantitative disagreement with the data. This can be seen by comparing the results of this mean-field theory with the simulation data in both the flexible (Fig. 2.6) and semi-flexible (Fig. 2.7) polymer cases.

2.5.3 Other variational approaches

An equivalent approach to variational mean field theory other than the density matrix formulation presented in Sec. 2.5.1 is the Hamiltonian approach, in which the averages of the full Hamiltonian $\mathcal{H}$ are computed with respect to some simpler zeroth level Hamiltonian $\mathcal{H}_0$ which can be evaluated exactly. It can be shown [10] that the true free energy F is always less than or equal to a variational free energy defined as

$$F_v[h] = F_0 + \langle \mathcal{H} - \mathcal{H}_0\rangle_0, \tag{2.77}$$

where F_0 is the free energy corresponding to the zeroth level hamiltonian and h is the set of parameters which characterises the zeroth order hamiltonian $\mathcal{H}_0$. The values of the parameters are then to be determined by minimising the free energy with respect to these parameters.

The hamiltonian for our system is given by

$$\begin{aligned}\mathcal{H} &= -\frac{p}{2}\sum_{j=0}^{N-1}\sum_{k=0}^{j-1}(\hat{t}_k \times \hat{t}_j) - J\sum_{j=0}^{N-1}(\hat{t}_j.\hat{t}_{j+1}) \\ &= -\frac{p}{2}\sum_{j=0}^{N-1}\sum_{k=0}^{j-1}\sin(\theta_j - \theta_k) - J\sum_{j=0}^{N-1}\cos(\theta_{j+1} - \theta_j)\end{aligned}$$

It was observed that the results of the density matrix approach can be exactly

reproduced by choosing a zeroth order hamiltonian as

$$\mathcal{H}_0 = -h \sum_{j=0}^{N-1} \cos(\theta_j - \frac{2\pi j}{N}), \tag{2.78}$$

where h is an unknown variational parameter denoting the magnitude of the external field. This observation also makes sense physically since it is clear from the form of the zeroth order hamiltonian that this ansatz ensures that the individual angles θ_j are directed along $2\pi j/N$, which is also the main input of the density functional mean field theory as described in Sec. 2.5.1.

The variational free energy in this case is given by

$$F_v = -N\ln(2\pi) - N\ln(I_0(h)) - \frac{pN}{4}\frac{I_1^2(h)}{I_0^2(h)}\cot(\frac{\pi}{N}) - NJ\frac{I_1^2(h)}{I_0^2(h)}\cos(\frac{2\pi}{N}) + Nh\frac{I_1(h)}{I_0(h)}. \tag{2.79}$$

The value of the variational parameter h is to be determined by solving the equation

$$\frac{\partial \mathcal{F}_v[h]}{\partial h} = 0, \tag{2.80}$$

and ensuring that the solution satisfies

$$\frac{\partial^2 \mathcal{F}_v[h]}{\partial^2 h} \geq 0. \tag{2.81}$$

It is clear from the form of the variational free energy Eq. 2.79 that for $N \gg 1$, the pressure and bending rigidity can be combined into an effective pressure $\hat{p}_{eff} = \hat{p} + J$, which was the case for the density matrix approach also, as was seen from Eq. 2.52.

We also tried different choices for the zeroth order hamiltonian in order to see whether the result might be improved. However, it was found that, among the various choices that we used for the zeroth order hamiltonian $\mathcal{H}_0$, the best results we obtained by our original choice, where the individual angles of the tangent vectors are constrained to point along specific direction, as described in Eq. 2.78.

One obvious choice for the zeroth order order hamiltonian might seem to be to constrain the difference in angles between adjacent tangent vectors, instead of constraining the angles of the individual tangent vectors. We assume that the

angles between adjacent tangent vectors to have a value of $2\pi/N$. The zeroth order hamiltonian in this case can be written as

$$\mathcal{H}_0 = -h \sum_{j=1}^{N-1} \cos\big[(\theta_{j+1} - \theta_j) - \frac{2\pi}{N}\big]. \tag{2.82}$$

Using this choice for the zeroth order hamiltonian, the variational free energy is obtained as

$$\begin{aligned} F_v &= (N-1)\ln[I_0(h)] - \frac{pN}{2}\frac{I_0^2(h)I_1(h)\sin(2\pi/N)}{I_0^2(h) - 2I_0(h)I_1(h)\cos(2\pi/N) + I_1^2(h)} \\ &- NJ\frac{I_1(h)}{I_0(h)}\cos(\frac{2\pi}{N}) + Nh\frac{I_1(h)}{I_0(h)}. \end{aligned} \tag{2.83}$$

As is immediately clear from the form of the variational free energy, the pressure and bending rigidity terms cannot be combined in the limit of large N, as was done for Eq. 2.52 and Eq. 2.79. Thus, this variational approach cannot yield the correct asymptotic result.

Another ansatz tried out was to define the zeroth order hamiltonian as the sum of cross products of nearest neighbour tangent vectors. This is then given by

$$\mathcal{H}_0 = -h \sum_{j=1}^{N-1} \sin(\theta_{j+1} - \theta_j). \tag{2.84}$$

However, the variational free energy computed with respect to this hamiltonian did not succeed in explaining the observed variation of the average area as a function of the pressure. Thus, within the range of choices that we tried for the variational approach, the best results were obtained in the case when the individual tangent vectors were constrained to lie, on average, along specified directions, as described in this section as well as Sec. 2.5.1.

2.6 Scaling and Critical Exponents

The order parameter that describes the collapsed to inflated phase transition is the ratio of the area to the maximum area. When $N \gg 1$, the ratio is zero below the transition and non-zero above it. The behaviour near the transition line can

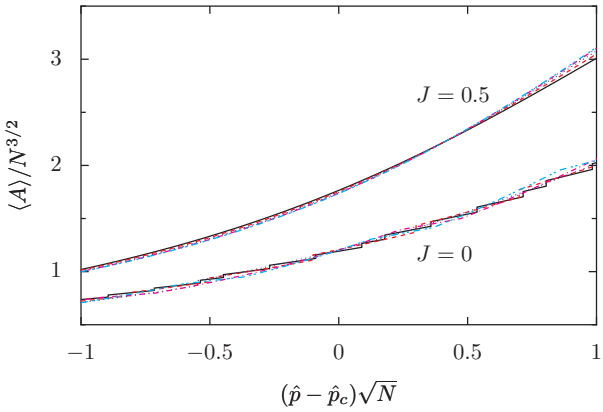

Figure 2.8: Area collapse for flexible and semiflexible polymers around the critical point. This verifies Eq. (2.85). The data is for $N = 80, 100, 120, 140, 150$ for the lattice problem.

be described by the scaling form

$$\frac{\langle A\rangle}{A_{max}} \simeq N^{-\phi\beta} g\left[(\hat{p} - \hat{p}_c)N^{\phi}\right], \tag{2.85}$$

where ϕ, β are exponents and $g(x)$ is a scaling function. When $x \to 0$, then $g(x) \to$ constant. When $x \to \infty$, then $g(x) \sim x^{\beta}$. When $x \to -\infty$, then $g(x) \sim 1/x$ [see Eqs. (2.12) and (2.14)]. This immediately implies that

$$\phi(1 + \beta) = 1. \tag{2.86}$$

To obtain the one independent exponent, we resort to the scaling theory (see Sec. 2.4). At $\hat{p}_c$, $\langle A\rangle/A_{\max} \sim 1/\sqrt{N}$. At the critical point, the area scales as $N^{3/2}$. Combining with Eq. (2.86), we obtain $\phi = 1/2$ and $\beta = 1$. These exponents are independent of J.

In Fig. 2.8, we show scaling plots when area is scaled as in Eq. (2.85) with ϕ and β as above for the cases $J = 0$ and $J = 0.5$. The excellent collapse shows that the Flory type scaling theory gives the correct exponents.

We now look at the fluctuations. Consider the compressibility χ defined as

$$\chi = \frac{1}{A}\frac{\partial\langle A\rangle}{\partial p}. \tag{2.87}$$

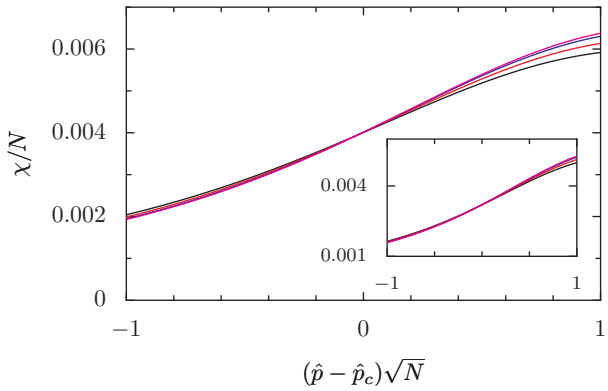

Figure 2.9: The scaling plots for compressibility χ when scaled as in Eq. (2.89). The data is for the lattice model with $J = 0.5$ and $J = 0$ (inset). The system sizes are $N = 80, 100, 120, 140, 150$.

When $\hat{p} < \hat{p}_c$, χ can be calculated from Eqs. (2.12) and (2.14) to be

$$\chi = -\frac{1}{\hat{p}^2} + \frac{\pi^2}{\hat{p}_c^2 \sin^2(\pi\hat{p}/\hat{p}_c)}, \quad \hat{p} < \hat{p}_c. \tag{2.88}$$

Thus, χ diverges as $(\hat{p}_c - \hat{p})^{-2}$ below the transition point. The behaviour near the transition point is described by the scaling form

$$\chi \simeq N^{\phi\gamma} h\left[(\hat{p} - \hat{p}_c)N^{\phi}\right], \tag{2.89}$$

where $h(x)$ is a scaling function and $\phi = 1/2$. When $x \to 0$, then $h(x) \to$ constant. When $|x| \gg 1$, then $h(x) \sim x^{-\gamma}$. Comparison with Eq. (2.88) gives $\gamma = 2$.

In Fig. 2.9, we plot the compressibility scaled as in Eq. (2.89) for two different values of J. A good collapse is obtained again showing that the Flory type scaling theory gives the correct exponents. Similar, but noisier data can be obtained for the continuum model. We thus conclude that the introduction of semiflexibility does not affect any of the exponents describing the transition.

2.7 The lattice problem

In this section, we present some additional enumeration results for the lattice problem. Consider the scaling theory presented in Sec. 2.4. The inextensibility of

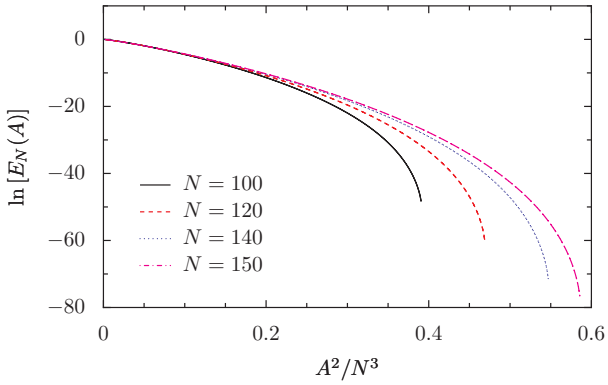

Figure 2.10: Collapse of the $E_N(A)$ for different values of N when plotted against A^2/N^3. The data is for the lattice model with $J = 0$.

the polymer was captured by the R^4/N^3 term for a polymer of extent R. This was obtained from a calculation based on the extension of a polymer under a force. Here we present numerical evidence supporting this.

Let $P_N(A)$ be the probability (at $P = 0$) that a walk of length N encloses an area A. In Appendix 2.4.3, we obtain [see Eq. (2.44)]

$$P_N(A) = \frac{1}{N} I\left(\frac{A}{N}\right), \; A, N \to \infty, \; \frac{A}{N} \text{ fixed.} \tag{2.90}$$

where the scaling function $I(x)$ is given by

$$I(x) = \pi \, \mathrm{sech}^2(2\pi x). \tag{2.91}$$

We consider the corrections to the scaling form in Eq. (2.90). Let

$$E_N(A) = \frac{N P_N(A)}{I(A/N)}. \tag{2.92}$$

Scaling theory predicts that $E_N(A)$ should be a function of one variable A^2/N^3. This is verified in Fig. 2.10 where $\ln E_N(A)$ is plotted against A^2/N^3 for a range of system sizes.

We also study the behaviour of area when $\hat{p}$ is very large. When $\hat{p} \gg 1$, the behaviour is seen to differ from the continuum version of the problem. It can be

shown to be[32]

$$1 - \frac{\langle A \rangle}{A_{\max}} \sim \frac{1}{\hat{p}^2}, \quad \hat{p} \to \infty. \tag{2.93}$$

This should be contrasted with the continuum case which varied as $1/\hat{p}$. In Fig. 2.11, we show numerical confirmation of the prediction of Eq. (2.93).

2.8 Conclusions

In this chapter, we have proposed and studied lattice and continuum models for self-intersecting pressurised semi-flexible polymers. Our work generalises results of Ref. [21] to include a bending rigidity. A simple variational mean-field approach provides very accurate fits to the Monte Carlo data for this problem in the absence of semi-flexibility. The mean-field approach for $J = 0$ [42, 18, 21] was generalised to the semiflexible case. The phase boundary between collapsed and inflated phases as well as expressions for the area as a function of p and J in the different phases were obtained analytically.

We have shown that the essence of the physics is captured through simple Flory approximations. The scaling predictions of the Flory theory were verified numerically for both the lattice and continuum cases.

We have also investigated the behaviour of the system in the extreme limits of a fully pressurised polymer ring and a collapsed configuration. For the fully

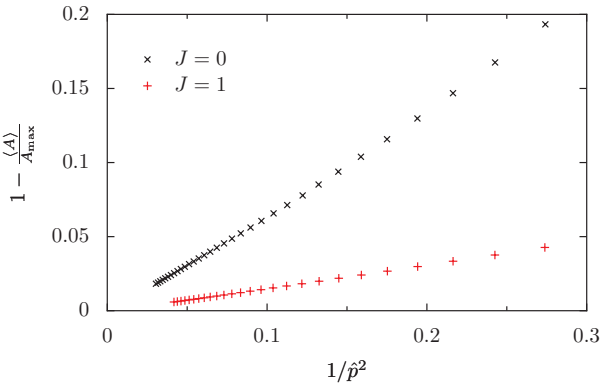

Figure 2.11: The asymptotic behaviour of area in the limit of large $\hat{p}$ as computed for the lattice model. The curves are straight lines when plotted against $1/\hat{p}^2$.

pressurised ring, we deduce the leading order asymptotic behaviour of the area in both the continuum and lattice cases. The collapsed phase was studied using the mapping to the quantum mechanical problem of an electron confined to two dimensions and placed in a transverse magnetic field[12]. The analytic results thus obtained fit the data accurately.

The usefulness of these results for more realistic systems lies in the fact that both the restriction to the signed area as well as allowing for self-intersections at no energy cost are irrelevant in the large p limit. The results obtained at large p should therefore apply both qualitatively and quantitatively to the more realistic case of a pressurised self-avoiding polymer, where the pressure term couples to the true physical area and not to the signed area. This is the LSF model [27]. The approach presented here is thus also useful in understanding the behaviour of a larger class of models, some of which are more physical in character, but which lack the analytic tractability of the model proposed and studied here.

3

Asymptotic behaviour of pressurized lattice polygons

3.1 Introduction

The study of lattice polygons weighted by area and perimeter is a central problem in lattice statistics and combinatorics. Lattice polygons have been used to model vesicles [27, 15], cell membranes [43], emulsions [44], polymers [36] and percolation clusters [37]. In several cases, exact generating functions for classes of such polygons have been obtained. In the introduction (Sec. 1.4) we provided an overview of lattice polygons and the previous work done in this field. Also, a survey of different kinds of lattice polygons and a review of related results can be found in Refs. [5, 45].

In this chapter, we study the asymptotic behaviour of the area enclosed by inflated polygons of fixed perimeter. We calculate the area for two special cases of lattice polygons - convex and column-convex lattice polygons. We then conjecture the appropriate form for the area of self-avoiding polygons in the inflated phase.

We first summarise known results for the problem of pressurised polygons, based on the generating function

$$G(\mu, p) = \sum_{A,N} C_N(A) e^{pA} \mu^N, \tag{3.1}$$

where $C_N(A)$ is the number of self-avoiding polygons of perimeter N and area A, weighted by a chemical potential μ. Here p is the pressure which couples to

the area A. Exact solutions exist for $G(\mu, p)$ when $C_N(A)$ is restricted to convex polygons [29, 4, 3] or to column-convex polygons [6]. However, a general solution for self-avoiding polygons is unavailable. Exact enumeration results for self-avoiding polygons exist for all N up to $N = 90$ and for all A for these values of N [25]. A transition at $p = 0$ separates a branched polymer phase when $p < 0$ (for μ sufficiently small) from an inflated phase when $p > 0$. At $p = 0$, the problem reduces to that of the enumeration of self-avoiding polygons. The scaling function describing the scaling behaviour (for $p < 0$) near the tricritical point $p = 0$ and $\mu = \kappa^{-1}$, where κ is the growth constant for self-avoiding polygons, is also known exactly [39, 9, 38].

Less is known about the inflated phase obtained for positive pressures $p > 0$. However, this phase is of physical interest in the case of two-dimensional vesicles, or equivalently pressurised ring polymers [27, 42, 18, 21, 32]. In the calculations described in this chapter, we consider the partition function

$$\mathcal{Z}_N(p, J) = \sum_{A,b} C_N(A, b) e^{pA - Jb}, \quad p > 0, \tag{3.2}$$

where $C_N(A, b)$ is the number of self-avoiding polygons of area A with b bends. A bending energy cost J per bend is introduced to incorporate semi-flexibility.

Some rigorous results exist for $Z_N(p, 0)$ when $p > 0$. Ref. [35] proved that

$$\mathcal{Z}_N(p, 0) = A(p) e^{pN^2/16} (1 + \mathcal{O}(\rho^N)) \ \text{ as } \ N \to \infty, \tag{3.3}$$

for some $0 < \rho < 1$, with $A(p)$ some function of p. This result holds in the limit where $N \to \infty$ keeping p fixed. However, as we argue in Sec. 3.2, the relevant scaling limit in the inflated regime is $p \to 0$, $N \to \infty$ keeping $\tilde{p} = pN$ finite.

The central results of the chapter are the following: We calculate expressions for the area for convex [see Eq. (3.28)] and column-convex [see Eqs. (3.48), (3.52) and (3.54)] polygons. In the limit $\tilde{p} \gg 1$, we show that for both convex and column-convex polygons, the area is given by,

$$\langle A \rangle = \frac{N^2}{16} \left[1 - \frac{32\pi^2}{3\tilde{p}^2} + \frac{64}{\tilde{p}^2} \mathrm{Li}_2 \left(1 - \alpha\right) \right] + \mathcal{O}(e^{-\tilde{p}/8}), \tag{3.4}$$

where Li_2 is the dilogarithm function

$$\mathrm{Li}_2(x) = \sum_{m=1}^{\infty} \frac{x^m}{m^2}, \tag{3.5}$$

and, $\alpha = e^{-2J}$. We argue that this result should also extend to the self-avoiding case and test this conjecture numerically.

The chapter is organised as follows. In Sec. 3.2, we present a justification of the scaling limit we consider using a simply Flory-type argument. Sections. 3.3 and 3.4 contain the calculation of the area for convex and column-convex polygons respectively. Section 3.5 contains the numerical analysis of self-avoiding polygons and self intersecting polygons. A brief summary of our results and conclusions is presented in Sec. 3.6.

3.2 Scaling in the inflated regime

The inflated regime of self-intersecting pressurised polygons has been well studied in the continuum [42, 18, 21, 32]. In this case the appropriate scaling variable is obtained by scaling the thermodynamic pressure with the system size, taking $p \to 0$, $N \to \infty$ keeping $\tilde{p} = pN$ finite. A typical configuration in the inflated phase has no self-intersections. Thus, we expect that the above scaling should also hold for self-avoiding polygons.

This choice of the scaling variable can be motivated by simple scaling arguments. The pressure contribution to the free energy in the inflated phase is given by

$$F = -pA \approx -pR^2 \approx -pN^2, \tag{3.6}$$

since $\langle R \rangle \sim N$ in this regime. However, the free energy of a polygon of perimeter N, being an extensive variable, scales linearly with N. In order to make these two energies comparable, the pressure should scale inversely with N, i.e. $p \sim 1/N$.

In Fig. 3.1, we show the variation of $\langle A \rangle / A_{max}$ with pressure p, where $A_{max} = N^2/16$ is the maximum possible area. The data points collapse onto one curve when p is scaled as $\tilde{p} = pN$. The data is obtained from exact enumerations of self-avoiding polygons on the square lattice [24].

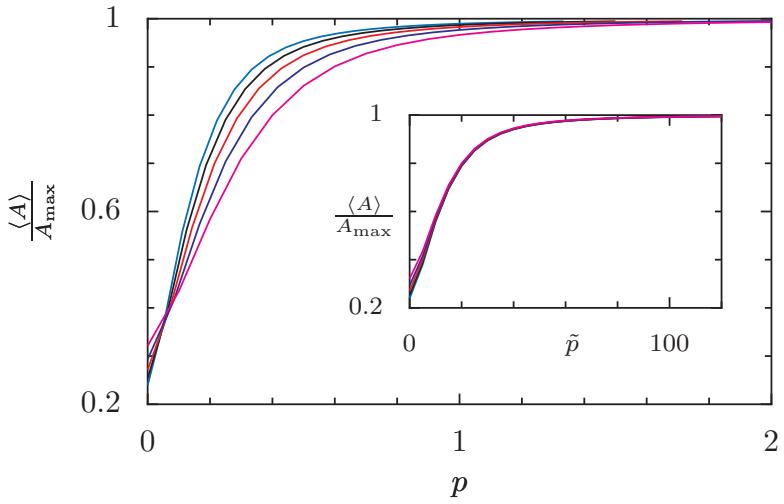

Figure 3.1: The variation of area with pressure p for self avoiding polygons on a square lattice. Inset: When plotted as a function of the scaling variable $\tilde{p} = pN$, the area curves for different values of N collapse onto each other. The system sizes used are $N = 50, 60, 70, 80, 90$. The data is generated from exact enumerations of the polygons on the square lattice [24].

3.3 Convex Polygons

In this section we calculate the equilibrium shape and area of a convex polygon when $\tilde{p} > 0$. Convex polygons are those polygons which have exactly 0 or 2 intersections with any vertical or horizontal line drawn through the midpoints of the edges of the lattice (see Fig. 3.2). We calculate the area by determining the shape of the convex polygon that minimises the free energy at fixed perimeter, generalising the calculation presented in Ref. [37].

The perimeter N of a convex polygon is the same as that of its bounding box, which, in general, is a rectangle. The equilibrium shape should however be invariant about rotations by angle $\pi/2$. The bounding box of the equilibrium shape is thus a square of side $N/4$. We can now calculate the shape in the first quadrant, obtaining the shapes in other quadrants by symmetry.

Consider a coarse grained shape $y(x)$ in the first quadrant with endpoints at $(0, N/8)$ and $(N/8, 0)$. The free energy functional for this curve $y(x)$ can be written

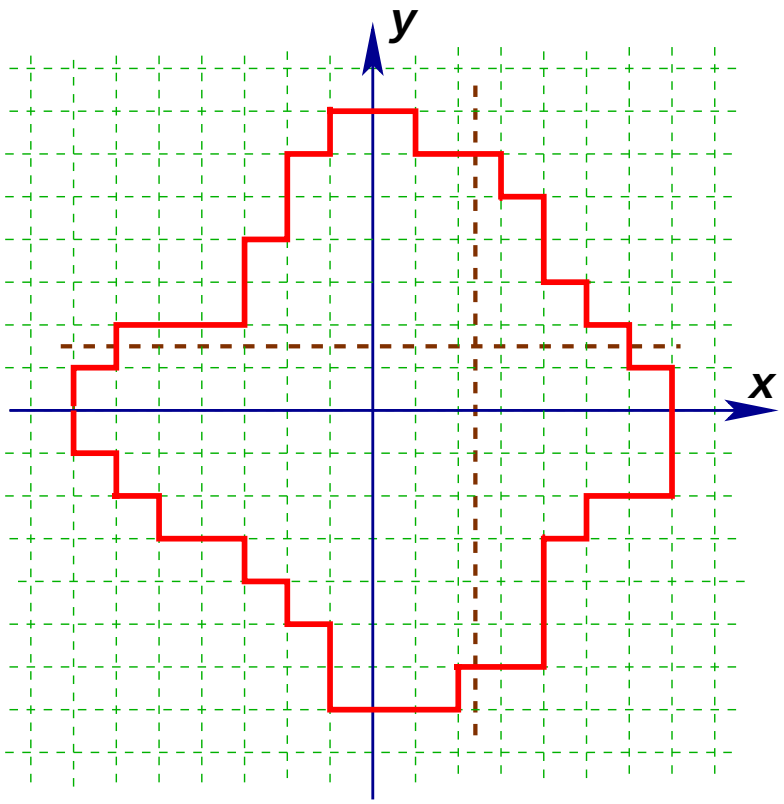

Figure 3.2: A representative diagram of a convex polygon. Any vertical or horizontal line (thick dashed lines) intersects the convex polygon at either 0 or 2 points.

as

$$\mathcal{L}[y(x)] = \int_0^{N/8} dx\, \sigma(y')\sqrt{1+y'^2} - \frac{\tilde{p}}{N}\int_0^{N/8} dx\ y, \tag{3.7}$$

where $\sigma(y')$ is the free energy per unit length associated with a slope y' and $\tilde{p}$ is the scaled pressure. The shape is then obtained obtained from Eq. (3.7) through the Euler Lagrange equation (Wulff construction) [41],

$$\frac{d}{dx}\frac{d}{dy'}\left[\sigma(y')\sqrt{1+y'^2}\right] = -\frac{\tilde{p}}{N}. \tag{3.8}$$

The free energy can be calculated using a simple combinatorial argument. Consider all possible paths starting from $(0, y)$ and ending at $(x, 0)$ with only rightward and downward steps. The weight of a path is $\exp(-Jb)$, where b is the number

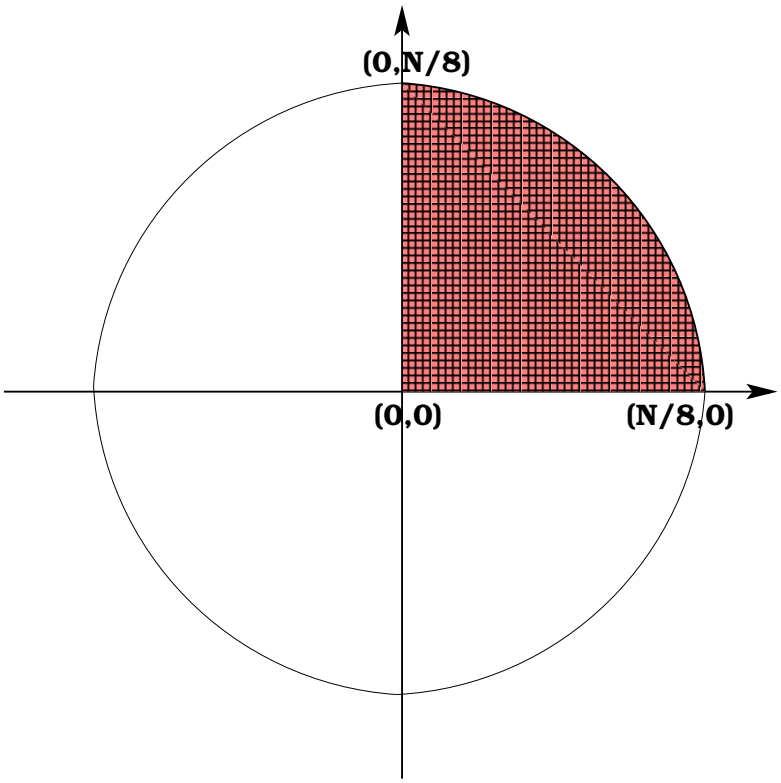

Figure 3.3: A schematic diagram of a convex polygon. We determine the equation of the bounding curve in the first quadrant.

of bends. When $x, y \gg 1$, the weighted sum of these paths will be equal to $\exp[-\sqrt{x^2+y^2}\sigma(y')]$, where y' is the mean slope of the path.

Let $C(x, y)$ be the sum of weighted walks constructed as above. Such walks may be enumerated by splitting the path into sequences of rightward and downward steps and associating the bending energy term to a sequence of downward (y) steps begun and terminated by a step to the right. Then

$$C(x,y) = \sum_{y_1,y_2,\ldots,y_X} \prod_i W_i \; \delta\left[\sum y_i - y\right], \tag{3.9}$$

where W_i is the weight associated with the i^{th} step, which is given by

$$W_i = [\alpha(1-\delta_{y_i,0}) + \delta_{y_i,0}], \tag{3.10}$$

and $\alpha = e^{-2J}$, with J being the cost of each $\pi/2$ bend. The delta function enforces the constraint that the steps taken in the y-direction must total y. The summation is over all possible numbers of steps taken in the y direction at steps $1, 2 \ldots x$.

Performing a discrete Laplace transform, we obtain

$$\begin{aligned} \sum_y C(x,y)\omega^y &\approx \left[1 + \alpha\omega + \alpha\omega^2 + \cdots\right]^x, \\ &= \left[\frac{1-(1-\alpha)\omega}{1-\omega}\right]^x. \end{aligned} \tag{3.11}$$

For large x, y, the inverse Laplace transform can be calculated using the saddle point approximation. This gives

$$\sigma(y') = \frac{-f(\omega^*)}{\sqrt{1+y'^2}}, \tag{3.12}$$

where

$$f(\omega) = y' \ln(\omega) + \ln[1-(1-\alpha)\omega] - \ln(1-\omega), \tag{3.13}$$

and ω^* satisfies

$$\left.\frac{df}{d\omega}\right|_{\omega^*} = 0. \tag{3.14}$$

This gives,

$$\left.\frac{df}{d\omega}\right|_{\omega^*} = \frac{y'}{\omega^*} + \frac{\alpha - 1}{1-(1-\alpha)\omega^*} + \frac{1}{1-\mu} = 0 \tag{3.15}$$

This implies,

$$\omega^* = \frac{-2y' + \alpha + \alpha y' + \sqrt{-4y'\alpha + \alpha^2 + 2\alpha^2 y' + \alpha^2 y'^2}}{2y'(\alpha - 1)} \tag{3.16}$$

Substituting Eqs. 3.12 and 3.13 into the Euler-Lagrange equation (Eq. 3.8), we get,

$$\frac{d}{dx}\frac{d}{dy'}\left[-y' \ln \omega^* - \ln[1-(1-\alpha)\omega^*] + \ln(1-\omega^*)\right] = -\frac{\tilde{p}}{N}. \tag{3.17}$$

Integrating, we obtain,

$$\ln \omega^* = \frac{\tilde{p}x}{N} + c. \tag{3.18}$$

Substituting the form of ω^* from Eq. 3.16, we obtain,

$$\frac{-2y' + \alpha + \alpha y' + \sqrt{-4y'\alpha + \alpha^2 + 2\alpha^2 y' + \alpha^2 y'^2}}{2y'(\alpha - 1)} = Ce^{\tilde{p}x/N}. \tag{3.19}$$

On simplifying, we get,

$$y'(x) = \frac{\alpha c e^{\tilde{p}x/N}}{(ce^{\tilde{p}x/N} - 1)(1 + ce^{\tilde{p}x/N}(\alpha - 1))}. \tag{3.20}$$

Integrating once more, we obtain for the equilibrium curve,

$$\begin{aligned} y(x) &= \frac{N[\ln(ce^{\tilde{p}x/N} - 1) - \ln(1 + ce^{\tilde{p}x/N}(\alpha - 1))]}{\tilde{p}} + c_1, \\ \Rightarrow \quad c_1 e^{\tilde{p}y/N} &= \frac{ce^{\tilde{p}x/N} - 1}{1 + ce^{\tilde{p}x/N}(\alpha - 1)}. \end{aligned} \tag{3.21}$$

If we define the scaled coordinates X and Y as $X = x/N$ and $Y = y/N$, the shape satisfies the equation

$$ce^{\tilde{p}X} + cc_1 e^{\tilde{p}(X+Y)}(1 - \alpha) - c_1 e^{\tilde{p}Y} = 1. \tag{3.22}$$

Now, symmetry requires that the equilibrium curve be invariant under interchange of X and Y, $X \leftrightarrow Y$. This implies that we must have

$$c_1 = -c, \tag{3.23}$$

and the equilibrium shape can be written as

$$ce^{\tilde{p}X} - c^2 e^{\tilde{p}(X+Y)}(1 - \alpha) + ce^{\tilde{p}Y} = 1. \tag{3.24}$$

The remaining constant can be fixed by the boundary condition that $y(x = N/8) = 0$. This gives,

$$\begin{aligned} & ce^{\tilde{p}/8} - c^2 e^{\tilde{p}/8}(1 - \alpha) + c = 1, \\ \Rightarrow \quad & c = \frac{(1 + e^{-\tilde{p}/8}) \pm \sqrt{(1 + e^{-\tilde{p}/8})^2 - 4e^{-\tilde{p}/8}(1 - \alpha)}}{2(1 - \alpha)} \end{aligned} \tag{3.25}$$

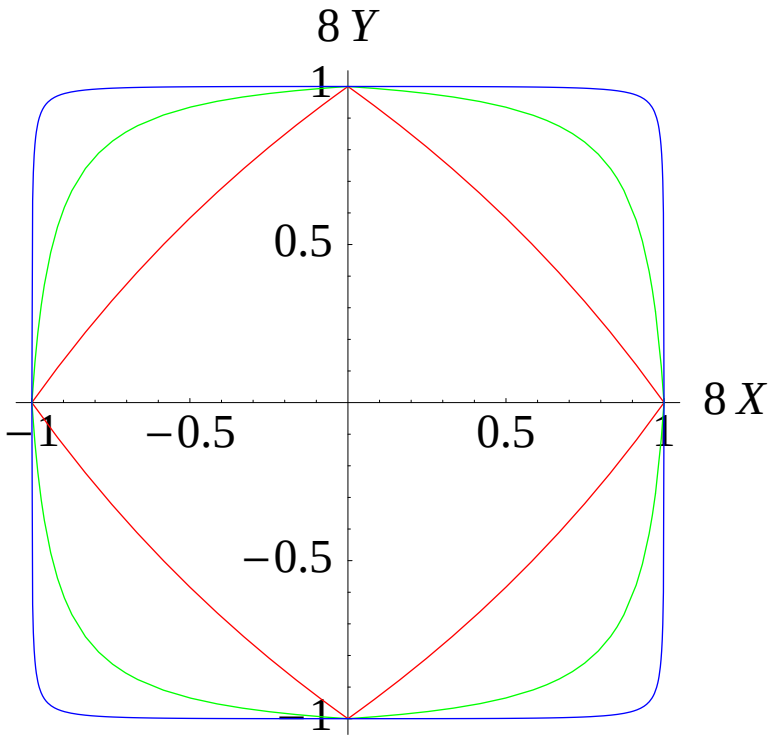

Figure 3.4: Shape of the convex polygon as obtained from Eq. (3.24) for polygons with $J = 1$. The different shapes correspond to pressure values $\tilde{p} = 1.0, 10.0, 50.0$, with the outer shape corresponding to largest pressure.

The sign is resolved by noting that the minus sign yields the correct asymptotic behaviour for the area. Thus, finally, we get the constants as,

$$c = -c_1 = \frac{(1 + e^{-\tilde{p}/8}) - \sqrt{(1 + e^{-\tilde{p}/8})^2 - 4e^{-\tilde{p}/8}(1 - \alpha)}}{2(1 - \alpha)}, \tag{3.26}$$

The shapes for different values of the scaled pressure are shown in Fig. 3.4 for a convex polygon with $J = 1$.

The area of the convex polygon is obtained from the equilibrium shape as

$$\langle A \rangle = 4N^2 \int_0^{1/8} Y dX, \tag{3.27}$$

where the factor of 4 corresponds to the four quadrants. Doing the integration, we

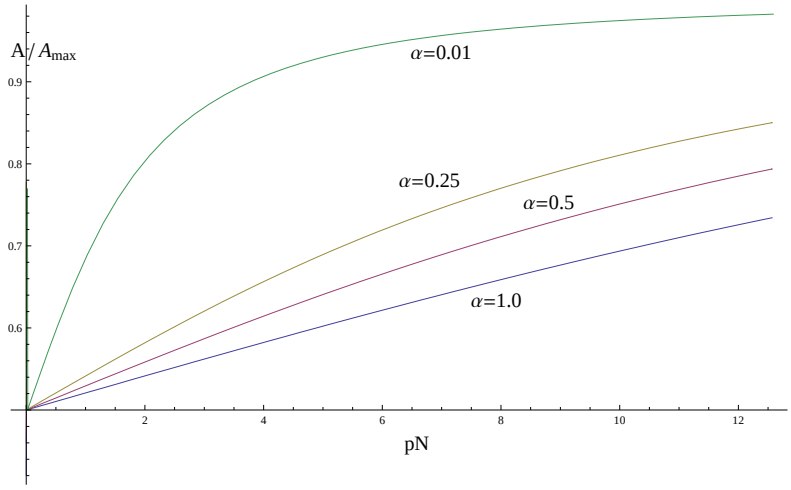

Figure 3.5: Area of a convex polygon from Eq. 3.28.

obtain

$$\begin{aligned}\langle A\rangle &= \frac{N^2}{16}\left[-\frac{8\ln(c)}{\tilde{p}}+\frac{64}{\tilde{p}^2}\left(\mathrm{Li}_2[c]-\mathrm{Li}_2[c\,e^{\tilde{p}/8}]\right.\right.\\ &+ \left.\left.\mathrm{Li}_2[c(1-\alpha)e^{\tilde{p}/8}]-\mathrm{Li}_2[c(1-\alpha)]\right)\right], \end{aligned} \tag{3.28}$$

where Li_2 is the dilogarithm function. The area as predicted by this equation is plotted in Fig. 3.5.

The asymptotic behaviour for large $\tilde{p}$ may be calculated from Eqs. (3.26) and (3.28). When $\tilde{p} \gg 1$, the constant c can be written as,

$$c = e^{-\tilde{p}/8} + \mathcal{O}(e^{-\tilde{p}/4}). \tag{3.29}$$

Substituting into Eq. (3.28), we obtain

$$\langle A\rangle = \frac{N^2}{16}\left[1-\frac{32\pi^2}{3\tilde{p}^2}+\frac{64}{\tilde{p}^2}\mathrm{Li}_2\left(1-\alpha\right)\right]+\mathcal{O}(e^{-\tilde{p}/8}). \tag{3.30}$$

When $J = 0$, the last term on the right hand side of Eq. (3.30) is zero and the relation reduces to

$$\langle A\rangle = \frac{N^2}{16}\left[1-\frac{32\pi^2}{3\tilde{p}^2}\right]+\mathcal{O}(e^{-\tilde{p}/8}), \quad J=0. \tag{3.31}$$

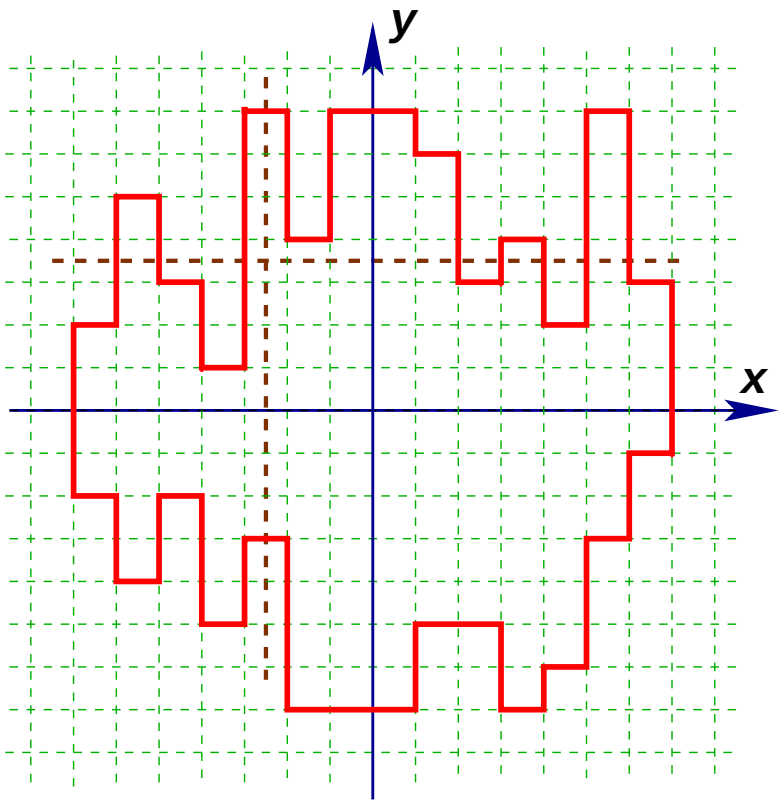

Figure 3.6: A representative diagram of a column-convex polygon. Any vertical line intersects the convex polygon at either 0 or 2 points.

3.4 Column-Convex Polygons

In this section, we calculate the shape and area of a column-convex polygon when $\tilde{p} > 0$. Column-convex polygons are those polygons which have exactly 0 or 2 intersections with any vertical line drawn through the midpoints of the edges of the lattice. There, is however, no such restriction in the horizontal direction (see Fig. 3.6). We calculate the area by determining the shape of the column-convex polygon that minimises the free energy for a fixed perimeter.

The perimeter of a column-convex polygon has no simple relation to its bounding box. We thus introduce a chemical potential μ that couples to the perimeter N. Consider a shape $y(x)$ with endpoints at $(-\beta N, 0)$ and $(\beta N, 0)$. The free energy

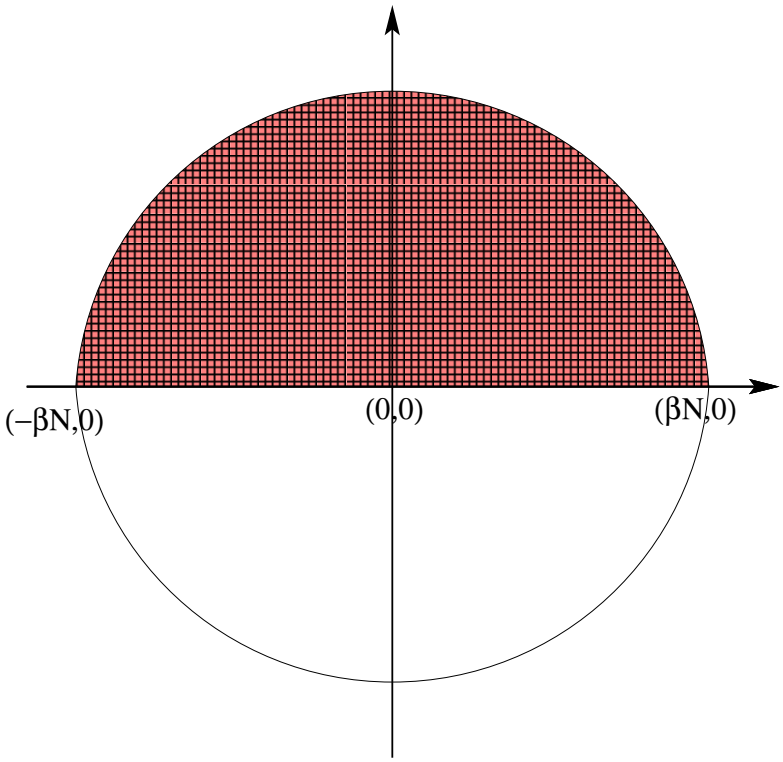

Figure 3.7: A schematic diagram of a column-convex polygon. We determine the equation of the bounding curve in the upper half plane.

functional for this curve $y(x)$ is given by

$$\mathcal{L}[y(x)] = \int_{-\beta N}^{\beta N} dx\, \sigma(y')\sqrt{1+y'^2} - \frac{\tilde{p}}{N}\int_{-\beta N}^{\beta N} dx\ y, \tag{3.32}$$

where, $\tilde{p}$ is the scaled pressure, $\tilde{p} = pN$. As before, $\sigma(y')$ represents the free energy per unit length associated with a slope y'. The Euler-Lagrange equation then gives the shape of the curve equilibrium curve $y(x)$.

The free energy may be calculated as follows. Consider all paths starting from (0,0) to (x, y). Let $C(x, y)$ be the weighted sum of all paths. Then, we obtain

$$C(x,y) = \sum_{y_1,y_2,\ldots,y_X} \prod_i W_i\ \delta\left[\sum y_i - Y\right], \tag{3.33}$$

where W_i is the weight associated with the i^{th} step and equals

$$W_i = \mu^{|y_i|}\left[\alpha(1-\delta_{y_i,0})+\delta_{y_i,0}\right]\mu. \tag{3.34}$$

Converting the δ-function in Eq. (3.33) into an integral, we obtain

$$\begin{aligned} C(x,y) &= \frac{1}{2\pi}\int_0^{2\pi} ds e^{-isy}\prod_i\sum_{y_i}\mu^{|y_i|+1}e^{isy_i}[\alpha(1-\delta_{y_i,0}+\delta_{y_i,0})], \\ &= \frac{1}{2\pi}\int_0^{2\pi} ds e^{-isy}\left[f(\mu,\alpha,s)\mu\right]^x, \end{aligned} \tag{3.35}$$

where

$$\begin{aligned} f(\mu,\alpha,s) &= \sum_y \mu^{|y|}e^{isy}[\alpha(1-\delta y,0)+\delta_{y,0}], \\ &= 1+\frac{\alpha\mu e^{is}}{1-\mu e^{is}}+\frac{\alpha\mu e^{-is}}{1-\mu e^{-is}}, \\ &= \frac{1+(1-2\alpha)\mu^2+\mu(\alpha-1)(e^{is}+e^{-is})}{(1-\mu e^{is})(1-\mu e^{-is})}. \end{aligned} \tag{3.36}$$

When $y \gg 1$, Eq. (3.35) may be evaluated by the saddle point method. Denoting y/x by y', we obtain

$$\sigma(y') = \frac{1}{\sqrt{1+y'^2}}\left[is_0y' - \ln\mu - \ln f(\mu,\alpha,s_0)\right], \tag{3.37}$$

where s_0 is the saddle point and is given by,

$$\frac{d}{ds_0}\ln f(\mu,\alpha,s_0) = iy'. \tag{3.38}$$

Substituting the expression for $\sigma(y')$ into the Euler-Lagrange equation (Eq. (3.8)) and using Eq. (3.38) we integrate once to obtain an equation for y'. This gives

$$\begin{aligned} y' &= \frac{\mu(\alpha-1)(ce^{-\tilde{p}x/N}-c^{-1}e^{\tilde{p}x/N})}{1+(1-2\alpha)\mu^2+\mu(\alpha-1)(ce^{-\tilde{p}x/N}+c^{-1}e^{\tilde{p}x/N})} \\ &\quad +\frac{\mu ce^{-\tilde{p}x/N}}{1-\mu ce^{-\tilde{p}x/N}}-\frac{\mu c^{-1}e^{\tilde{p}x/N}}{1-\mu c^{-1}e^{\tilde{p}x/N}}. \end{aligned} \tag{3.39}$$

The constant of integration c is fixed by the condition that the slope of the equilibrium curve is 0 ($y' = 0$) at $x = 0$. From Eq. 3.39, we then obtain,

$$\begin{aligned} 0 &= \frac{\mu(\alpha-1)(c-c^{-1})}{1+(1-2\alpha)\mu^2+\mu(\alpha-1)(c+c^{-1})}. \\ \Rightarrow \quad & \frac{(1-\alpha)(c-c^{-1})}{1+(1-2\alpha)\mu^2+\mu(\alpha-1)(c+c^{-1})} = \frac{c-c^{-1}}{(1-\mu c)(1-\mu c^{-1})}. \end{aligned} \tag{3.40}$$

Thus we can have either

$$\begin{aligned} & c - c^{-1} = 0, \\ \Rightarrow \quad & c = \pm 1. \end{aligned} \tag{3.41}$$

or,

$$\begin{aligned} & (1-\alpha)(1-\mu c)(1-\mu c^{-1}) = 1+(1-2\alpha)\mu^2+\mu(\alpha-1)(c+c^{-1}), \\ \Rightarrow \quad & \mu^2 = 1. \end{aligned} \tag{3.42}$$

Since μ cannot be a constant, the constant of integration is given by Eq. 3.41. We now need to determine the sign of the constant. This is done by noticing that the equilibrium curve y should have a maximum at $x = 0$, (see Fig. 3.7), i.e.

$$y''\big|_{x=0} < 0. \tag{3.43}$$

Differentiating Eq. 3.39, we obtain,

$$y''\big|_{x=0} = -\frac{2\tilde{p}c\mu}{N}\left[\frac{(\alpha-1)}{1+(1-2\alpha)\mu^2+2\mu(\alpha-1)c} + \frac{1}{(1-\mu c)^2}\right]. \tag{3.44}$$

If we consider the case, $\alpha = 1$ ($J = 0$), we obtain

$$y''\big|_{x=0} \overset{\alpha=1}{=} -\frac{2\tilde{p}c\mu}{N}\frac{1}{(1-\mu c)^2}, \tag{3.45}$$

which is less than zero if $c = 1$. On the other hand, if we consider the case $\alpha = 0$ ($J = \infty$), we obtain

$$y''\big|_{x=0} \overset{\alpha=0}{=} -\frac{2\tilde{p}c\mu}{N} \times 0 = 0. \tag{3.46}$$

If we now consider the variation of this second derivative at $x = 0$ as a function of α, we obtain,

$$\frac{\partial}{\partial\alpha}\left[y''\big|_{x=0}\right] = -\frac{2\tilde{p}c\mu(1-\mu^2)}{N[1+(1-2\alpha)\mu^2+2\mu(\alpha-1)c]^2}, \tag{3.47}$$

which is less than zero for all α if $c = 1$. Thus, this second derivative is a monotonically decreasing function of α when $c = 1$, and since we have shown that this derivative is zero for $\alpha = 0$ and negative for $\alpha = 1$, it follows that it must be less than zero for all all values of α. Thus the constant of integration is given by $c = 1$.

We can now integrate once more to obtain the equation of the equilibrium curve as

$$\begin{aligned} Y(X) = & \\ & -\frac{c_1}{\tilde{p}} + \frac{1}{p}\ln\left[\frac{(1-\mu e^{\tilde{p}X})(1-\mu e^{-\tilde{p}X})}{1+(1-\alpha)\mu^2+\mu(\alpha-1)(e^{\tilde{p}X}+e^{-\tilde{p}X})}\right]. \end{aligned} \tag{3.48}$$

As before, X and Y are defined as $X = x/N$ and $Y = y/N$. The constant of integration c_1 is fixed by the boundary condition $y(x = \beta N) = 0$. This gives,

$$c_1 = \ln\frac{(1-\mu e^{\tilde{p}\beta})(1-\mu e^{-\tilde{p}\beta})}{1+(1-\alpha)\mu^2+\mu(\alpha-1)(e^{\tilde{p}\beta}+e^{-\tilde{p}\beta})}. \tag{3.49}$$

The parameter β that determines the endpoint of the curve is still undetermined. It is chosen to be that β that minimises the free energy. The Lagrangian $\mathcal{L}_0$ for this curve $Y(X)$ is given by substituting Eqs. (3.48) and (3.49) into Eq. (3.32):

$$\begin{aligned} \mathcal{L}_0 = 2\beta N\int_0^1 dz & \\ & \left[\ln\frac{(1-\mu e^{\tilde{p}z\beta})(1-\mu e^{-\tilde{p}z\beta})}{1+(1-\alpha)\mu^2+\mu(\alpha-1)(e^{\tilde{p}z\beta}+e^{-\tilde{p}z\beta})} - \ln\mu\right]. \end{aligned} \tag{3.50}$$

The parameter β satisfies the equation

$$\frac{d\mathcal{L}_0}{d\beta} = 0. \tag{3.51}$$

This gives

$$g(\mu, J) \equiv e^{\beta_0 \tilde{p}} = \frac{1 - \mu + \mu^2 - \mu^3(1-2\alpha)}{2\mu[1+\mu(\alpha-1)]} + \frac{\sqrt{(1-\mu^2)[1-2\mu+\mu^2(1-2\alpha)][1-\mu^2(1-2\alpha)]}}{2\mu[1+\mu(\alpha-1)]}. \tag{3.52}$$

The chemical potential μ is determined by the constraint that total perimeter is N. This is equivalent to

$$\mu \frac{d\mathcal{L}_0}{d\mu} = -\frac{N}{2}. \tag{3.53}$$

μ then satisfies the equation,

$$-\frac{\tilde{p}}{4} = \ln \frac{1-\mu g}{g-\mu} - \ln g + \frac{2-a}{\sqrt{a^2-b^2}} \ln \frac{(a+b)(g+1)+\sqrt{a^2-b^2}(g-1)}{(a+b)(g+1)-\sqrt{a^2-b^2}(g-1)}, \tag{3.54}$$

where a and b are given by

$$a = 1 + (1-2\alpha)\mu^2, \tag{3.55}$$

$$b = 2\mu(\alpha - 1). \tag{3.56}$$

This solves the equilibrium macroscopic shape completely. The shapes given by Eq. (3.48) are plotted in Fig. 3.8 for column-convex polygons with $J = 1.0$.

We now determine the asymptotic behaviour of area when $\tilde{p} \gg 1$. This corresponds to the limit $\mu \to 0$. In this limit, $g(\mu, J)$ can be expanded as

$$g(\mu, J) = \frac{1}{\mu} - \alpha + \alpha(\alpha-1)\mu - \alpha(\alpha-1)^2\mu^2 + \mathcal{O}(\mu^3). \tag{3.57}$$

and Eq. (3.54) reduces to

$$\mu = e^{-\tilde{p}/8} + \mathcal{O}(e^{-\tilde{p}/4}). \tag{3.58}$$

Substituting the values of $g(\mu, J)$ and μ from Eqs. (3.57) and (3.58) into Eq. (3.50), we can obtain the Lagrangian in the (μ, N) coordinates to be

$$\mathcal{L}_0(\mu, N) = \frac{\tilde{p}N}{32} + \frac{2N}{\tilde{p}}[\mathrm{Li}_2(1-\alpha) - \frac{\pi^2}{6}] + \mathcal{O}(e^{-\tilde{p}/8}). \tag{3.59}$$

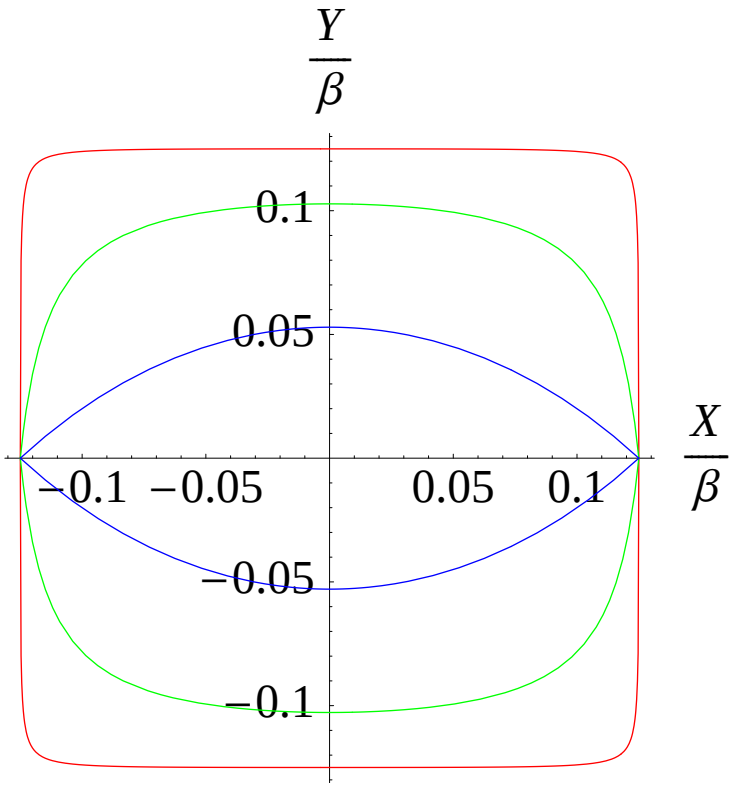

Figure 3.8: Shape of the column-convex polygon as obtained from Eq. (3.48) for polygons with $J = 1$. The different shapes correspond to pressure values $\tilde{p} = 3.0, 10.0, 50.0$, with the outer curve corresponding to the largest pressure. Both the X and Y axes are scaled by β.

The Lagrangian in the $(\tilde{p}, N)$ coordinates can then be obtained by a Legendre transformation as

$$\mathcal{L}_0(\tilde{p}, N) = \mathcal{L}_0(\mu, N) + \ln(\mu)\frac{N}{2}, \tag{3.60}$$

$$= \frac{-\tilde{p}N}{32} + \frac{2N}{\tilde{p}}[\mathrm{Li}_2(1-\alpha) - \frac{\pi^2}{6}] + \mathcal{O}(e^{-\tilde{p}/8}), \tag{3.61}$$

when $\tilde{p} \gg 1$.

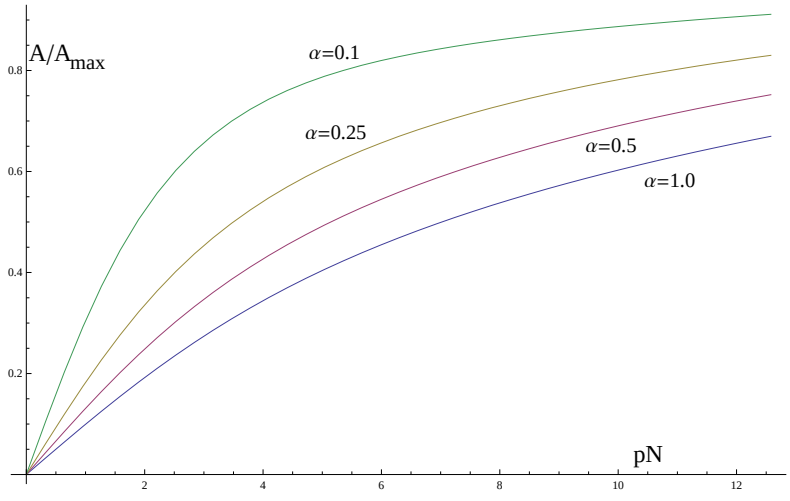

Figure 3.9: Area of a column-convex polygon from Eqs. 3.48, 3.52 and 3.54.

The area enclosed by the column-convex polygon is

$$A = -2N\frac{\partial \mathcal{L}_0}{\partial \tilde{p}}, \tag{3.62}$$

$$= \frac{N^2}{16}\left[1 - \frac{32\pi^2}{3\tilde{p}^2} + \frac{64}{\tilde{p}^2}\,\mathrm{Li}_2(1-\alpha)\right] + \mathcal{O}(e^{-\tilde{p}/8}), \tag{3.63}$$

where the factor 2 in Eq. (3.62) accounts for the lower half plane. Interestingly, Eq. (3.63) is identical to Eq. (3.30) which is the asymptotic area expression for convex polygons.

3.5 Self-avoiding and self-intersecting polygons

In this section, we study the asymptotic behaviour of self-avoiding and self-intersecting polygons. An analytic calculation along the lines of those presented for convex and column-convex polygons is not possible for self-avoiding polygons. However, we argue as follows: Convex polygons have no overhangs and the shape has four cusps. Introducing overhangs in one direction gives column convex polygons, reducing the number of cusps by two. Remarkably, the asymptotic behaviour of the area in the column-convex case [Eq. (3.63] coincides with that for convex polygons

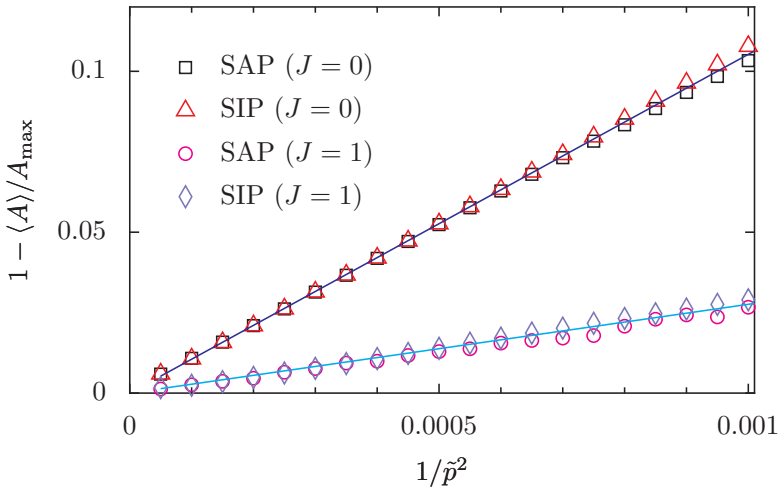

Figure 3.10: The asymptotic behaviour of the area for self-avoiding (SAP) and self-intersecting polygons (SIP). The solid lines correspond to the theoretical prediction of Eq. (3.64). The data is in good agreement with Eq. (3.64).

[Eq. (3.30)]. It is therefore plausible that introducing overhangs in both directions does not affect the asymptotic behaviour of the area, but merely removes the remaining two cusps, yielding a smooth shape. We therefore conjecture that the asymptotic behaviour of the area of self-avoiding polygons is given by

$$\langle A \rangle = \frac{N^2}{16}\left[1 - \frac{32\pi^2}{3\tilde{p}^2} + \frac{64}{\tilde{p}^2}\mathrm{Li}_2\left(1-\alpha\right)\right], \quad \tilde{p} \gg 1. \tag{3.64}$$

For self-intersecting polygons in the inflated phase, it is expected that the typical shape of the polygon does not intersect itself. Therefore, we argue that the area of self-intersecting polygons should also have the same asymptotic behaviour as in Eq. (3.64).

These conjectures may be verified numerically. When $J = 0$, the area of self-avoiding polygons may be obtained using exact enumeration data on the square lattice [25]. This data is available for lengths up to $N = 90$ [24]. When $J \neq 0$, there is no exact enumeration data available. We therefore resort to Monte Carlo simulations. We shall briefly describe the Monte Carlo algorithm in the next subsection. The system size used was $N = 800$.

For self-intersecting polygons, the area may be computed using exact enumer-

ation methods. We briefly describe the algorithm for the case $J = 0$. Consider a random walk starting from the origin and taking steps in one of the four possible directions. For each step in the positive (negative) x-direction, we assign a weight e^{-py} (e^{py}), where y is the ordinate of the walker. The weight is then e^{pA} for a closed walk enclosing an area A. Let $T_N(x, y)$ be the weighted sum of all N-step walks from $(0, 0)$ to (x, y). It obeys the recursion relation,

$$\begin{aligned} T_{N+1}(x, y) &= e^{-py}T_N(x-1, y) + e^{py}T_N(x+1, y) \\ &\quad + T_N(x, y-1) + T_N(x, y+1), \end{aligned} \tag{3.65}$$

with the initial condition

$$T_0(x, y) = \delta_{x,0}\delta_{y,0}. \tag{3.66}$$

For non-zero values of J, the ring is now a walk with a one-step memory, as explained in Chapter 2 (Sec. 2.3.2). As discussed in Sec. 2.3.2 this can be converted to a Markov process and the corresponding recursion relations are given by Eq. 2.8. Finally, $T_N(0, 0)$ gives the partition function of the self-intersecting polygons on a lattice. We used exact enumeration data up to $N = 150$.

In the case of all exact enumeration data, for each pressure point, we extrapolated to $N \to \infty$ using finite size scaling. For each pressure value, we determine the quantity $\Omega = 1 - A/A_{max}$ as a function of the systemsize N. This is assumed to have a correction with systemsize as

$$\Omega_N = a + \frac{b}{N}. \tag{3.67}$$

Using data for two N values, we can evaluate a as a function of N.

$$\begin{aligned} \Omega_{N+2} &= a + \frac{b}{N+2}, \\ \Omega_{N-2} &= a + \frac{b}{N-2}. \end{aligned} \tag{3.68}$$

This gives for a and b,

$$\begin{aligned} a_N &= \frac{(N+2)\Omega_{N+2} - (N-2)\Omega_{N-2}}{4}, \\ b_N &= \frac{(\Omega_{N-2} - \Omega_{N+2})(N+2)(N-2)}{4} \end{aligned} \tag{3.69}$$

Now using this value of a as a function of N for each pressure value, we do a further fit of the form

$$a_N = \lambda + \frac{\beta}{N^\gamma}. \tag{3.70}$$

This is fitted numerically and the resulting answer λ is plotted as a function of the pressure. The results of the numerical analysis is shown in Fig. 3.10. The numerical data agree very well with the theoretical prediction.

3.5.1 Monte Carlo Algorithm

The Monte Carlo algorithm we used to simulate lattice polygons follows the one described by Madras, Orlitsky and Shepp [30]. We shall now briefly describe this algorithm.

The lattice polygon is placed on a background grid which maintains a record of whether a specific site is empty or occupied. This ensures that checking for self-avoidance is a local operation. We start from some initial configuration, which was usually chosen to be a square, but it was verified that the results are independent of the starting configuration. The algorithm consists of two basic moves, the inversion move (Fig. 3.11) and the reflection move (Fig. 3.12). To determine which move is to be performed, we randomly select two monomers. If the monomers are separated by a distance of $\sqrt{2}a$, where a is the lattice spacing, i.e. the two randomly selected points are separated by a lattice diagonal, then both moves are possible and we choose either of them with a probability of 1/2. If this condition is not satisfied, however, then only the inversion move is possible.

If the two randomly chosen points are designated by k and l, the inversion move consists of rotating the section of the polygon between k and l about the midpoint of the line joining the two points k and l. The endpoints themselves remain unaffected by the transformation. The reflection move consists of reflecting all the points between k and l about the perpendicular bisector of the line kl. As

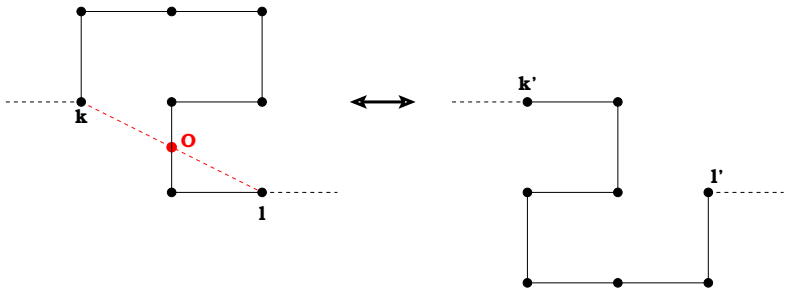

Figure 3.11: The inversion move for lattice polygons. All lattice points which lie between the two points k and l are rotated by 180^o about the point O.

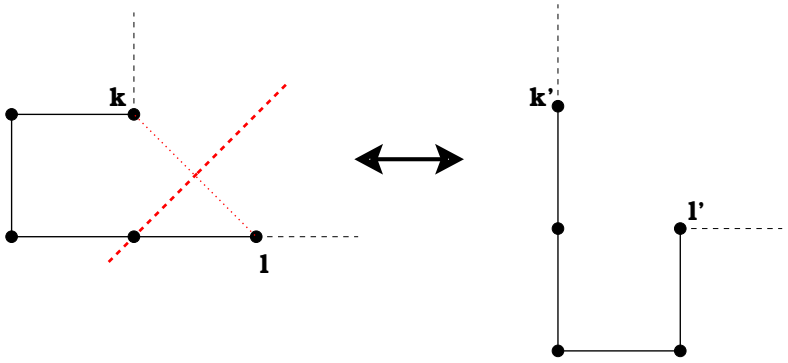

Figure 3.12: The reflection move for lattice polygons. All lattice points which lie between the two points k and l are reflected about the perpendicular bisector of the line joining the two points.

for the inversion move, the endpoints are unaffected by the operation. It can be explicitly shown that a combination of these two moves leads to an ergodic sampling of the phase space for two-dimensional SAWs [30].

Once we perform the relevant move, we find out the new positions of the polygon on the background grid. If the relevant sites were unoccupied previously, then the move is a valid one, and we can accept or reject in accordance with the Metropolis criterion. We let the system equilibrate for 4×10^6 steps and then run for 6×10^6 steps to calculate the thermodynamic averages.

3.6 Conclusions

We now summarise the basic results of this chapter. For different types of polygons, we studied the dependence of area on pressure, in the inflated regime. For convex and column-convex polygons, we calculated the area using the Wulff construction. We found analytic expressions for these two classes of polygons for all positive values of $\tilde{p}$, where $\tilde{p} = pN$ in the limit $p \to 0$, $N \to \infty$, keeping pN fixed. The asymptotic behaviour in the limit $\tilde{p} \gg 1$ was observed to coincide for both classes of polygons. We therefore conjectured that overhangs are not important in the inflated regime, and hence that self avoiding polygons should have the same asymptotic behaviour. This was verified numerically. We also showed numerically that self intersections were irrelevant in the inflated regime. These results continue to remain valid in the presence of a non-zero bending rigidity.

Interestingly, the asymptotic behaviour for continuum ring polymers differs from that of lattice polygons. In the continuum, the analogous relation for the area of pressurised rings is asymptotically [21, 32]

$$\frac{\langle A \rangle}{A_{max}} \longrightarrow 1 - \frac{2\pi}{\tilde{p}}, \quad \tilde{p} \gg 1. \tag{3.71}$$

This difference between continuum and lattice models is physically sensible in the expanded limit, since curvature in the lattice case is concentrated in local regions with $\pi/2$ bends but is delocalised along the contour in the continuum case.

While our conjectured result for self-avoiding polygons is in good agreement with numerical data, it would be of interest to have a mathematically rigorous derivation of this result. It may be possible to extend the methods of Ref. [35] to this problem.

4

Self-Avoiding Rings

4.1 Introduction

The shapes of three-dimensional fluid vesicles can be understood in terms of the energy minimizing configurations of a simple curvature Hamiltonian for a closed surface, computed under the constraints of fixed enclosed volume and surface area [8, 23, 11]. The full three-dimensional problem can be studied only numerically[2, 34, 19]. However, equivalent models in one lower dimension should provide useful insights into the three-dimensional case. Among the simplest of such models is a model of a self-avoiding polymer ring, whose enclosed area is constrained through a coupling to a pressure difference term [27, 14, 7, 15].

In the corresponding self-intersecting ring problem, defined by relaxing the self-avoidance constraint, Rudnick and Gaspari [42, 18] showed that there occurs a phase transition at a fixed value of the scaled pressure $\hat{p} = pN$. However, it has been the general belief that no such transition at non-zero pressure occurs in the case of polymer rings with self-avoidance, with the area generally believed to swell gradually with increasing pressure [31, 22]. Leibler, Singh and Fisher [27] showed that there exists a continuous phase transition at zero pressure, $p = 0$, which separates the collapsed phase from the inflated phase. However, their study failed to address satisfactorily the behaviour of the scaling functions for large arguments.

In later work, Maggs *et. al.*, [31] showed that applying scaling arguments consistently yields $A \sim N^3$. Thus, since a phase in which $A \sim N^2$ *must* describe the physical state of a pressurized polymer at sufficiently large pressure values, the expanded regime is inaccessible in arguments based on scaling about the fixed

point at $p = 0$, the validity of the scaling assumptions of LSF being confined to the regime in which $p << 1/N$.

In this Chapter, we shall study in detail the behaviour of the polymer ring in the inflated phase in an appropriate scaling limit. We study a wide class of models for self-avoiding ring polymers. We show that, by defining an appropriately scaled pressure variable $\hat{p} = pN$, an additional fixed point separating a weakly inflated from a strongly inflated phase becomes manifest at a constant value of the scaled pressure $\hat{p}_c$. In the rest of this chapter, we shall study the behaviour of the system around this new fixed point and characterise the nature of the phases on either side of the transition.

4.2 General model and results

The original model of LSF considers a system of N beads of diameter a connected by tethers with a maximum length $R_0 < 2a$. This constraint on the maximum length, while bestowing a certain advantage in maintaining the self- avoiding condition, obscures certain interesting features of the self-avoiding ring. In addition, modeling the connections between the beads as tethers is a rather special scenario. We use a more generalised model for the self-avoiding ring, beads of diameter a connected by springs of maximum length R_0, where $a < R_0 \leq \infty$. We also use different potentials $V(x, R_0)$ for the springs connecting the beads, and comment on the changes in the results obtained for different spring potentials. In Section 4.4 we shall provide a much more detailed description of the models we study.

We now provide a summary of the main results of our analysis. The original work of by Leibler, Singh and Fisher [27] and later study by Maggs et. al. [31] showed that there is a continuous second order phase transition at $p = 0$ from a branched polymer configuration to an inflated regime where $\langle A \rangle \sim pN^3$. At the transition point, the ring is described by self- avoiding walk statistics, $\langle A \rangle \sim N^{3/2}$. The area around $p = 0$ is described by

$$\frac{\langle A \rangle}{N^{3/2}} = f(pN^{3/2}). \tag{4.1}$$

Maggs et. al. showed that the scaling function for positive pressures may be

written in the form,

$$f(x) = a + bx, \tag{4.2}$$

which reproduces both the $N^{3/2}$ scaling at $p = 0$ and the N^3 scaling for large values of the argument.

Since in the truly inflated regime, the area must scale with N^2, the pressure in this regime must scale as $1/N$ in order for the Maggs analysis to hold. In fact, it is the scaled pressure $\hat{p} \sim pN$ which is the relevant variable in this regime. In order to take into account finite size corrections, we define the scaled pressure as

$$\tilde{p} = \frac{p}{4} \cot\left(\frac{\pi}{N}\right) \overset{N\to\infty}{\longrightarrow} \frac{pN}{4\pi}. \tag{4.3}$$

We now summarize our basic results:

- For point particles connected by quadratic springs, i.e. $V(x) = \frac{1}{2}kx^2$, the area diverges at a finite value of the scaled pressure, $\tilde{p} = k/2$.

- If there is a finite maximum extension R_0, then there is a transition such that $\lim_{\substack{N\to\infty \\ R_0\to\infty}} \frac{A}{A_{max}}$ is zero below the transition and non-zero above it.

- This transition separates a weakly expanded phase, in which the area scales as N^2, but is otherwise insensitive to the value of the cutoff scale R_0 - which represents the maximum bond-length, from a strongly expanded phase, in which the area scales as $(NR_0)^2$.

- Depending on the form of the potential, the transition between the weakly expanded and strongly expanded phases can be either first-order or continuous.

- For large R_0, this transition, if continuous, can be characterized through the scaling form for the average area:

$$\frac{\langle A \rangle}{N^2} \sim R_0^{\theta_1} f((\tilde{p} - \tilde{p}_c) R_0^{\theta_2}). \tag{4.4}$$

  where we estimate the values $\theta_1 \approx 0.67 \pm 0.1$ and $\theta_2 \approx 1.33 \pm 0.1$ from simulations. Note that the high pressure limit of the area implies that the

condtion $\theta_1 + \theta_2 = 2$ must always be satisfied. For $\tilde{p} > \tilde{p}_c$, we show that $\frac{\langle A \rangle}{N^2} \sim (1 - 1/\tilde{p})R_0^2$, while for $\tilde{p} < \tilde{p}_c$, we have $\frac{\langle A \rangle}{N^2} \sim (\tilde{p}_c - \tilde{p})^{-\theta_1/\theta_2}$.

- The transition can be characterized as a shape transition, in terms of the asphericity A_2 which measures the deviation away from spherical symmetry. Below the transition, the asphericity is found to be independent of R_0. while above the transition it scales as R_0^2.

- The transition can also be studied in terms of the variation of the angle between neighbouring bonds, θ. This goes from some intermediate value below the transition to the maximum possible value corresponding to a regular polygon shape above the transition.

- For a model with a finite value of the bead diameter to the maximum bond length ratio, a/R_0, there is a sharp crossover from the weakly to the strongly expanded phase. The phase transition then occurs if we take the limit $R_0/a \to \infty$.

Physically, this implies a scenario in which the ring expands without feeling the effect of the maximum extension R_0 below the transition, and feels it as soon as it reaches the critical pressure.

4.3 Scaling analysis

In this section, we shall present Flory-type scaling arguments for the self-avoiding rings. We follow the spirit of the scaling arguments that predict the finite pressure transition for self-intersecting rings, and then examine the corresponding predictions for the self-avoiding ring case.

The relevant terms in the Flory-type free energy are the contributions from self-avoidance, the pressurisation energy, the entropic term and the stretching energy. Thus the free energy can be written as,

$$\begin{aligned} F &\simeq F_{SA} + F_{pressure} + F_{entropy} + F_{stretching}, \\ &\simeq F_{SA} - pR^2 + \frac{R^2}{N} + F_{stretching}, \end{aligned} \tag{4.5}$$

The stretching free energy depends on the maximum bond length R_0. The exact dependence can be computed from the form of the potential between the bonds and it can be shown to be of the form $F_{stretching} = \frac{R^4}{R_0^2 N^3}$ (See Sec. 4.7) . Aside from the self-avoiding term, the remaining terms are exactly the same contributions that occur for the self-intersecting ring. As in that case, we can combine the second and third terms by defining a scaled pressure, $\tilde{p} = pN$,

$$F \simeq F_{SA} + \frac{R^2}{N}(1 - \tilde{p}) + \frac{R^4}{R_0^2 N^3}. \tag{4.6}$$

This leads us to expect that a phase transition occurs at some constant value of the scaled pressure pN.

In order to compute the exponents predicted by such a scaling analysis on either side of the transition, we need to estimate the contribution from the self-avoidance term.

The usual contribution from the self-avoidance is written as $F_{SA} = N^2/R^2$, which is estimated by assuming the N monomers to be distributed uniformly over a region of extent R, giving rise to a monomer density of $\rho = N/R$. The free energy is then estimated from $F_{SA} = \int \rho^2 dV$, where dV is the volume element. This form of the free energy then predicts a transition at $\tilde{p}_c$ but with different N exponents on either side of the transition. This predicts,

$$\langle A \rangle \sim \langle R^2 \rangle \sim \begin{cases} N^{3/2}/\sqrt{1-\tilde{p}}, & \tilde{p} < \tilde{p}_c \\ N^{5/3} R_0^{2/3}, & \tilde{p} = \tilde{p}_c \\ N^2 R_0^2 (\tilde{p} - 1), & \tilde{p} > \tilde{p}_c \end{cases} \tag{4.7}$$

This form of the free energy thus fails to capture the fact that the area goes as N^2 on either side of the transition, instead yielding different exponents in the three regimes. Interestingly, however, this does predict the divergence of the area with pressure below the transition point correctly (Eq. 4.25). Also, this yields the correct dependence of the area on the maximum bond length R_0 in all the three regimes (Eq. 4.26).

A fully consistent scaling analysis should yield the fact there is no different N scaling on either side of the transition. This can be obtained by assuming that the contribution to the free energy from self-avoidance can be written as $F_{SA} = N^2/R$.

This term can be interpreted if we assume that the polymer conformations are confined to a tube of diameter d, with d independant of R. This form of the free energy predicts for the area,

$$\langle A \rangle \sim \langle R^2 \rangle \sim \begin{cases} \frac{N^2}{(1-\tilde{p})^{2/3}}, & \tilde{p} < \tilde{p}_c \\ N^2 R_0^{4/5}, & \tilde{p} = \tilde{p}_c \\ N^2 R_0^2 (\tilde{p} - 1), & \tilde{p} > \tilde{p}_c \end{cases} \tag{4.8}$$

Thus, both of the above Flory-type scaling theories predicts the existence of a transition at a critical value of the scaled pressure. However the N^2 scaling on either side of the transition implies that the fluctuations are confined to within an annulus independent of the radius of the ring.

4.4 Definition of Models

The original version of the LSF models the self-avoiding ring as a system of N beads of diameter a connected by tethers with a maximum length $l_0 < 2a$. This constraint on the maximum length ensures that the self-avoiding nature of the ring is preserved. However, such a model has the difficulty that the minimum area allowed due to the finite diameter and the maximum area possible due to the length of the tether, are very close in value. This tends to make finite size effects more pronounced and the interpretation of various results may become ambiguous. In order to conclusively prove the presence of a finite pressure transition, we study the self-avoiding ring problem in the context of slightly different models, which differ in the nature of the beads as well as the nature of the bonds between them.

4.4.1 Model A: Infinitely Extensible self-avoiding ring with point beads connected by quadratic springs.

The first model we study is a self-avoiding generalisation of the Rudnick Gaspari Model for self-intersecting rings [42, 18]. In this model, the polymer ring is constituted of N monomer beads of radius zero, connected by springs which can extend

to infinity in accordance with a quadratic spring potential,

$$V(r) = \frac{1}{2}kr^2, \tag{4.9}$$

where r is the separation between two monomers.

The self-avoiding nature of the ring is taken into account by ensuring that the springs never intersect each other. It is known that the size of such non-intersecting polymer rings of zero thickness scale with the chain length N in the same way as a self-avoiding polymer with a finite excluded-volume [20, 33]. Thus we expect that the results obtained within this model will translate more generally into the case for self-avoiding polymer rings. However, as in the Rudnick-Gaspari Model, the absence of any upper cutoff on the spring length implies that it is not possible to access the truly inflated regime within this model.

4.4.2 Model B: Self avoiding ring with point beads connected by quadratic springs with a finite cutoff.

In order to access the inflated phase of the polymer ring, we need to impose an upper cutoff R_0 on the length of the springs connecting the monomers in the spring, and this sets an upper bound on the maximum area accessible by the ring, $A_{max} \simeq \frac{NR_0^2}{4\tan(\frac{\pi}{N})}$. In this model, we achieve this by defining the spring potential to be infinity beyond the cutoff length R_0. Thus in this model, the spring potential is given by

$$\begin{aligned} V(r) &= \frac{1}{2}kr^2, \quad r < R_0 \\ &= \infty, \quad r \geq R_0. \end{aligned} \tag{4.10}$$

The monomers are still point particles and self-avoidance is enforced by ensuring that the springs never intersect each other.

The spring constant k is a parameter of the model, and the critical pressure value can be determined as a function of this parameter from a simple $T = 0$ calculation. This can be seen easily by combining the contributions of the pressurization

energy and the spring energy. The pressurization energy is given by,

$$F_{pressure} = -pA = -4\pi^2\tilde{p}\frac{R^2}{N}. \tag{4.11}$$

The spring energy is given by,

$$F_{spring} = N\frac{1}{2}k\big(\frac{2\pi R}{N}\big)^2 = 2\pi^2 k\frac{R^2}{N}. \tag{4.12}$$

Adding these terms yield,

$$F_{pressure} + F_{spring} = 2\pi^2[-2\tilde{p} + k]\frac{R^2}{N}, \tag{4.13}$$

which then gives an expression for the critical pressure as a function of the spring constant,

$$\tilde{p}_c = \frac{k}{2}. \tag{4.14}$$

As a special case of this model, if the spring constant vanishes, $k = 0$, then we have a self-avoiding ring with point particles connected by tethers.

4.4.3 Model C: Self avoiding ring with point beads connected by springs with a logarithmic potential.

In this version of the model, we again modify the infinitely extensible version of the self-avoiding ring, as defined in Model A, to introduce an upper cutoff length R_0 on the springs. In this case, the upper bound is introduced by replacing the quadratic potential of the springs by a logarithmic potential which diverges as the length of the springs approaches R_0 while reducing to the quadratic potential for small values of the spring length. This is the Finitely Extensible Nonlinear Elastic (FENE) model for the polymer ring. The spring potential is thus now given by

$$\begin{aligned} V(r) &= -R_0^2 \ln\left(1 - \frac{r^2}{R_0^2}\right), \quad r < R_0 \\ &= \infty, \quad r \geq R_0 \end{aligned} \tag{4.15}$$

As in the case of Models A and B, the monomers constituting the ring are point objects and the self-avoidance constraint is also satisfied in a similar manner.

4.4.4 Model D: Self-avoiding ring with finite beads connected by springs.

The final model we study defines a more general model for self-avoiding rings. The ring is modeled as N self-avoiding beads of diameter a connected by springs with a maximum length R_0. Self-avoidance is ensured by ensuring that no bead overlaps with each other as well no bonds intersect each other. The spring potential is a simple quadratic potential with a cutoff at the maximum bond length R_0, i.e.,

$$\begin{aligned} V(r) &= \frac{1}{2}kr^2, \quad r < R_0 \\ &= \infty, \quad r \geq R_0. \end{aligned} \tag{4.16}$$

The controlling parameter in this model is the ratio of the bead diameter to the maximum bond-length,

$$0 \leq \delta \equiv \frac{a}{R_0} < 1. \tag{4.17}$$

In the limit $\delta = 0$, we recover the model with point beads, whereas for $\delta > 0.5$, we obtain the analog of the LSF model, albeit with springs instead of tethers. In this regime, self-avoidance of beads automatically implies self-avoidance of springs. Thus for $\delta > 0.5$, only bead intersections are important, while below this point, both bead and bond intersections play a role in maintaining self-avoidance.

The spring constant is chosen to be $k = 2$, noting that the results for other values of k may be obtained by simply rescaling the pressure axis as $\hat{p} \to 2\hat{p}/k$.

4.5 Monte Carlo algorithm

In this section, we will provide a detailed description of the Monte Carlo algorithm used to simulate the self-avoiding ring. The initial configuration is chosen to be a regular polygon of side $l = qR_0$ (see Fig. 4.1), where, $a/R_0 < q \leq 1$. It was verified that different initial conditions produce the same results.

In order to efficiently compute self-intersection checks for beads and bonds, we place the polymer ring onto a background lattice. For the bead-spring model, the background lattice is a square lattice with sides $a/\sqrt{2}$, which ensures that at most only one bead can occupy one background square. For the models with

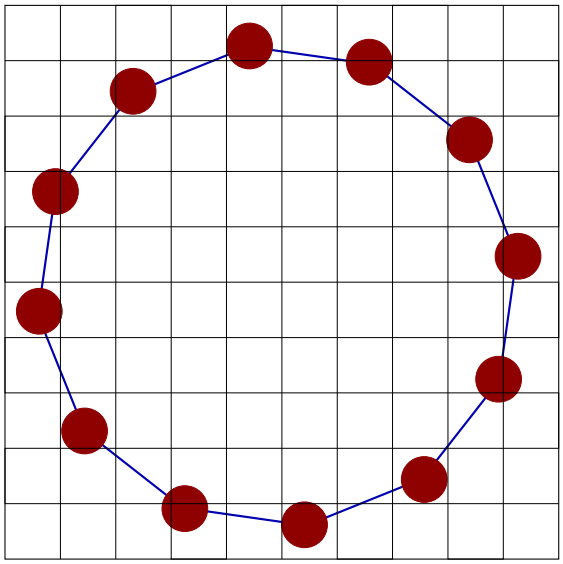

Figure 4.1: Schematic representation of initial configuration.

point particles, we choose appropriate sizes for the background grid, so that only few grids need to be checked in order to ensure self-avoidance. Typically, for simulations above the transition pressure, we choose grid squares with size R_0, while below the transition, the square has sides of order 1.

The basic Monte Carlo move consists of of picking any one bead at random and giving it an arbitrary kick (Fig. 4.2). The magnitude of the kick is chosen randomly between 0 and some parameter A, and the direction chosen to be some random angle between 0 and 2π. The parameter A is tuned such that roughly about half of all attempted moves are accepted.

The first check we perform is to ensure that the new bond lengths after the kick do not exceed the maximum bond length R_0 or becomes smaller than the diameter of the bead a. Since perturbing a single bead implies that only two bond lengths are modified in a move, this is a local check.

If the bond length constraint is satisfied, next we check that the new bead position does not overlap with any of the existing bead positions. We determine the new position of the perturbed bead with respect to the background grid. If the new grid square on which the bead is situated is already occupied, we reject the move. Furthermore, for the eight nearest neighbour grid boxes, we check if they are occupied, and if they are, then we ensure that the distance between the center

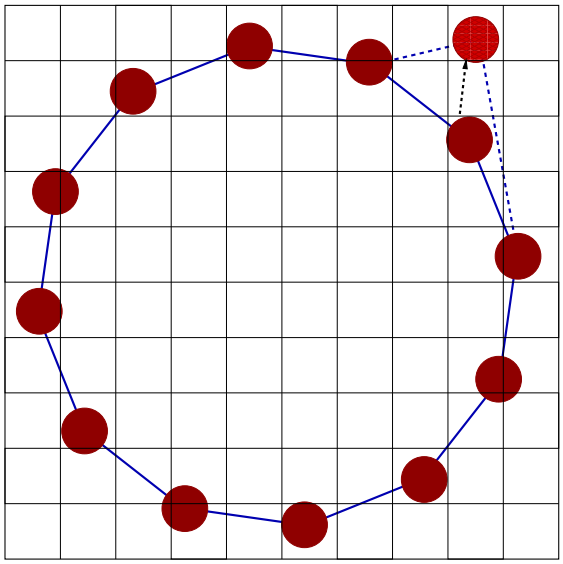

Figure 4.2: A sample attempted move.

of that bead and the perturbed bead is greater than the bead diameter (Fig. 4.3). The background grid thus reduces the self-avoidance check of the beads also to a local operation.

After ensuring that beads do not overlap, we need to check that the bonds do not intersect each other. At every point in the simulation, we keep track of the maximum bond length in the system. Then for a given grid size, this gives a radius within which we need to check the grids for intersecting bonds. For each of the two bonds which are affected by the perturbation, we calculate the point of intersection with all the bonds which lie within the radius as determined by the maximum bond length, except the nearest neighbour ones. If the point of intersection lies on the bond itself, we reject the attempted move (Fig. 4.4). Since this check is potentially more time consuming than the other checks, in the simulations, this check is performed only if the previous two checks have been satisfied.

Depending on which of the models described in Section 4.4 we are interested in simulating, we may or may not need all of the above checks. Only Model D, the generalised self-avoiding ring, needs all three checks, any of the others requiring only a subset of the three.

After we have verified that the attempted move satisfies all the relevant constraints, we calculate the energy of the new configuration. The total energy is the

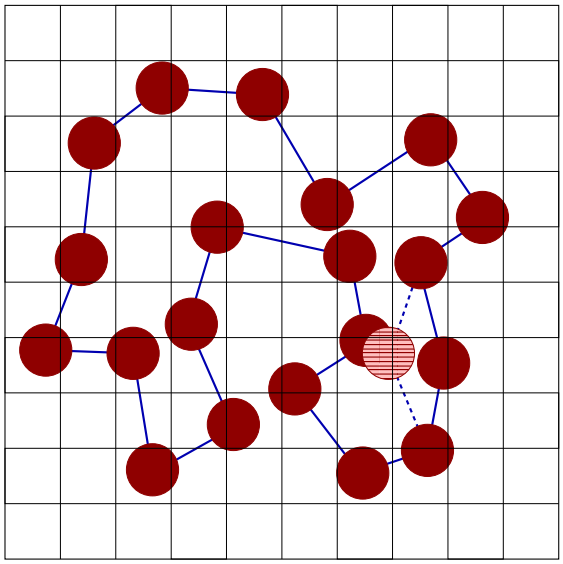

Figure 4.3: An attempted move violating self-avoidance of beads.

sum of the pressure contribution and the appropriate spring energy for the model. The move is accepted or rejected by the Metropolis algorithm. If the change in energy due to the perturbation is ΔE, then the move is accepted with a probability

$$prob = min(1, e^{-\Delta E/k_B T}). \tag{4.18}$$

which is the Metropolis acceptance rule. If the move is rejected, then we restore the perturbed bead to its old coordinates before the kick.

The simulation is allowed to run for T_1 Monte Carlo steps in order to allow the system to equilibrate before we start to take measurements of the various quantities we are interested in. After equilibration, the simulation is run for a further T_2 steps where we take measurements. Typically, $T_1 \sim 10^7$ steps while $T_2 \sim 5 \times 10^7$, although the exact values may depend on the system size being simulated. Reading are typically taken at a gap of $2 - 5$ Monte Carlo steps to ensure that different readings are not correlated.

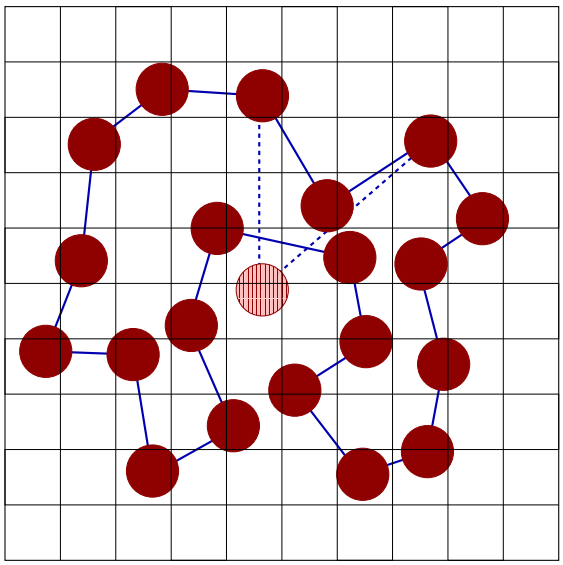

Figure 4.4: An attempted move violating self-avoidance of bonds.

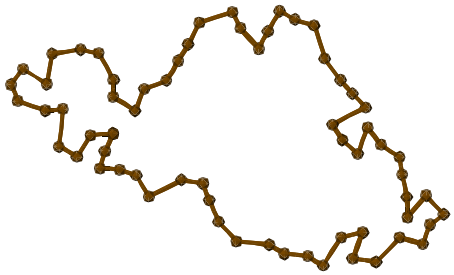

Figure 4.5: A snapshot of an actual configuration below the finite pressure transition. This configuration was obtained for the generalised self-avoiding ring, Model D.

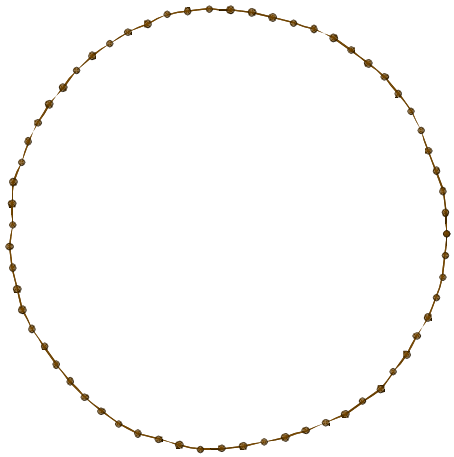

Figure 4.6: A snapshot of an actual configuration above the finite pressure transition. This configuration was obtained for the generalised self-avoiding ring, Model D.

4.6 Results

4.6.1 The order parameter

The phase transition from the weakly inflated to the strongly inflated phase is studied in terms of the area order parameter. We define the order parameter as the ratio of the average area to the maximum allowed area, $\Phi = A/A_{max}$. Here, $A_{max} = \frac{1}{4}NR_0^2\cot(\frac{\pi}{N})$. In the thermodynamic limit, defined as the double limit $N \to \infty$ and $R_0 \to \infty$, this order parameter should be zero below the transition $\tilde{p} < \tilde{p}_c$ and nonzero above it.

A second order continuous phase transition is characterised by a peak of the appropriately defined susceptibility at the transition point $\tilde{p}_c$. The area susceptibility is defined as

$$\chi = \frac{1}{A}\frac{\partial\langle A\rangle}{\partial\tilde{p}} = \frac{\langle\Phi^2\rangle - \langle\Phi\rangle^2}{N\langle\Phi\rangle}. \tag{4.19}$$

There exists a continuous phase transition as a function of the maximum bond length R_0 in several of the models we study. The order parameter around the critical point can then be described by a scaling function of the form

$$\Phi = R_0^{\theta_1} f((\tilde{p} - \tilde{p}_c)R_0^{\theta_2}). \tag{4.20}$$

Similarly, the susceptibility collapse around the transition can be described by a scaling function

$$\chi = R_0^{\zeta_1} f((\tilde{p} - \tilde{p}_c)R_0^{\zeta_2}). \tag{4.21}$$

We provide estimates of the various critical exponents from the Monte Carlo simulation.

4.6.2 Characterising the shape

This phase transition at a finite value of the critical pressure has implications for the shape of the ring on either side of the critical point. For low values of the pressure, below the transition point, the ring has an aspherical shape. Immediately above the transition, the ring assumes the shape of a regular N-gon. Any subsequent increase of the pressure inflates the ring as a whole without changing the overall

shape.

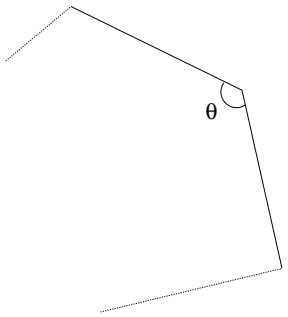

Figure 4.7: The angle between two neighbouring bonds.

The shape of the ring can be characterised by the gyration tensor. In particular, the sum of eigenvalues of the gyration tensor gives the radius of gyration for the configuration, while the difference between the eigenvalues measures the asphericity of the shape. The gyration tensor is defined as,

$$T_{\alpha,\beta} = \frac{1}{N}\sum_{i=1}^{N}(X_i - X_{CG})(Y_i - Y_{CG}), \tag{4.22}$$

where, (X_{CG}, Y_{CG}) represents the coordinates of the center of mass of the polymer ring. If we denote the eigenvalues of the gyration tensor as λ_1 and λ_2, the radius of gyration and the two-dimensional asphericity are defined as

$$R_g^2 = \lambda_1 + \lambda_2 \tag{4.23}$$

$$A_2 = \left(\frac{\lambda_1 - \lambda_2}{\lambda_1 + \lambda_2}\right)^2 \tag{4.24}$$

The asphericity is 0 for a perfectly spherical shape and 1 for a rod-like shape. We find that the asphericity is non-zero below the transition and goes to zero above it.

In addition to the asphericity, the extended shape of the ring above the transition can also be inferred by studying another property, the ratio of the average area to the average perimeter squared. If the ring assumes a circular shape with radius R, the quantity area by perimeter squared reaches its maximum value, $1/4\pi$. This is borne out by our simulations which shows that the ratio $\frac{4\pi A}{P^2}$ is less than 1 below

the transition and becomes 1 immediately above it.

Another direct measure of the shape change on either side of the fixed point is provided by studying the variation of the angle included between two neighbouring bonds, denoted by θ (Fig. 4.7). Across the transition, the angle goes from some intermediate value to the regular polygon value, $\theta_{max} = \pi - \frac{2\pi}{N}$.

4.6.3 Model A results

Fig. 4.8 shows the divergence of the area with the scaled pressure for Model A. In this model, there is no upper bound on the maximum length of the springs joining the monomers and the area diverges as we approach the critical point. The susceptibility also diverges as we approach the critical point. This is shown in Fig. 4.9.

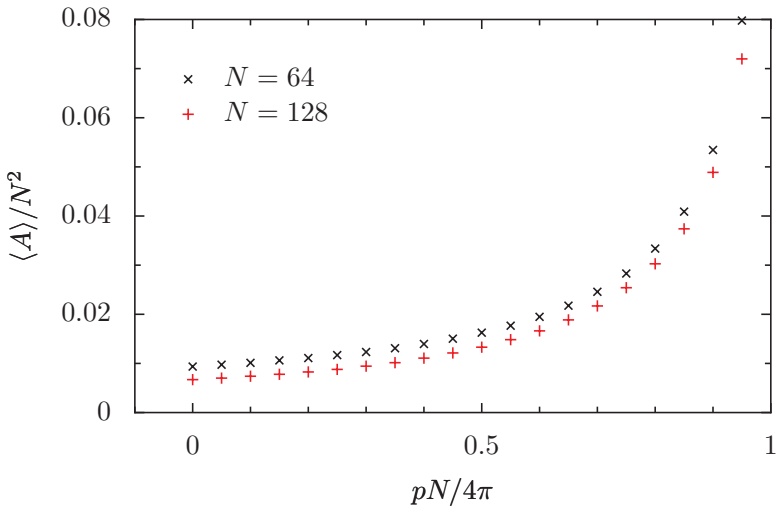

Figure 4.8: The divergence of the area as a function of the scaled pressure for the model with infinitely extensible springs, Model A. This is the self-avoiding version of the Rudnick-Gaspari model. The average area diverges as the pressure approaches the critical pressure.

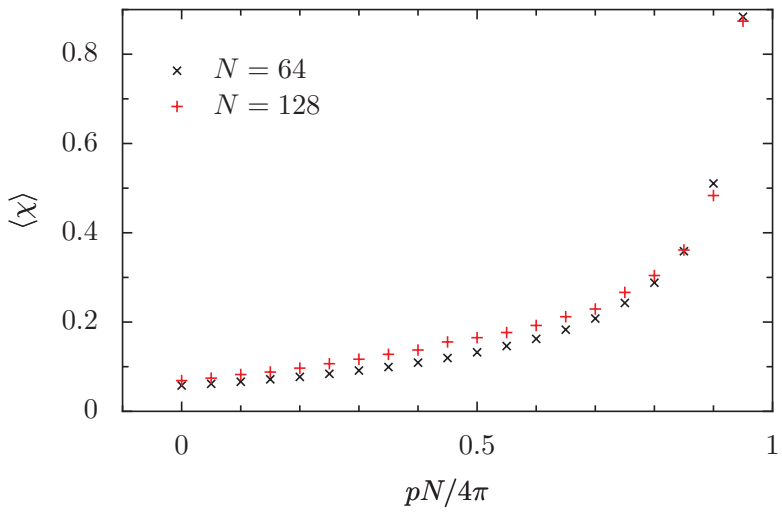

Figure 4.9: The area susceptibility as a function of the scaled pressure for the model with infinitely extensible springs, Model A. The susceptibility diverges as the pressure approaches the critical pressure.

4.6.4 Model B results

In Fig. 4.10, we plot the order parameter, the ratio of the average area to the maximum area as a function of the scaled pressure for Model B, point particles connected by quadratic springs. For a fixed value of the spring constant k, there is a transition at a fixed value of the scaled pressure. The order parameter is zero (provided $R_0 \to \infty$), below the transition and non-zero above it, showing a first order like jump at the transition point.

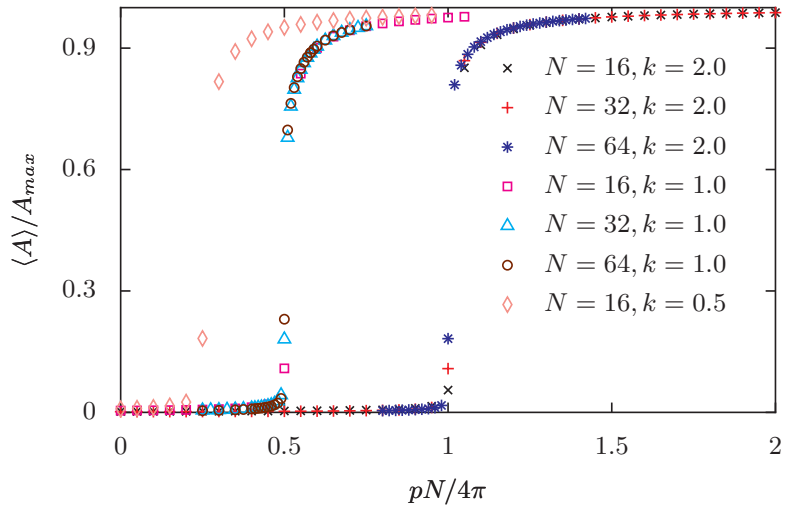

Figure 4.10: The order parameter plot for the model with quadratic springs with a maximum allowed length, Model B. The maximum bond length is $R_0 = 10$ for all models. The order parameter is zero below the transition and rises up sharply above it, approaching the maximum value, where $\langle A \rangle$ approaches A_{max}. The figure shows the order parameter plot for three different values of the spring constant k.

As can be seen from Fig. 4.10, as we decrease the spring constant k, the critical pressure also decreases. We plot the value of the critical pressure as a function of the spring constant in Fig. 4.11, verifying the linear relationship given by Eq. 4.14.

Fig. 4.12 shows the probability distributions for the order parameter for model B at three different values of the scaled pressure. For pressure values smaller than or greater than the critical pressure, the probability distribution is sharply peaked about the most probable pressure value. However at the critical pressure, all area values become equally likely and the probability distribution becomes flat. This curve is plotted at a spring constant value of $k = 2$, but similar behaviour is

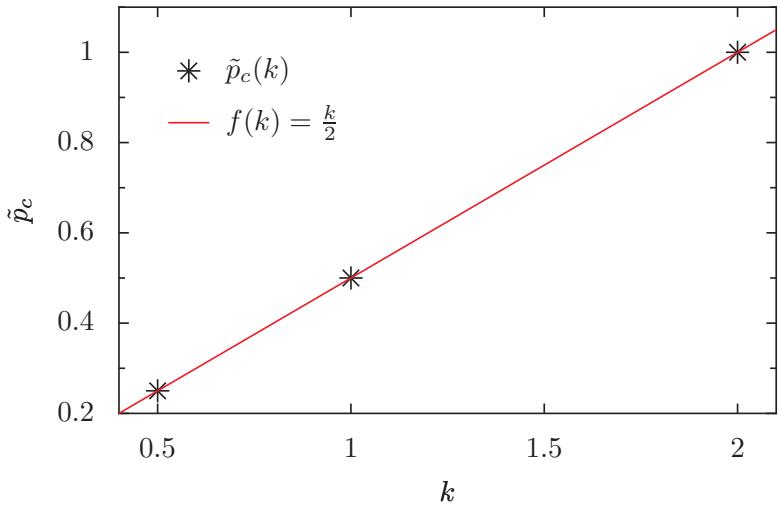

Figure 4.11: The variation of the critical pressure as a function of the spring constant for Model B. The critical pressure values were were determined from data for systems with $N = 16$ and $R = 10$.

observed for other values of the spring constant also.

In Fig. 4.13 we show the susceptibility plot with pressure for Model B, point particles connected by quadratic springs. There is a non-trivial N scaling at the transition point suggestive of a first order transition even when R_0 is finite.

In Fig. 4.14, we plot the asphericity as a function of the scaled pressure $\tilde{p}$ for Model B, point particles connected by quadratic springs. The asphericity is non-zero below the transition and zero beyond it, demonstrating that the ring becomes roughly circular beyond the transition point.

Another quantity that characterises the shape of a two-dimensional object is the ratio of the area to the perimeter squared. If the shape is circular and radius of the circle is R, the perimeter is $P = 2\pi R$ while the area is $A = \pi R^2$. Thus the ratio A/P^2 should go to $1/4\pi$, or $4\pi A/P^2$ should go to one. This behaviour is demonstrated for Model B in Fig. 4.15.

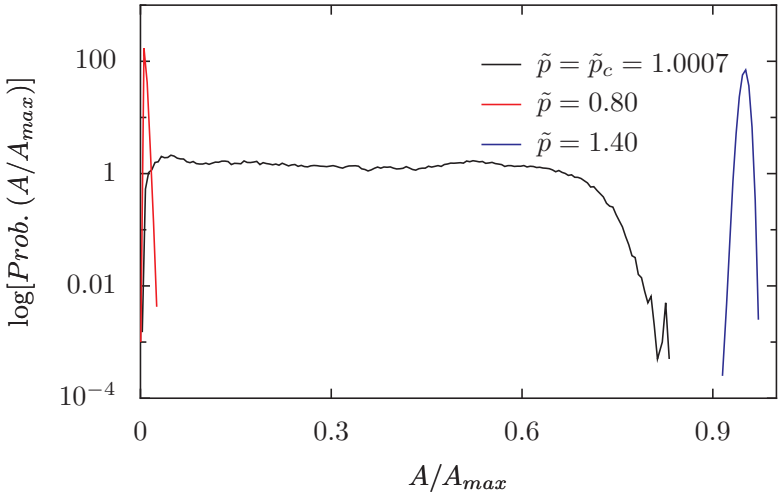

Figure 4.12: The probability distribution plots at three different pressures for the model with quadratic springs with a maximum allowed length, Model B. The spring constant is chosen as $k = 2$. The data shown is for $N = 64$ and $R_0 = 10$. For pressure values far away from the transition, both below and above the critical pressure, the probability distribution is sharply peaked about the most probable area value. However, at the transition point, the probability distribution is flat, indicating that all values of the area are equally sampled at the transition point.

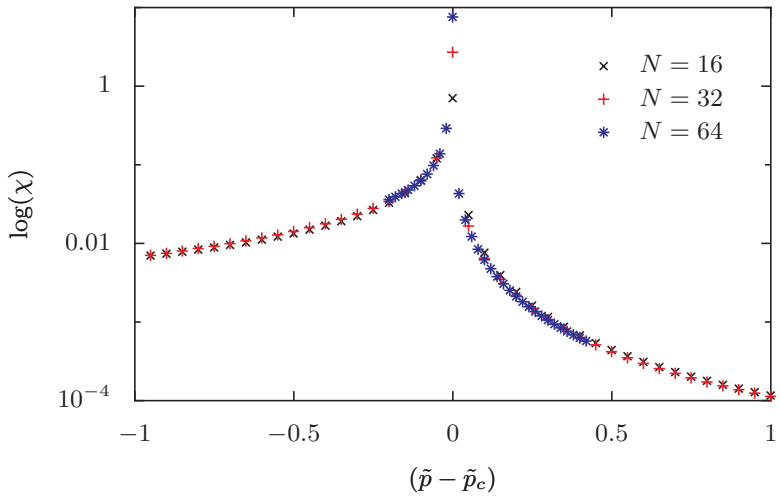

Figure 4.13: The susceptibility plot for different values of N for Model B, quadratic springs with a cutoff $R_0 = 10$, and spring constant $k = 2$. There is a nontrivial scaling with system size at the transition.

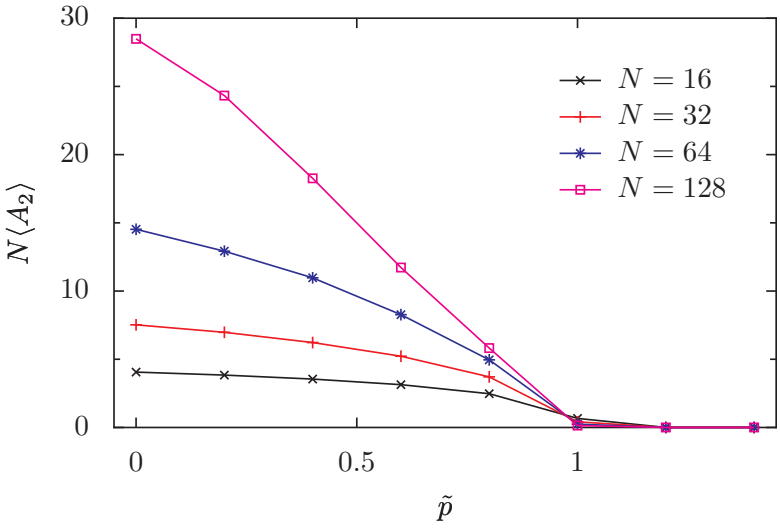

Figure 4.14: The asphericity plot on either side of the transition for the model with quadratic springs, Model B, with $R_0 = 30$ and $k = 2$. The shape becomes circular above the transition and consequently the asphericity becomes zero.

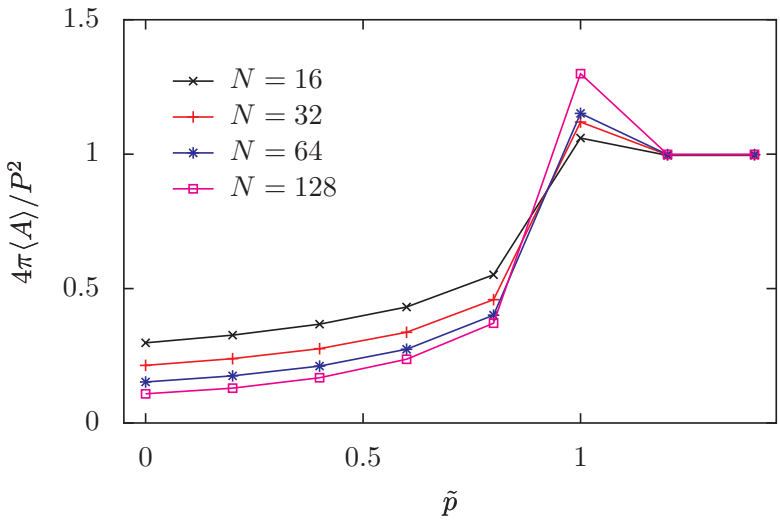

Figure 4.15: Ratio of area to perimeter squared for Model B. The maximum bond length is $R_0 = 30$ and the spring constant is $k = 2$. Above the transition, this ratio becomes 4π, indicating that the shape is a regular N-gon in this regime.

4.6.5 Model C results

In Fig. 4.16 we plot the corresponding order parameter plot for Model C, point particles connected by logarithmic springs. The order parameter is zero below the transition and nonzero above it, in the limit that $R_0 \to \infty$. However, unlike the quadratic potential case, the transition in this case is second order, with the order parameter showing no jump at the critical point.

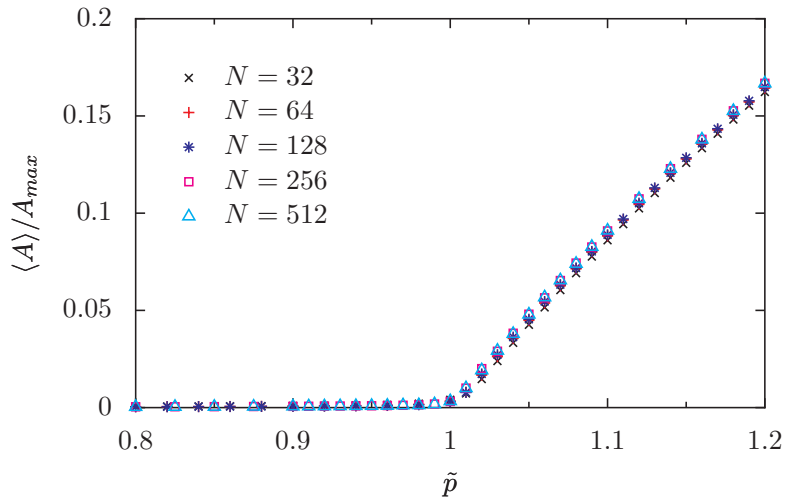

Figure 4.16: The order parameter plot for the model with logarithmic springs with a maximum allowed length, Model C. The maximum bond length used is $R_0 = 30$. The order parameter is zero below the transition and nonzero above it.

In order to study the dependence of the area on the system size N below the transition, we plot the area after subtracting the contribution at zero pressure as a function of the scaled pressure. The contribution at $p = 0$ scales differently with N and hence subtracting out this contribution gives cleaner statistics. This is shown in Fig. 4.17 for Model C, point particles connected by logarithmic springs. The data shows that the area scales with the square of the system size, $\langle A \rangle \sim N^2$ even below the transition.

It is also interesting to study how the area diverges with pressure as we approach the critical point. It is found that the divergence of the area, in the limit $R_0 \to \infty$ can be described by

$$\langle A \rangle \sim \frac{1}{(\tilde{p}_c - \tilde{p})^{\eta}}, \tag{4.25}$$

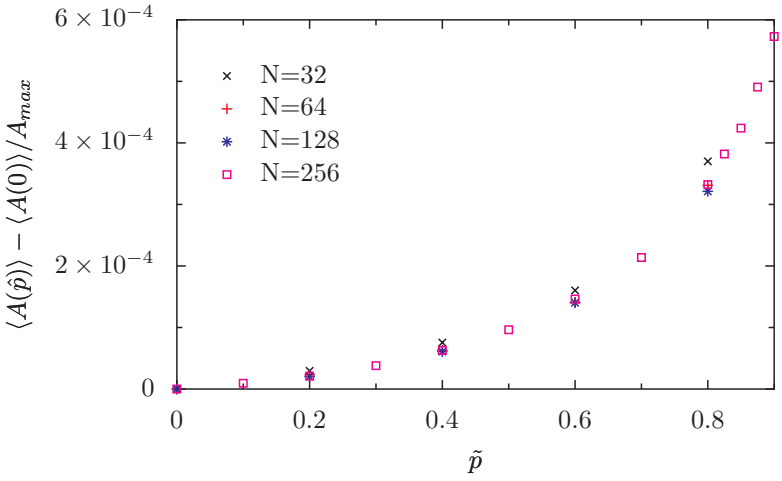

Figure 4.17: The area collapse as a function of the scaled pressure $\tilde{p}$ after subtracting out the contribution at $p = 0$ for the model with logarithmic springs with a maximum allowed length, Model C. The maximum bond length used was $R_0 = 30$. As discussed in text, area goes as N^2 below the finite pressure transition also.

with $\eta \simeq 0.5 \pm 0.1$ from simulation data. This behaviour is illustrated in Fig. 4.18.

Since there is no transition as a function of the system size, the susceptibility behaviour should not show any non-trivial scaling form. This is verified in Fig. 4.19 for Model C for three different system sizes.

Although the area scales as the square of the system size throughout the inflated phase, the scaling with the maximum extension R_0 of the bonds differs on either side of the transition. Below the transition, the area is independant of R_0, while in the strongly inflated phase, the area scales with R_0^2 as well as N^2. Around the transition point then, the area can be collapsed by a single scaling form. This is shown in Fig. 4.20 for Model C with a system size $N = 512$. The scaling equation that collapses data for different values of R_0 around the critical point is given by

$$\langle A \rangle \sim R_0^{\theta_1} f[(\hat{p} - \hat{p}_c) R_0^{\theta_2}], \tag{4.26}$$

with $\theta_1 \simeq 0.67 \pm 0.1$ and $\theta_2 \simeq 1.33 \pm 0.1$.

The scaling collapse of the susceptibility for Model C, with systems of the same system size ($N = 512$) but different maximum bond lengths R_0 is shown in

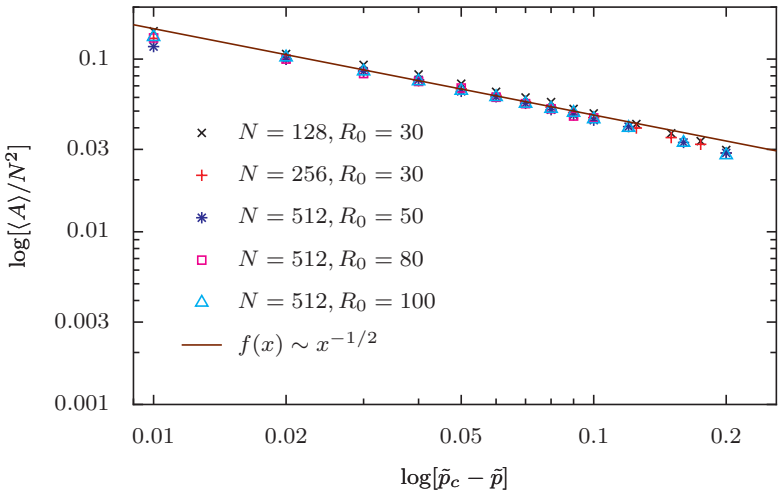

Figure 4.18: The divergence of area with pressure near the critical point for a range of system sizes and maximum bond lengths. The data is for the model with logarithmic springs, Model C.

Fig. 4.21. The scaling equation is given by Eq. 4.21. The critical exponents are found to be,

$$\zeta_1 = \zeta_2 \simeq 1.33. \tag{4.27}$$

In Fig. 4.22 we show the variation of asphericity for different values of the system size. The asphericity goes from being non-zero below the transition to zero above it, indicating that the configuration is spherically symmetric above the critical pressure. Below the critical pressure, the asphericity goes as the inverse of the system size.

In Fig. 4.23, we study the dependence of the asphericity on the maximum bond length R_0 above the critical pressure. The inverse of the asphericity is found to scale as the square of maximum extension, $A_2^{-1} \sim R_0^2$. The data shown is for Model C. The inset shows the unscaled plots for the asphericity.

Fig. 4.24 plots the ratio $4\pi A/P^2$ as a function of the pressure. As discussed earlier, this quantity also measure the shape of the ring. As expected this ration goes to 1 above the transition point, indicating that the shape becomes circular beyond this point.

The angle between two neighbouring bonds also undergoes a transition at the critical pressure, rising from an intermediate value to the maximum value $\pi - 2\pi/N$.

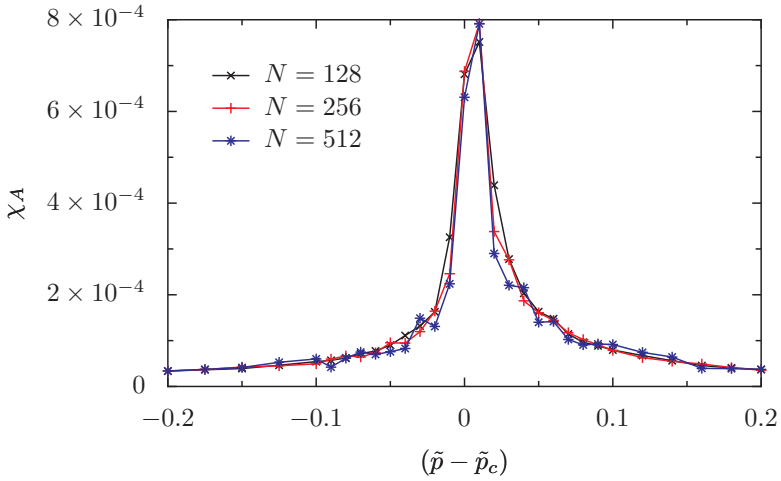

Figure 4.19: The variation of χ_A with $\tilde{p}$ for different N. The data is for the logarithmic spring model, Model C, with $R_0 = 30$. The curves collapse on top of each other.

This behaviour is shown in Fig. 4.25.

The radius of gyration, R_g provides a measure of the size of the ring. If we subtract the contribution at $p = 0$, we can easily see that the square of the radius of gyration scales with the square of the system size. This behaviour is expected, since the average area, which is of the order of R_g^2, is known to scale as N^2. This is shown in Fig. 4.26 for Model C.

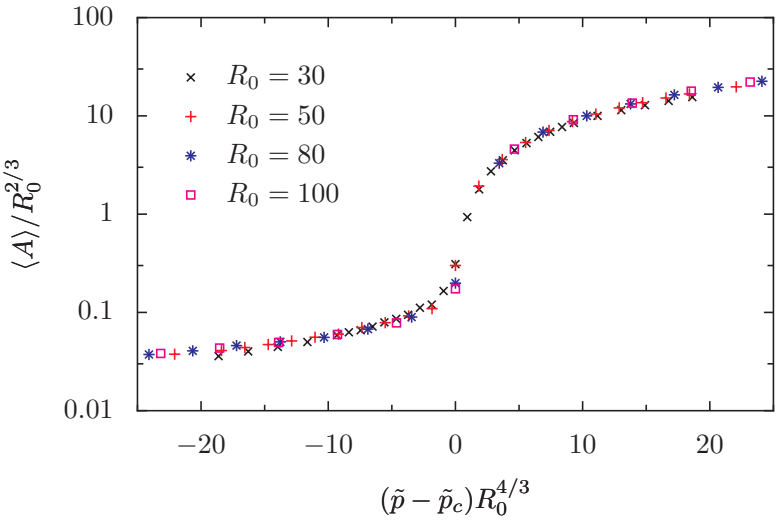

Figure 4.20: Scaling collapse of the area around the critical pressure $\tilde{p}_c$ for different values of the maximum allowed length R_0 for Model C, with logarithmic springs. The system size used is $N = 512$.

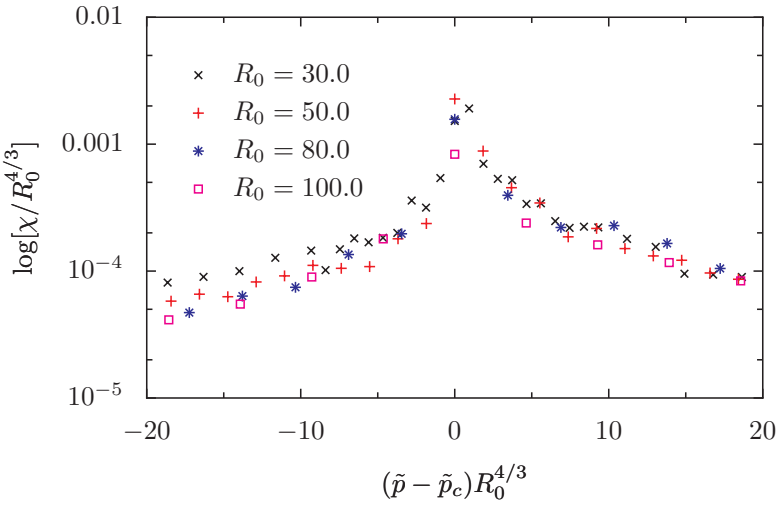

Figure 4.21: Scaling collapse of the susceptibility for different values of the maximum allowed length R_0 for Model C, with logarithmic springs. The system size used is $N = 512$.

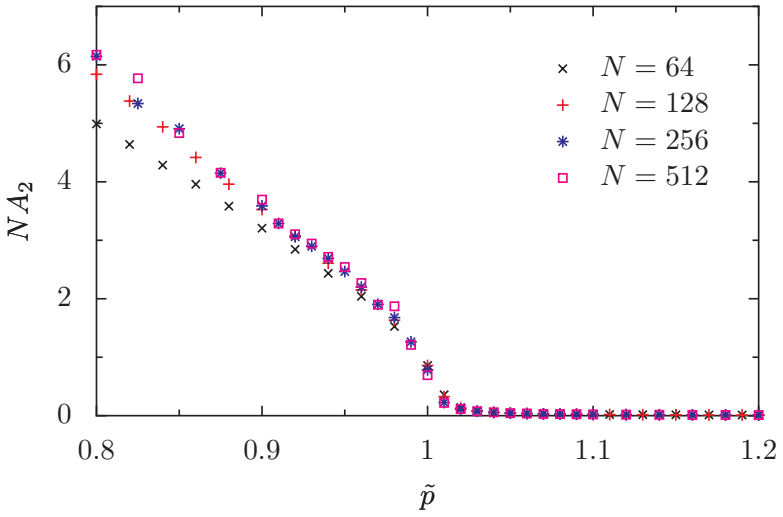

Figure 4.22: The asphericity plot about the critical point for Model C, monomers connected by logarithmic springs, with $R_0 = 30$.

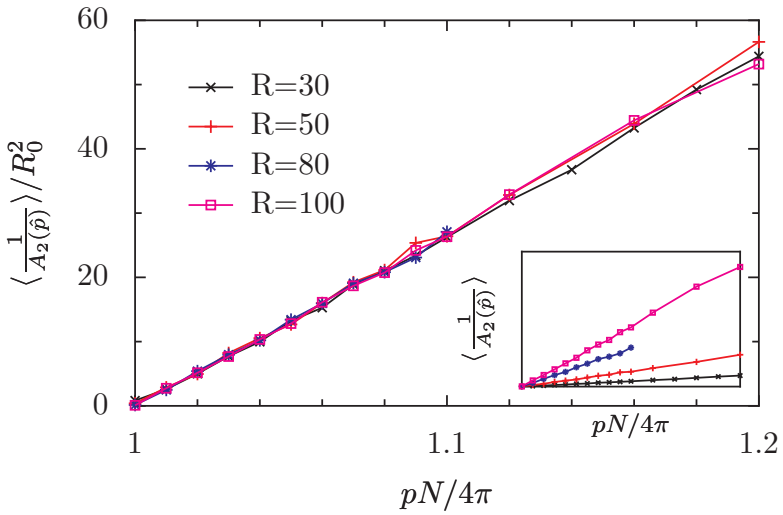

Figure 4.23: Above the critical point, the asphericity for different values of R_0 goes down as R_0^{-2}. The data is for Model C, monomers connected by logarithmic springs. The inset shows the unscaled data. The system size used is $N = 512$.

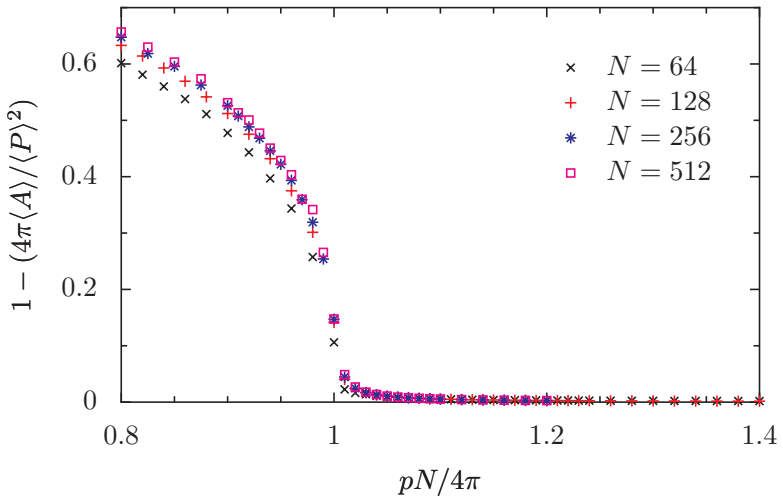

Figure 4.24: Ratio of area to perimeter squared for Model C with $R_0 = 30$. Above the transition, the shape becomes a regular N-gon.

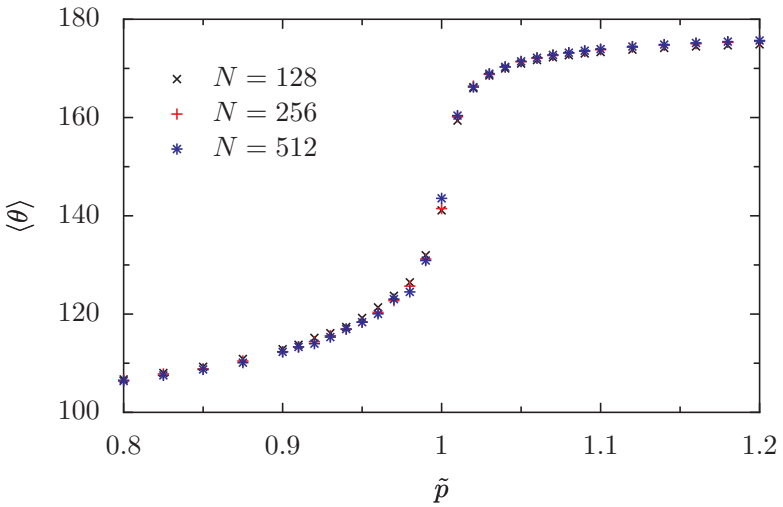

Figure 4.25: Angle between neigbouring bonds for Model C for different system sizes with $R_0 = 30$. Above the transition, the angle goes to its maximum possible value.

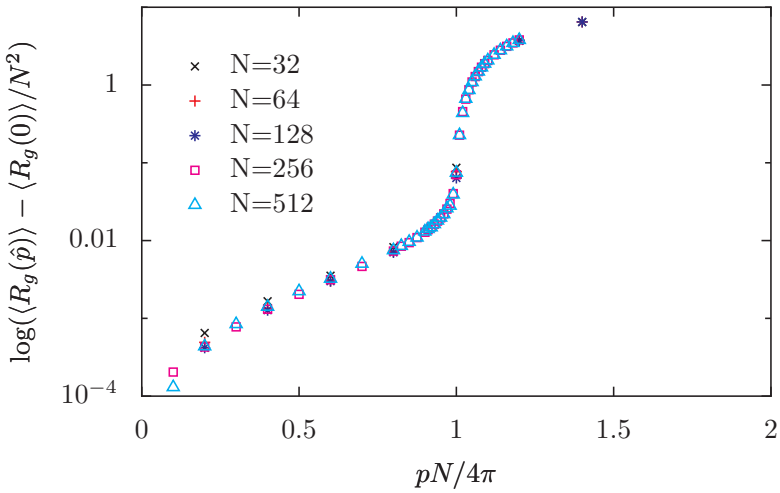

Figure 4.26: The radius of gyration, after subtracting out the relevant quantity also collapses when plotted against the scaled pressure $\tilde{p}$. The data is for Model C with $R_0 = 30.0$.

4.6.6 Model D results

For the generalised self-avoiding ring problem, as defined by Model D, different limits may be explored by tuning the parameter $\delta = a/R_0$. We do this by fixing the bead diameter $a = 1.0$ and then varying R_0 and looking at the order parameter. For large values of R_0, there is a discrete jump at a critical pressure $\hat{p}_c$. As we decrease the value of R_0, the jump becomes progressively less pronounced until for very small values of R_0, $R_0 = 2a$, the order parameter curve does not appear to show any discontinuities. This is shown in Fig. 4.27. In order to understand the full features of the problem, we plot the susceptibilities for different values of R_0. For $R_0 = 2a$, the susceptibility peak scales as $pN^{3/2}$, the LSF scaling variable (see Fig. 4.28). When plotted against $\hat{p} = pN$, the peaks shift toward zero with increasing system size. This is shown in the inset of Fig. 4.28. The opposite limit is demonstrated in Fig. 4.30 for $R_0 = 30a$, where the susceptibility peak clearly scales as a function of $\hat{p} \sim pN$. For intermediate values of R_0, say $R_0 = 3a$, we observe two coexisting peaks in the susceptibility plot. This is shown in Fig. 4.29. The peak on the right scales as pN whereas the peak on the left scales as $pN^{3/2}$. This is shown in the inset of Fig. 4.29. Although an apparent discontinuity exists for $R_0 \geq 3$, the fact that all the curves appear to have a common intersection point as well as the observation of a large pretransitional variation, suggest that this may be a sharp crossover. Since there is good evidence for a transition in the limit of zero bead size (as in models A, B and C), it would seem that there is a singularity only in the limit $a/R_0 \to 0$, corresponding either to a vanishing bead size or the limit when $R_0 \to \infty$.

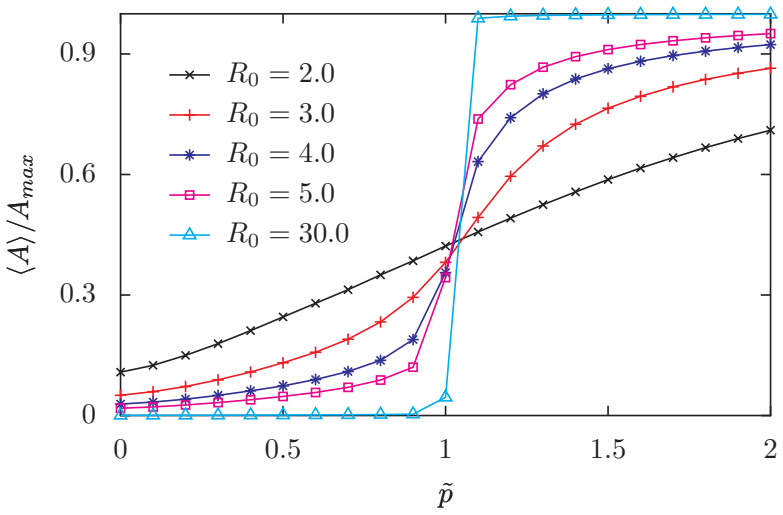

Figure 4.27: The order parameter for different values of the maximum allowed length R_0 for the generalised self-avoiding ring model, Model D. As the cutoff length R_0 decreases, the jump in the order parameter also become less pronounced, until it become completely smooth at $R_0 = 2.0a$. Here we have chosen $a = 1.0$, $k = 2.0$ and $N = 64$.

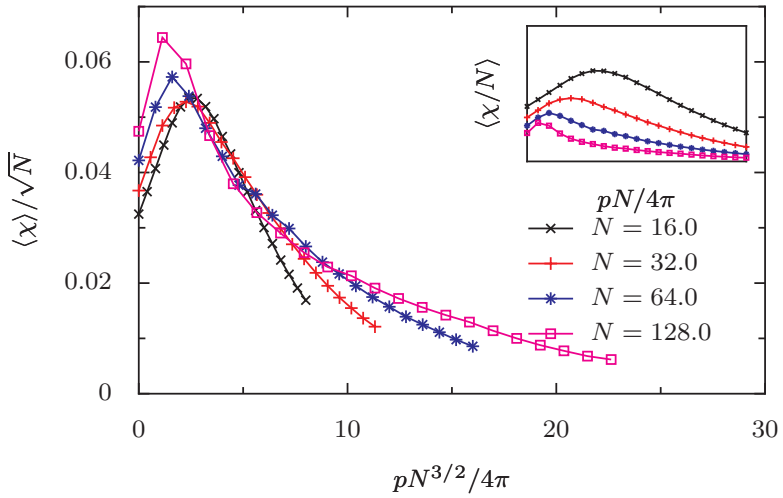

Figure 4.28: The susceptibility plots for different lengths for Model D with $R_0 = 2a$ and $k = 2.0$. The peak in the susceptibility scales as $pN^{3/2}$. The inset shows the same data plotted against pN, where the peaks can be seen to be shifting toward zero as we increase the N value.

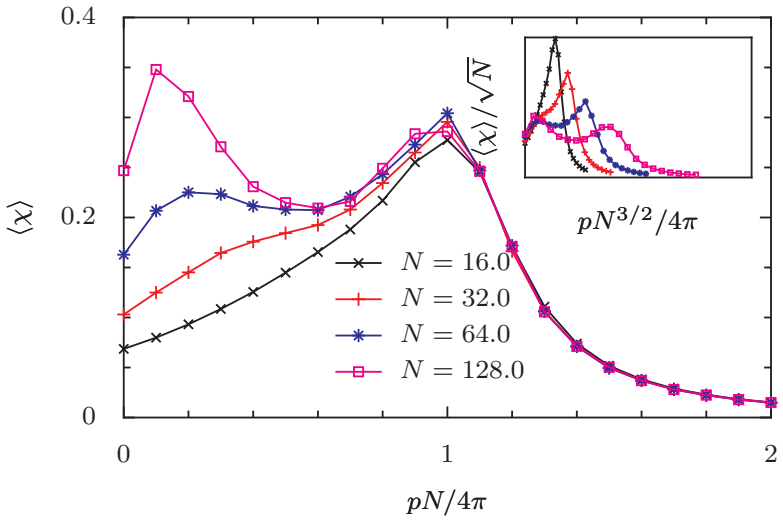

Figure 4.29: The susceptibility plots for different lengths for Model D with $R_0 = 3a$. The susceptibility plot now shows two distinct peaks. The right peak scales with pN. This is shown in the main figure. On the other hand, the left peak scales with $pN^{3/2}$. This is shown in the inset. As in the previous figure, the left peak shifts toward zero with increasing N when plotted against the scaled pressure pN.

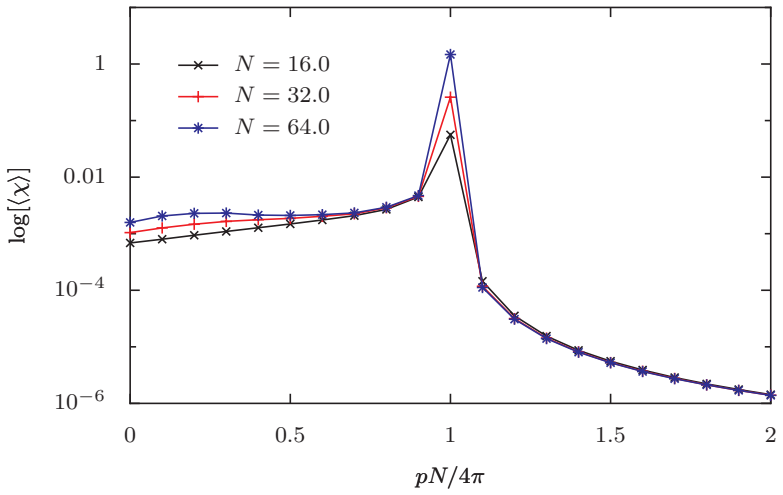

Figure 4.30: The susceptibility plots for different lengths for Model D with $R_0 = 30a$. The peak at $pN = 1$ is now the dominant peak. This swamps out the smaller peak near $p = 0$ which scales as $pN^{3/2}$.

4.7 Discussion

Clearly, in the light of the different results presented in the previous section, we need to provide a modified approach to the scaling description that can explain the observed facts. The results of the previous section shows that the scaling variable pN is the correct choice to describe the system in the inflated phase.

At a constant value of this scaled pressure, $\tilde{p}_c$, we show that there exists a phase transition in the limit that $N \to \infty$, $R_0 \to \infty$, while any finite value of R_0 shows a crossover effect. We obtain a scaling form for the area as well the susceptibility that describes the behaviour of the system about the transition. This transition is analogous to the finite pressure transition observed in the self-intersecting case, although here, unlike in the original transition, the N exponent is identical on both sides of the transition. The transition separates a weakly inflated phase, where although the area scales as N^2, there is no dependence on the maximum bond length R_0, from a strongly inflated phase, where the area scales as $(NR_0)^2$, where NR_0 can be thought of as the maximum perimeter. In this strongly inflated phase, the shape of the ring is a regular polygon, and the fluctuations about this shape are in the form of breathing modes, involving the contraction and expansion of the ring as a whole while maintaining the regular polygon nature.

The behaviour of the area above the transition, in fact, can be computed by a simple analytic calculation. In this regime, as noted, the shape of the polygon ring is simply a regular polygon. The free energy in this regime is given simply by the sum of the pressure energy and the spring energy of the regular polygon.

$$F = -pA + \text{SpringEnergy(Regular polygon)}, \tag{4.28}$$

where, p is the pressure and A is the area of the polygon. For a regular polygon of side a, the area is given by,

$$A = \frac{1}{4} N a^2 \cot(\frac{\pi}{N}), \tag{4.29}$$

while the maximum possible area is given by,

$$A_{max} = \frac{1}{4} N R_0^2 \cot(\frac{\pi}{N}), \tag{4.30}$$

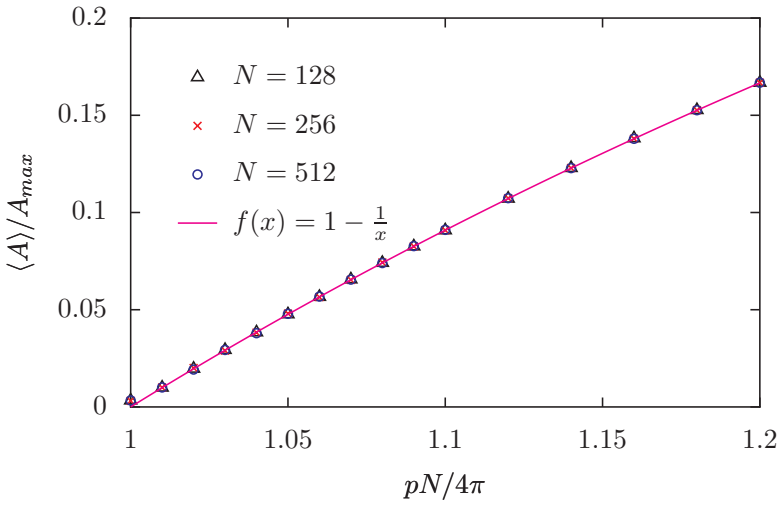

Figure 4.31: The large pressure behaviour of the average area. This verifies the prediction of Eq. 4.36. The data is shown for Model C for three system sizes $N = 128, 256, 512$ with $R_0 = 30.0$.

where R_0 is the maximum allowed bond length. If we consider that the spring energy is given by the logarithmic potential,

$$\begin{aligned} V(a) &= -R_0^2 \ln\left(1 - \frac{a^2}{R_0^2}\right) \\ &= -R_0^2 \ln\left(1 - \frac{A}{A_{max}}\right), \end{aligned} \tag{4.31}$$

then the free energy can be written as,

$$F = -pA - NR_0^2 \ln\left(1 - \frac{A}{A_{max}}\right). \tag{4.32}$$

The average area is obtained by solving the equation $\frac{dF}{dA} = 0$ for A. This gives,

$$p = \frac{4\tan(\pi/N)}{1 - \frac{\langle A \rangle}{A_{max}}}. \tag{4.33}$$

Defining the scaled pressure as,

$$\tilde{p} = \frac{1}{4} p \cot(\frac{\pi}{N}), \tag{4.34}$$

we obtain,

$$\tilde{p} = \frac{1}{1 - \frac{\langle A \rangle}{A_{max}}}. \tag{4.35}$$

Note that this definition for $\tilde{p}$ is in fact the correct one, reducing to the usual $\tilde{p} = \frac{pN}{4\pi}$ for large system sizes. The average area is then given by

$$\frac{\langle A \rangle}{A_{max}} = 1 - \frac{1}{\tilde{p}}. \tag{4.36}$$

This prediction turns out to be very accurate in predicting the behaviour of the area for large pressures, extending almost upto the critical pressure for large R_0. This is illustrated in Fig. 4.31.

The critical pressure can be determined by using a scaling approach similar to the one used to derive the contributions to the free energy in the self-intersecting ring case (Sec. 2.4.1). Assuming that the spring potential is described by a logarithmic potential

$$V(a) = -\frac{R_0^2}{\Delta^2} \ln\big(1 - \frac{a^2}{R_0^2}\big), \tag{4.37}$$

the partition function $\mathcal{Z}$ for a ring of N monomers can be written down as

$$\mathcal{Z}^{1/N} = \int_0^{R_0} da \int_0^{2\pi} d\theta \; a e^{-V(a)} e^{fa\cos\theta}. \tag{4.38}$$

On performing the integrals and expanding as a series in f, we obtain,

$$\mathcal{Z}^{1/N} = \frac{R_0^2\Delta^2}{2(R_0^2+\Delta^2)} + \frac{f^2}{4}\frac{R_0^4\Delta^4}{2R_0^4 + 6R_0^2\Delta^2 + 4\Delta^4} + \frac{f^4}{64}\frac{R_0^6\Gamma(1+R_0^2/\Delta^2)}{\Gamma(4+R_0^2/\Delta^2)} + ... \tag{4.39}$$

The mean end-to-end distance in the limit of small force is obtained from $R \sim \partial \ln Z/\partial f$ and this is then inverted to give an expression for f as a function of R/N. The free energy is then given by,

$$\begin{aligned} F(R) &= -\ln \mathcal{Z}[f(R)] + f.R, \\ &= \frac{R^2}{N\Delta^2}\big(1 + \frac{2\Delta^2}{R_0^2}\big) + \frac{R^4}{2N^3R_0^2\Delta^2}\frac{1+2\Delta^2/R_0^2}{1+3\Delta^2/R_0^2}. \end{aligned} \tag{4.40}$$

In addition, there are contributions from the self-avoidance F_{SA} and the pressur-

ization term $F_{pressure} = -pR^2 \sim -\frac{\tilde{p}R^2}{N\Delta^2}$. Thus the full free energy is given by

$$F = F_{SA} + \frac{R^2}{N\Delta^2}\big(1 + \frac{2\Delta^2}{R_0^2} - \tilde{p}\big) + \frac{R^4}{2N^3R_0^2\Delta^2}\frac{1 + 2\Delta^2/R_0^2}{1 + 3\Delta^2/R_0^2}. \tag{4.41}$$

This form of the free energy then predicts the transition pressure as a function of the maximum bond length R_0 as

$$\tilde{p}_c(R_0) = 1 + \frac{2\Delta^2}{R_0^2}. \tag{4.42}$$

If we then define the scaled pressure as $\tilde{p} = \frac{p\cot(\pi/N)}{4(1+\frac{2\Delta^2}{R_0^2})}$, the transition pressure can be seen to be exactly $\tilde{p}_c = 1.0$ for all values of R_0.

4.8 Conclusion

In conclusion, we have shown that models which are physically more appealing generalizations of the LSF model can be shown to have a genuine phase transition at non-zero $\tilde{p}$. We have demonstrated this through a careful study of the area scaling on both sides of the transition, as well as through a study of geometrical properties of the ring polymer.

For the LSF model, our data indicate that there is no such finite pressure transition. We ascribe this to the fact that the LSF model is defined such that only the intersection of the discs is relevant, since the cutoff-scale R_0 is of order the size of the disc a. However, in the limit that $R_0 \gg a$, the transition can be clearly seen - first as a sequence of two peaks in the area susceptibility as a function of pressure, with the lower peak sharpening and moving towards $p = 0$ if the definition $\hat{p} = pN^{3/2}$ is used. The second peak, located at $\hat{p} = pN = 1$, becomes sharper if pN scaling is used. At values of $R_0 \gg a$, only the peak at $\tilde{p} = 1$ is seen, and a generic transition transition is obtained.

The new results of this chapter also include the following: we have demonstrated that the phase transition in the simple Rudnick-Gaspari model survives the incorporation of self-avoidance. Interestingly, the transition is also shown to occur at precisely the same value of the scaled pressure as in the self-intersecting model. We have also shown that first-order transitions between weakly inflated

and strongly inflated phases of the ring polymer are generic and can be obtained in a sequence of models which generalize the LSF model to include a more realistic interactions between different monomers of the polymer. The fact that simple models for two-dimensional pressurized polymer rings can yield first-order transitions does not seem to have been noticed in the literature before.

5
Conclusion

In this thesis we have studied the properties of different models for pressurised polymer rings. We study polymer rings with and without self-avoidance, and also investigate the effects of semiflexibility on the system behaviour.

Firstly, we have looked in detail at the problem of self-intersecting rings with semiflexibility. While this problem had been studied earlier for flexible ring polymers and a phase transition was known to exist separating a collapsed phase from an inflated phase, a detailed study of the effects of nonzero bending rigidity on the phase diagram is important since semiflexible effects are important for any real biological polymer. We calculated the phase boundary in the presence of non-zero bending rigidity using scaling arguments. We studied both lattice and continuum ring polymers and established the fact that below the transition the lattice structure of the ring does not affect the average properties of the system. The lattice model has the advantage that the various possible configurations can be enumerated exactly and hence the partition function can be calculated with high accuracy. We also extended the previously known mean field calculations using Lagrange multipliers for the semiflexible case. We performed mean field calculations, and showed that using a suitable ansatz for the ground state hamiltonian, we can reproduce the properties of the system with a greater accuracy than the previous mean field theory. We also characterised the critical exponents around the finite pressure transition.

In the case of lattice polymers, we computed the area of the convex and column convex polygons using analytic methods. Interestingly, it turned out that the asymptotic area of both classes of polygons is the same in the limit of large pres-

sures. This suggests that overhangs are not important in the inflated phase, and hence we conjectured that the same area formula should be valid in the case of self-avoiding polygons also in the limit of large pressures. We verified this hypotheses using numerical techniques, Monte Carlo and lattice enumeration for both flexible and semiflexible polymers. The asymptotic area is found to be given by

$$\langle A \rangle = \frac{N^2}{16}\left[1 - \frac{32\pi^2}{3\tilde{p}^2} + \frac{64}{\tilde{p}^2}\mathrm{Li}_2\left(1-\alpha\right)\right] + \mathcal{O}(e^{-\tilde{p}/8}), \tag{5.1}$$

where Li_2 is the dilogarithm function

$$\mathrm{Li}_2(x) = \sum_{m=1}^{\infty} \frac{x^m}{m^2}, \tag{5.2}$$

and, $\alpha = e^{-2J}$, and J is the bending energy cost. This analysis was performed for polygons of fixed perimeter, and then we calculated the average area as a function of the pressure. However, the converse case is also interesting. It would be instructive to repeat the calculation for polygons with a fixed area but variable perimeter. If the convex and column convex polygons have the same asymptotic behaviour in this case also, then the self-avoiding polygon answer can be obtained using a similar reasoning.

Finally in the thesis, we looked at self-avoiding polymer rings. The canonical model in this case is the Leibler, Singh, Fisher Model which shows a continuous phase transition at zero pressure, separating a branched polymer phase from an inflated phase. We study a generalised model for self-avoiding rings, and consider the question of whether there exists a finite pressure phase transition in a scaled pressure variable similar to the self-intersecting case. The answer is that there does exist a phase transition, but it is a subtle effect in that the transition does not occur with system size but rather with the maximum bond length parameter R_0. Further, depending on the potential used for interactions between the constituent monomers, the transition can be either first order or continuous. We characterise the exponents at the transition and provide an explanation of the behaviour we see in terms of a shape transition. The system is found to be in the inflated regime throughout, but beyond the transition switches to a regular polygon configuration. Further fluctuations are akin to breathing modes, which do not change the overall

shape. This transition has not been reported for self-avoiding rings in the literature.

Bibliography

[1] K. Alim and E. Frey. Shapes of semiflexible polymer rings. *Phys. Rev. Lett.*, 99:198102, 2007.

[2] A. Baumgartner and J.S. Ho. Crumpling of fluid vesicles. *Phys. Rev. A*, 41:5747–5750, 1990.

[3] M. Bousquet-Melou. Convex polyominoes and algebraic languages. *J. Phys. A.*, 25:1935–1944, 1992.

[4] M. Bousquet-Melou. Convex polyominoes and heaps of segments. *J. Phys. A.*, 25:1925–1934, 1992.

[5] M. Bousquet-Melou. A method for the enumeration of various classes of column-convex polygons. *Discrete Math.*, 154:1–25, 1996.

[6] R. Brak and A. J. Guttmann. Exact solution of the staircase and row-convex polygon perimeter and area generating function. *J. Phys. A*, 23:4581–4588, 1990.

[7] Carlos J. Camacho and Michael E. Fisher. Tunable fractal shapes in self-avoiding polygons and planar vesicles. *Phys. Rev. Lett.*, 65:9–12, 1990.

[8] P.B. Canham. The minimum energy of bending as a possible explanation of the biconcave shape of the human red blood cell. *J. Theor. Biol.*, 26:61–81, 1970.

[9] John Cardy. Exact scaling functions for self-avoiding loops and branched polymers. *J. Phys. A*, 34:L665–L672, 2001.

[10] P.M. Chaikin and T.C. Lubensky. *Principles of Condensed Matter Physics*. Cambridge University Press, 1995.

[11] E. Evans. Bending resistance and chemically induced moments in membrane bilayers. *Biophys. J.*, 14:923–931, 1974.

[12] R.P. Feynman and A.R Hibbs. *Quantum Mechanics and Path Integrals*. McGraw-Hill Book Company, 1965.

[13] Michael E. Fisher. Shape of a self-avoiding walk or polymer chain. *J. Chem. Phys.*, 44:616–622, 1966.

[14] Michael E. Fisher. Fractal and nonfractal shapes in two-dimensional vesicles. *Physica D*, 38:112–118, 1989.

[15] Michael E. Fisher, Anthony J. Guttmann, and Stuart G. Whittington. Two-dimensional lattice vesciles and polygons. *J. Phys. A*, 24:3095–3106, 1991.

[16] W. C. Forsman and R. E. Hughes. Radii of gyration for random-flight chains. *J. Chem. Phys.*, 38:2118, 1963.

[17] George Gaspari, Joseph Rudnick, and Arezki Beldjenna. The shapes of open and closed random walks : a 1/d expansion. *J. Phys. A*, 20:3393–3414, 1987.

[18] George Gaspari, Joseph Rudnick, and Arezki Beldjenna. The shapes and sizes of two-dimensional pressurized, self-intersecting rings, as models for two-dimensional vesicles. *J. Phys. A*, 26:1–13, 1993.

[19] G. Gomper and D. M. Kroll. Inflated vesicles: A new phase of fluid membranes. *Europhys. Lett.*, 19:581–586, 1992.

[20] A. Y. Grosberg. Critical exponents for random knots. *Phys. Rev. Lett.*, 85:3858–3861, 2000.

[21] E. Haleva and H. Diamant. Smoothening transition of a two-dimensional pressurized polymer ring. *Eur. Phys. J. E*, 19:461–469, 2006.

[22] E. Haleva and H. Diamant. Swelling of particle-encapsulating random manifolds. *Phys. Rev. E*, 78:021132–1 – 021132–7, 2008.

[23] W. Helfrich. Elastic properties of lipid bilayers: theory and possible experiments. *Z. Naturforsch.*, 28:693–703, 1973.

[24] Iwan Jensen. Number of sap of given perimeter and any area.

[25] Iwan Jensen. A parallel algorithm for the enumeration of self-avoiding polygons on the sqaure lattice. *J. Phys. A*, 36:5731–5745, 2003.

[26] Kleanthes Koniaris. Modeling large gaussian ring polymers. *J. Chem. Phys.*, 101:731–733, 1994.

[27] Stanislas Leibler, Rajiv R. P. Singh, and Michael E. Fisher. Thermodynamic behaviour of two-dimensional vesicles. *Phys. Rev. Lett.*, 59:1989–1992, 1987.

[28] Edward Levinson. Asphericity of two-dimensional closed pressurized random walks. *Phys. Rev. A*, 45:3629–3636, 1992.

[29] K. Y. Lin. Exact solution of the convex polygon perimeter and area generating function. *J. Phys. A.*, 24:2411–2417, 1991.

[30] N. Madras, A. Orlitsky, and L. A. Shepp. Monte carlo generation of self-avoiding walks with fixed endpoints and fixed length. *J. Stat. Phys.*, 58:159–183, 1990.

[31] Anthony C. Maggs, Stanislas Leibler, Michael E. Fisher, and Carlos J. Camacho. Size of an inflated vesicle in two dimensions. *Phys. Rev. A*, 42:691–695, 1990.

[32] M. K. Mitra, G. I. Menon, and R. Rajesh. Phase transitions in pressurised semiflexible polymer rings. *Phys. Rev. E*, 77:041802, 2008.

[33] N.T. Moore and A. Y. Grosberg. Limits of analogy between self-avoidance and topology-driven swelling of polymer loops. *Phys. Rev. E*, 72, 2005.

[34] E. Orlandini and M. C. Tessi. Monte carlo study of 3d vesicles. *Physica A*, 185:160–165, 1992.

[35] T. Prellberg and A. L. Owczarek. On the asymptotics of the finite-perimeter partition function of two-dimensional lattice vesicles. *Commun. Math. Phys.*, 201:493–505, 1999.

[36] V. Privman and N.M. Svrakic. *Directed Models of Polymers, Interfaces, and Clusters: Scaling and Finite-Size Properties*. Springer-Verlag, 1989.

[37] R. Rajesh and Deepak Dhar. Convex lattice polygons of fixed area with perimeter-dependant weights. *Phys. Rev. E*, 71:016130–1–016130–8, 2005.

[38] C. Richard. Scaling behaviour of two-dimensional polygon models. *J. Stat. Phys.*, 108:459–493, 2002.

[39] C. Richard, A. J. Guttmann, and I. Jensen. Scaling function and universal amplitude combinations for self-avoiding polygons. *J. Phys. A*, 34:L495–L501, 2001.

[40] C. Richard, I. Jensen, and A. J. Guttmann. Scaling function for self-avoiding polygons revisited. *J. Stat. Mech*, page P00807, 2004.

[41] C. Rottman and M. Wortis. Statistical mechanics of equilibrium crystal shapes: interfacial phase diagrams and phase transition. *Phys. Rep.*, 103:59–79, 1984.

[42] Joseph Rudnick and George Gaspari. The shapes and sizes of closed pressurized random walks. *Science*, 252:422–, 1991.

[43] S. V. M. Satyanarayana and A. Baumgaertner. Shape and motility of a model cell: A computational study. *J. Chem. Phys.*, 121:4255–4265, 2004.

[44] E. van Faassen. Effects of surface fluctuations in a two-dimensional emulsion. *Physica A*, 255:251–268, 1998.

[45] E. J. J. van Rensburg. *The Statistical Mechanics of Interacting Walks, Polygons, Animals and Vesicles*. Oxford University Press, 2000.

[46] E J Janse van Rensburg, S.G. Whittington, and N. Madras. The pivot algorithm and polygons: results on the fcc lattice. *J. Phys. A*, 23:1589–1612, 1990.